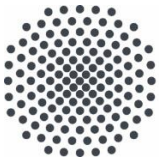

Universität Stuttgart

Artificial solid electrolyte interphase protecting metal anodes in metal-sulfur batteries

Künstliche Anoden-Elektrolyt-Grenzschichten zum Schutz der Metallanode in Metall-Schwefel Batterien

Masterarbeit

Studiengang Chemie

Tobias Rommel

2801168

20.10.2020

Prüfer

Prof. Dr. K. Andreas Friedrich

Institut für Technische Thermodynamik

Deutsches Zentrum für Luft- und Raumfahrt

Erklärung

Hiermit versichere ich, Tobias Rommel, dass ich meine Arbeit selbständig verfasst habe, dass ich keine anderen als die angegebenen Quellen benutzt und alle wörtlich oder sinngemäß aus anderen Werken übernommenen Aussagen als solche gekennzeichnet habe, dass die eingereichte Arbeit weder vollständig noch in wesentlichen Teilen Gegenstand eines anderen Prüfungsverfahrens gewesen ist, dass ich die Arbeit weder vollständig noch in Teilen bereits veröffentlicht habe, es sei denn, der Prüfer/die Prüferin hat die Veröffentlichung zuvor genehmigt, und dass das elektronische Exemplar mit den anderen Exemplaren übereinstimmt.

Stuttgart, den 20.10.2020

Tobias Rommel

Danksagung

An dieser Stelle danke ich Prof. Dr. Andreas Köhn für die Genehmigung, die vorliegende Masterarbeit am Deutschen Zentrum für Luft- und Raumfahrt anfertigen zu dürfen. In diesem Zusammenhang danke ich Prof. Dr. K. Andreas Friedrich für die Vergabe des hochaktuellen Forschungsthemas „Artificial SEI protecting metal anodes in metal-sulfur batteries“ und die Übernahme des Erstgutachtens der Masterarbeit.

Für die freundliche Aufnahme in die Arbeitsgruppe für Batterietechnik und die Möglichkeit, die Masterarbeit in dieser Gruppe bearbeiten zu dürfen, danke ich Dr. Norbert Wagner.

Ein besonderer Dank gilt Dr. Maryam Nojabaee und Joachim Häcker, die mich während der Masterarbeit betreut haben. Vielen Dank für den stets kompetenten fachlichen Rat und die immer geduldige und freundliche Unterstützung bei Fragen aller Art. Zudem möchte ich euch für die organisatorischen Bemühungen im Vorfeld dieser Arbeit danken.

Des Weiteren danke ich allen Mitarbeitern der Arbeitsgruppe für Batterietechnik für die gute Zusammenarbeit und die Hilfe und Unterstützung bei labortechnischen Fragen.

Ebenso möchte ich mich bei Martina Gerle bedanken, die zeitgleich mit mir ihre Masterarbeit im Bereich der Me-S Batterie angefertigt hat. Danke für den harmonischen Büro- und Laboralltag. Danke auch an Pia Lange für viele hilfreiche Tipps im Labor.

Zuletzt danke ich meinen Eltern und meiner Freundin Rahel Schulze für die Geduld und Unterstützung während der Masterarbeit und des gesamten Studiums. Auf euch ist immer Verlass – Danke.

Kurzfassung

Metall-Schwefel Batterien stellen ein vielversprechendes System für Hochenergiezellen dar und sind daher im Fokus vieler Forschungsgruppen. Ein Hauptproblem dieses Systems ist der sogenannte Polysulfidshuttle, sowie die inhomogene Metallabscheidung, die zu Dendriten führen kann. Um beidem entgegenzuwirken sollen in dieser Thesis Magnesium (Mg)- und Lithium (Li)-Metalloberflächen mit einer künstlichen Anoden-Elektrolyt-Grenzschicht (SEI) beschichtet werden. Die Beschichtung hält Polysulfide von der Reaktion an der Anode ab und verhindert eine übermäßige Elektrolytzersetzung. Zudem kann eine homogenere Metallabscheidung ermöglicht werden.

Beschichtungen basierend auf Ionomeren (z.B. Aquivion) und thermisch-zyklisiertem Poly(acrylnitril) (PAN) wurden mittels Spin- oder Dip-Coating auf die Metalloberfläche aufgetragen.

Magnesium-Schwefel (Mg-S) Zellen mit künstlicher SEI wurden für über 150 Zyklen stabil bei C/10 zyklisiert. Die Implementierung einer Aquivion-basierten SEI resultierte neben einer besseren Coulomb-Effizienz in einem konstanten Kapazitätsgewinn von etwa 200 % im Vergleich zu einer Zelle mit unbeschichteter Anode. Zudem erhöhte sich die Kapazität einer Mg-S Zelle durch die Implementierung einer PAN-basierten SEI. Weitere Ionomer-basierte Beschichtungen (z.B. Nafion, sulfoniertes Poly(etheretherketon) (SPEEK)) führten in den ersten Zyklen zu höheren Kapazitäten. Das partielle Aufbrechen der künstlichen SEI führte jedoch mit steigender Zyklenzahl zu einem Angleichen an die Werte der Mg-S Referenzzelle mit unbeschichteter Anode.

Um ein besseres Verständnis für die Grenzflächeneffekte zwischen Anode und Elektrolyt zu bekommen, wurde Elektrochemische Impedanzspektroskopie (EIS) in Mg-Mg und Mg-S Zellen eingesetzt. Während der Polarisation einer Mg-Mg Zelle mit unbeschichteter Anode wurden zwei Prozesse beobachtet. Ein Prozess in der mittelfrequenten (MF) Region durch die *in-situ* SEI sowie ein Prozess in der hochfrequenten (HF) Region auf Grund des Ladungstransports. Homogen beschichtete Anoden zeigten zusätzlich einen weiteren Prozess in der niederfrequenten (NF) Region, welcher der künstlichen SEI zugeordnet wurde. Während des OCV bildete sich eine Adsorptionsschicht auf der unbeschichteten Anode. Der Prozess der Adsorptionsschicht und der Prozess der künstlichen SEI weisen ähnliche Zeitkonstanten auf.

Der Beitrag von Schwefelspezies zur Grenzflächenschichtbildung an der Mg-Anode wurde in Mg-S Vollzellen während des OCV und den folgenden ersten zehn Zyklen untersucht. Während der anfänglichen OCV Phase formierten sich zwei Prozesse, die nur mit unbeschichteter Anode eindeutig in einen HF- und MF-Prozess unterteilt werden konnten. Mit beschichteten Anoden wird die Trennung der Prozesse erst im nachfolgenden Entlade-/Ladezyklus deutlich.

Zusätzlich zu Mg wurde die Anwendbarkeit des künstlichen SEI-Schutzes auf Li-Metallanoden in Verbindung mit unterschiedlichen Kathoden untersucht. Insgesamt erreichten Zellen mit künstlicher SEI eine bessere Zyklenstabilität als Li-S Referenzzellen mit unbeschichteter Anode. Die Kombination einer Aerogel-Kathode mit einer künstlichen SEI basierend auf SPEEK oder sulfoniertem Poly(phenylensulfon) zeigte sich als besonders vielversprechend. Li-S Zellen konnten für über 400 Zyklen bei C/3 unter einem hohen Kapazitätserhalt zyklisiert werden.

Abstract

Metal-sulfur batteries represent a promising system for high-energy cells and are therefore the focus of many research groups. However, some problems with the system are known, namely the so-called polysulfide shuttle and the inhomogeneous metal deposition that can lead to dendrites. In order to counteract both, magnesium (Mg) and lithium (Li) metal surfaces are to be coated with an artificial solid electrolyte interphase (SEI) in this thesis. Such a coating prevents the anode from reaction with polysulfides and reduces an excessive electrolyte degradation. In addition, a more homogeneous metal deposition is possible.

Ionomer based coatings (*e.g.* Aquivion) and thermally cyclized poly(acrylonitrile) (PAN) were applied to the metal surface by means of spin or dip coating.

Artificial SEI coated anodes resulted in stable cycling performances for over 150 cycles at C/10 in magnesium-sulfur (Mg-S) cells. A better coulombic efficiency as well as a constant capacity gain of around 200% was achieved using an Aquivion-based SEI instead of an uncoated anode. In addition, the capacity of a Mg-S cell was increased by the PAN-based SEI. Other ionomer-based coatings (*e.g.* Nafion, sulfonated poly(etheretherketone) (SPEEK)) led to higher capacities in the initial cycles. The partial collapse of the artificial SEI, however, led to an adjustment to the values of the Mg-S reference cell with uncoated anode with increasing number of cycles.

Electrochemical impedance spectroscopy (EIS) was used in Mg-Mg and Mg-S cells to better understand the interface effects between anode and electrolyte. During polarization, two overall processes were present with the uncoated Mg reference anode. A fast charge transfer process (high-frequency (HF) region) and a slower process (middle-frequency (MF) region) through the formation of an *in-situ* SEI. Completely coated anodes showed the formation of another process in the low-frequency (LF) region, which was assigned to the artificial SEI. In addition, an adsorption layer formed on the uncoated anode during open circuit voltage (OCV). Similar time constants for the adsorption and the diffusion through the artificial SEI led to an overlay of the impedance response in the LF region.

The contribution of sulfur species to interfacial layer formation at the Mg anode was investigated in Mg-S full cells during OCV and the subsequent first ten cycles. During the initial

OCV phase, two processes were present and could be separated into an HF and MF process in the case of an uncoated anode. With coated anodes, the separation of these processes into an HF and MF process is possible in the subsequent discharge/charge cycle.

In order to investigate the influence of the artificial SEI on the cycling performance of Li-S cells, coated anodes along with various cathodes were tested. In conclusion, cells with artificial SEI achieved better long-term stability than cells with uncoated anode. The combination of an aerogel cathode with an artificial SEI based on SPEEK or sulfonated poly(phenylene sulfone) was proved to be particularly promising. Thus, Li-S cells could be cycled for over 400 cycles at C/3 with a high capacity retention.

Table of content

List of figures

List of tables

List of abbreviations and symbols

Abbreviations

Ads	Adsorption
BaSyTec	Battery system technology
CE	Counter electrode
CPE	Constant phase element
CT	Charge transfer
DLR	German Aerospace Center
ECM	Equivalent circuit model
EDX	Energy-dispersive X-ray spectrometer
EIS	Electrochemical impedance spectroscopy
FTIR	Fourier-transform infrared spectroscopy
HC	Half cell
HF	High-frequency
KIT	Karlsruhe Institute for Technologies
LF	Low-frequency
LIB	Lithium-ion battery
Me	Metal
Me-Me	Metal-metal
Me-S	Metal-sulfur
MF	Middle-frequency
MPI	Max-Planck-Institute
nom	Nominal
OCV	Open circuit voltage
RE	Reference electrode
SEI	Solid electrolyte interface
SEM	Scanning electron microscope
SHE	Standard hydrogen electrode
SOC	State of charge
TGA	Thermogravimetric analysis

WE		Working electrode
WE-Sense		Working sense electrode
XPS		X-ray photoelectron spectroscopy

Latin letters

C	F	Capacity
C_{nom}	$\mathrm{Ah \cdot kg^{-1}}$	Nominal capacity
C_{sp}	$\mathrm{Ah \cdot kg^{-1}}$	Specific capacity
$\mathrm{e^-}$		Electron
E	J	Energy
E_{m}	eV	Migration energy
E^0	V	Standard potential
F	$\mathrm{As \cdot mol^{-1}}$	Faraday constant
ΔG	J	Gibbs free energy
I	A	Electric current
L	H	Inductance
m	g	Mass
M	$\mathrm{g \cdot mol^{-1}}$	Molar mass
n	mol	Amount of substance
q	C	Electric charge
R	Ω	Resistance
U_{OCV}	V	Open circuit voltage
W_{sp}	$\mathrm{kWh \cdot kg^{-1}}$	Specific energy density
W		Warburg element
σ	$\mathrm{S \cdot m^{-1}}$	Conductivity
z		Number of electrons
Z	Ω	Impedance

Greek letters

ε_r		Relative permittivity
η		Efficiency
ϕ	eV	Work of emission

Chemical symbols

Al	Aluminum
Al_2O_3	Aluminum oxide

Cl^-	Chloride
CMC	Carboxymethyl cellulose
cPAN	Thermal-cyclized poly(acrylonitrile)
DEC	Diethyl carbonate
DGM	Diethylene glycol dimethyl ether, diglyme
DMAc	Dimethylacetamide
DMC	Dimethyl carbonate
DME	Ethylene glycol dimethyl ether, monoglyme
DMF	Dimethylformamide
DOL	1,3-dioxolane
EC	Ethylene carbonate
H	Hydrogen
KB	Ketjenblack
Li	Lithium
Li^+	Lithium ion
LiBOB	Lithium bis(oxalato)borate
LiFBOB	Lithium difluoro(oxalato)borate
$LiNO_3$	Lithium nitrate
$LiPF_6$	Lithium hexafluorophosphate
Li_3PO_4	Lithium phosphate
Li-S	Lithium-sulfur
LiTFSI	Lithium bis(trifluoromethylsulfonyl)imide
Mg	Magnesium
Mg^{2+}	Magnesium ion
$Mg[BH_4]_2$	Magnesium borohydride
$Mg[B(hfip)_4]_2$	Magnesium tetrakis(hexafluoroisopropyloxy)borate
$MgCO_3$	Magnesium carbonate
MgO	Magnesium oxide
MgS	Magnesium sulfide
Mg-S	Magnesium-sulfur
$Mg(TFSI)_2$	Magnesium bis(trifluoromethanesulfonyl)imide
MgX_2	Mg halides (X = fluorine, bromine, iodine)
Na	Sodium
PAN	Poly(acrylonitrile)
PC	Propylene carbonate
PDMS	Poly(dimethylsiloxane)
PEDOT	Poly(3,4-ethylenedioxythiophene-co-ethylene oxide)
PEO	Poly(ethyleneoxide)

PTFE	Poly(tetrafluoroethylene)
PVDF	Poly(vinylidene fluoride)
$R^F - OH$	Fluorinated alcohol
S/S_8	Sulfur
SO_3^-	Sulfonate
S_x^{2-}	Polysulfide ion (x = chain length)
SBR	Styrene-butadiene rubber
SPEEK	Sulfonated poly(etheretherketone)
s-PSO2	Hydrocarbon sulfonated poly(phenylene sulfone)
$TFSI^-$	Bis(trifluoromethylsulfonyl)imide
THF	Tetrahydrofuran
TGDME	Tetraethylene glycol dimethyl ether, tetraglyme

1 Introduction

Energy storage is a key component in the exit from nuclear and fossil-fuel energy. In battery technology the lithium-ion battery (LIB) is the currently dominant technology for stationary applications and electromobility. As a future alternative sulfur-based batteries are in focus of research. Due to the high theoretical capacity of $1675\,\mathrm{mAh}\cdot\mathrm{g}^{-1}$ and the conformity to ecological and economic requirements, sulfur is a promising electrode material. The combination with metals such as lithium and magnesium leads in theory to high energy densities.[1] In the lithium-sulfur (Li-S) system theoretical specific energy densities of 2600 $\mathrm{Wh}\cdot\mathrm{kg}^{-1}$ and 2800 $\mathrm{Wh}\cdot\mathrm{l}^{-1}$ can be achieved.[2] In combination with magnesium specific energy densities of 1600 $\mathrm{Wh}\cdot\mathrm{kg}^{-1}$ and 3200 $\mathrm{Wh}\cdot\mathrm{l}^{-1}$ are theoretically possible.[3] However, the commercialization of these metal-sulfur (Me-S) batteries still poses some challenges for research that have to be addressed.

A general problem of the sulfur-based batteries is the cycle stability due to the polysulfide shuttle. Furthermore, sulfur is an insulator by nature, which is why conductive additives that influence the specific energy density must be added to the cathode material. On side of the metal anode the *in-situ* formation of a solid electrolyte interphase (SEI) can be a problem due to a parasitic reduction reaction.[4] During cell cycling a passivation layer forms between the anode and the electrolyte, which among other things results in an overconsumption of the electrolyte. In addition, the growth of dendrites is promoted and thus the safety of the battery is negatively affected by the chance of short circuits. The thickness and inhomogeneity of the passivation layers formed additionally have an adverse effect on important properties such as ionic conductivity. In case of a magnesium anode such passivation layers can lead to irreversibility of the stripping and plating of Mg/Mg^{2+}.[5] To counteract this phenomenon, the metal electrode can be coated with an artificial SEI layer that exhibits desired properties. The artificial layer must be thin, homogeneous and mechanically elastic in order to be ionically conductive and electronically insulating.[6] Such a protective coating is able to minimize the polysulfide shuttle and the formation of dendrites, which consequently prevents short circuits and improves the cycling stability.

Therefore, the aim of this work is to coat and protect lithium and magnesium metal anodes with artificial *ex-situ* SEI. Various sulfonate ($-SO_3^-$) based ionomers such as Aquivion, Nafion or

sulfonated poly(etheretherketone) (SPEEK) are to be used for this purpose, which have a high ionic conductivity and high cation transfer number.[7,8] Moreover, a Mg^{2+}-conducting polymeric film made from thermal-cyclized poly(acrylonitrile) (PAN) and conductive magnesium salt is to be investigated as coating component specifically for the magnesium anode.[9] The organic-based coatings are applied to the metal surface by means of spin coating or dip coating in order to obtain layers that are as uniform as possible. The composition and morphology of the samples are to be examined using a scanning electron microscope (SEM), energy-dispersive X-ray spectrometer (EDX) and Fourier-transform infrared spectroscopy (FTIR). Electrochemical properties are to be investigated in the form of galvanostatic cycling tests and electrochemical impedance spectroscopy (EIS) in symmetrical metal-metal (Me-Me) cells as well as Me-S full cells.

2 State of the art

This chapter explains the basic terms and parameters of battery technology that are relevant for this master thesis. Furthermore, the mechanism and setup of metal-sulfur (Me-S) batteries in particular lithium-sulfur (Li-S) and magnesium-sulfur (Mg-S) batteries are discussed. The current state of the art includes advances and concepts of electrode materials with a focus on the metal anode. The phenomenon of the solid electrolyte interface (SEI) and the related design of artificial SEI are discussed in detail.

2.1 Battery technology

Batteries enable the storage of chemical energy, which can be converted into electrical energy and released again when required. The basic principle of this process is an electrochemical reaction between two spatially separated reactants. In the case of primary batteries this reaction is irreversible. In contrast, the reaction takes place reversibly in a secondary battery, which is why this type of battery is rechargeable.[10] A battery is the interconnection of several cells in which a single cell is the smallest rechargeable unit. The voltage and capacity of the battery can be defined by combining the cells in parallel or in series. In cell-level research the terms cell and battery are often used synonymously. In order to be able to compare batteries with regards to their prospective performance, standardized characteristics and terminologies are of great importance. Some of the most important in battery technology are explained in the following.[11–13]

Open circuit voltage

The open circuit voltage (OCV) is the potential difference between the electrodes of a single cell at non-operating state. In the equilibrium state the OCV can be calculated with the help of the electropotential series or by using the Gibbs free energy ΔG and the Faraday constant F.

$$U_{\mathrm{OCV}} = E^0_{\mathrm{anode}} - E^0_{\mathrm{cathode}} = -\frac{\Delta G}{zF} \tag{2.1}$$

E^0 describes the standard potential. The number of electrons transferred in the electrode reaction is described through *z*. Equation 2.1 applies to the ideal state. The OCV in practical cell operations depends on the temperature, the concentration of the reactants, the state of charge (SOC) and potentially formed electrode surface layers.

Specific capacity

The amount of electrical charge that a battery can deliver is called capacity. The theoretical specific capacity C_{sp} relates solely to the molar masses *M* of the active materials of the cell and is given in $\mathrm{Ah} \cdot \mathrm{kg}^{-1}$.

$$C_{\mathrm{sp}} = \frac{zF}{\sum M} \tag{2.2}$$

The practically achievable value is lower than theoretically estimated as for example additives, separators, current collectors or the cell housing increase the weight but do not provide any capacity.

Specific energy density

The specific energy density W_{sp} indicates how much energy *E* can be stored per weight (gravimetric energy density in $\mathrm{kWh} \cdot \mathrm{kg}^{-1}$) or per volume (volumetric energy density in $\mathrm{kWh} \cdot \mathrm{l}^{-1}$). The specific energy density is related to the specific capacity via equation 2.3 and therefore only relates to the active material of the cell. As mentioned before, the practical value will be significantly lower when taking named limitations into account.

$$W_{\mathrm{sp}} = C_{\mathrm{sp}} \cdot U_{\mathrm{OCV}} \tag{2.3}$$

Coulombic efficiency

The efficiency η of a battery is expressed as the ratio between the amount of energy that can be extracted and the amount of energy that is supplied.

$$\eta_{\mathrm{Coulomb}} = \frac{q_{\mathrm{discharge}}}{q_{\mathrm{charge}}} \tag{2.4}$$

It is defined as the ratio of charge released by an electrode to the charge stored in the electrode during a cycle. This allows to quantify the charge loss of the battery during cycling since practical systems are never fully reversible.

C-rate

The charge or discharge current I of a battery is referred to as the C-rate C. It is defined as the quotient of I and the nominal capacity C_{nom} (Equation 2.5).

$$C = \frac{I}{C_{\mathrm{nom}}} \tag{2.5}$$

The C-rate is always related to the maximum capacity of the battery.

Cycle life

Cycle life refers to the capacity retention of a battery when it is discharged/charged (cycle ageing) and is often described as a number of cycles. The number of cycles indicates how often a battery can be cycled until a lower capacity limit is reached. The lower capacity limit is defined as 80% of the initial capacity. In laboratory operation the lower limit depends on the battery type and various factors such as the C-rate or temperature. To compare the cycle life of batteries comparable test conditions must be ensured and the loss of capacity due to the calendar aging of the battery must be considered.

2.2 Metal-sulfur batteries

Me-S batteries are rechargeable batteries and therefore belong to the group of secondary batteries. Among lithium metal as the most popular metal anode, several other mono- (Na, K) and multivalent (Ca, Mg, Al) metals have gained attention as future Me-S battery anodes due to their abundancy and enhanced safety.[1] Li-S batteries have been in the focus of research for decades and are considered as potential post LIBs. In recent years, research has also focused on Mg-S batteries as an alternative.

The functional principle of Me-S batteries is based on a redox reaction between metal on the anode side and sulfur on the cathode side. The metal is oxidized during the discharge, whereat metal ions are released from the anode (stripping), move into the electrolyte and migrate through the separator to the cathode. The electrons formed during the oxidation (Equation 2.6 and 2.8) pass from the anode to the cathode via an external circuit. A gradual reduction of elemental sulfur to metal sulfide takes place simultaneously on the sulfur cathode. The step-by-step reaction generates polysulfides with different chain lengths S_x^{2-} ($2 \leq x \leq 8$) as partially soluble intermediates. This process ideally takes place reversibly when charging. Metal ions are reduced and deposited again at the anode (plating) and metal polysulfides are reoxidized to elemental sulfur. Equations 2.6-2.9 show the respective sum reactions.

Li-S battery

$$2\,Li \rightleftharpoons 2\,Li^+ + 2\,e^- \quad (2.6)$$

$$S_8 + 16\,Li^+ + 16\,e^- \rightleftharpoons 8\,Li_2S \quad (2.7)$$

Mg-S battery

$$Mg \rightleftharpoons Mg^{2+} + 2\,e^- \quad (2.8)$$

$$S_8 + 8\,Mg^{2+} + 16\,e^- \rightleftharpoons 8\,MgS \quad (2.9)$$

The electron transfer between the metal anode and the sulfur cathode results in a cell voltage of 2.28 V in the Li-S system and a cell voltage of 1.77 V in the Mg-S system.[14] The schematic structure of a Me-S battery with the formed polysulfide species during discharging/charging is shown in Figure 2.1.

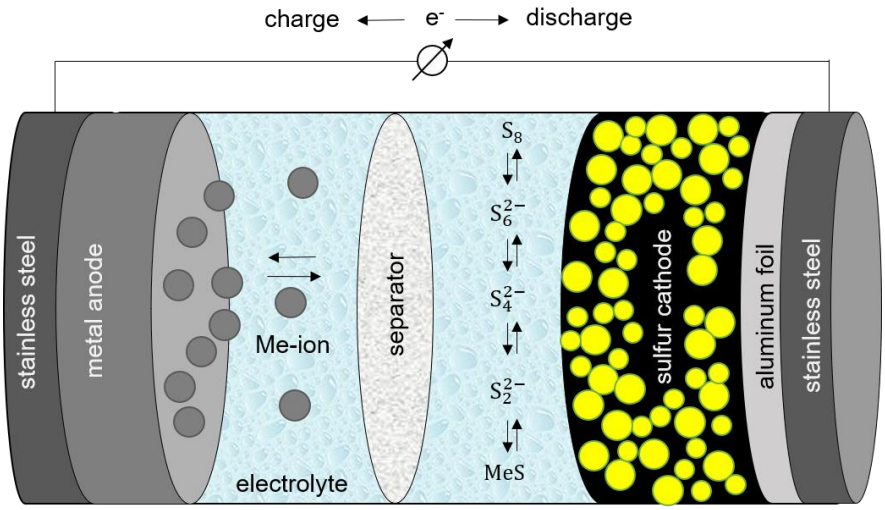

Figure 2.1: Simplified schematic of a metal-sulfur battery.

As shown in Figure 2.1 the electrochemically active materials of the cell consist of the metal anode and the sulfur cathode with the electrolyte and separator as other the main components. External current flow is realized via two current collectors. The materials and concepts of the individual components are described in more detail in the following chapters.

2.2.1 Metal anode

Li is a monovalent metal and belongs to the group of alkali metals. Due to a variety of advantages Li is one of the most promising electrode materials: the theoretical capacity of Li ($3861\ \mathrm{mAh \cdot g^{-1}}$ and $2062\ \mathrm{mAh \cdot ml^{-1}}$) is about ten times higher than the theoretical capacity of conventional graphite ($372\ \mathrm{mAh \cdot g^{-1}}$).[15] In addition, the low standard potential of $E^0 = -3.04$ V versus standard hydrogen electrode (SHE) and the small ion radius of Li^+ (0.9 Å) are further advantages of Li as active material.[16] The high theoretical capacity of the electrode material results in very high gravimetric and volumetric energy densities of $2600\ \mathrm{Wh \cdot kg^{-1}}$ and $2800\ \mathrm{Wh \cdot l^{-1}}$ of the Li-S battery.[2]

Li metal can, however, easily react with the electrolyte components. As a result, the surface of the Li anode is covered with a multiphase surface layer (SEI). The SEI exhibits an insulating effect, which results in severe overpotentials (Chapter 2.2.6). Another challenge is the formation of mossy lithium dendrites on the metal surface, which can lead to a short circuit.[17] Dendrites therefore represent a safety risk for the battery. Besides that, there is the loss of active

material ("dead lithium") of the anode due to the dissolution of lithium dendrites, which leads to a loss of capacity.[6] To avoid this effect some approaches for stabilizing the Li anode are proposed: the coating of the separator, the use of electrolyte additives or the formation of an artificial protective layer (artificial SEI).[15] Another approach is the sandwich protection technology in which a current collector is inserted between the Li anode and the cathode.[18] The aim is to homogenize the Li-ion transport. So-called compound anodes in which Li is used together with one or more other materials can also provide effective protection.[19] Figure 2.2 shows a graphical comparison of the electrochemistry of Li and Mg in terms of capacities and reductive potentials as well as a contrast of the related Me-S systems.

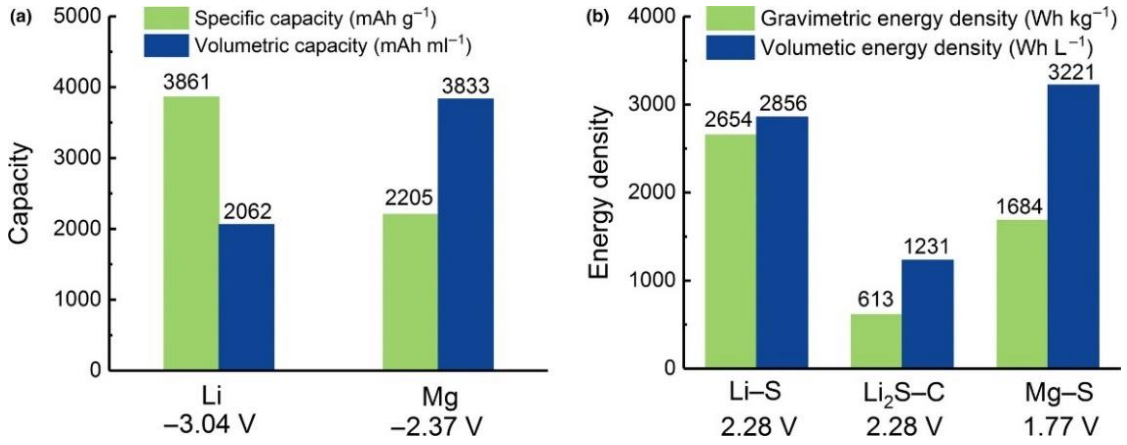

Figure 2.2: Comparison of the capacities and reductive potentials of Li and Mg (left). Comparison of energy densities and thermodynamic equilibrium voltage of Li and Mg batteries (right).[14]

As Li resources are limited, intensive research is being carried out on ecologically and economically attractive alternatives. The bivalent alkaline earth metal Mg is earth abundant and has high theoretical capacities of 2205 mAh $\cdot$ g^{-1} and 3833 mAh $\cdot$ ml^{-1} as well as a standard potential of -2.37 V versus SHE.[14] Due to the bivalence of Mg^{2+} (ion radius = 0.86 Å similar to Li) and the higher physically density of Mg (0.53 g $\cdot$ cm^{-3} vs. 1.74 g $\cdot$ cm^{-3}) Mg-S batteries have a higher theoretical volumetric capacity of 3200 Wh $\cdot$ l^{-1} than Li-S batteries.[20] The gravimetric energy density of 1600 Wh $\cdot$ kg^{-1}, however, is lower than that of Li-S batteries. In addition, Mg-ions have a slower solid state diffusion than Li-ions.

Compared to Li, Mg has less tendency to form dendrites, which is a safety advantage of the material of Mg-S batteries.[21] Bonnick *et al.* point out that the formation of dendrites strongly depends on the electrolyte used and the density of the electrical current. Dendrite-free deposition of Mg therefore is only possible up to certain current limits.[22] To date, however, these current limits have not yet been finally researched.[23] Previous research on Mg-S batteries has focused heavily on development of suitable electrolyte systems, modification of the sulfur cathode and mechanistic studies (Figure 2.3). Only about 6% of the publications deal with a magnesium anode leaving aside the enormous potential of the Mg anode.[24] A comparison of the percentage of publications in the main research fields in Mg-S batteries is shown in Figure 2.3.

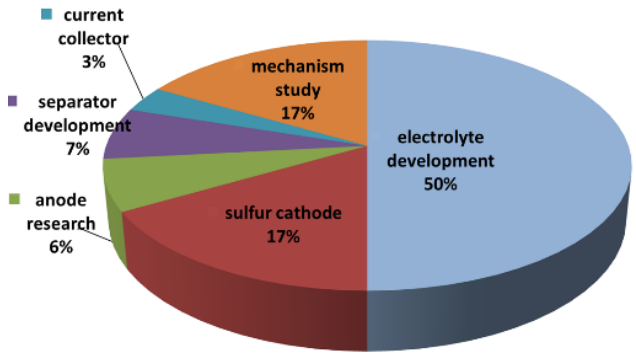

Figure 2.3: Comparison of research topics in publications on Mg-S batteries.[24]

Currently Mg anodes in the form of magnesium disks, plates, strips or foils are generally used. Sievert *et al*. showed one possibility for further development by using a pressed Mg powder anode.[25] Due to interconnected channels and scaffolds a faster diffusion of ions and electrons in the cell is possible. Anodes that have been pressed at low pressure (350 MPa) absorb more electrolyte than a conventional magnesium foil and show an improved electrochemical behavior. So far, the formation of a passivating layer on the Mg anode, which inhibits Mg^{2+} transport has proven to be problematic. Modification of the anode is recommended to ensure long-term reversible stripping and plating of Mg/Mg^{2+}.[26]

2.2.2 Sulfur cathode

Sulfur is harmless to health, sufficiently available and therefore inexpensive. Furthermore, in chemical industry sulfur is a waste product from the desulfurization of petroleum. In addition to the economic and ecological advantages sulfur exhibits a very high theoretical capacity of 1675 $Ah \cdot kg^{-1}$ as well as a large electrochemical potential difference to the metals of the anode.[27]

To achieve electrochemical addressability, however, conductive additives have to be added to the active material due to the insulating properties of elemental sulfur.[28] Further, a polymeric binder is required to achieve a sufficient mechanical strength and ensure direct contact of the particles. This has a negative impact on the specific energy density. To ensure the highest possible energy densities cathode systems are required, which can deliver reversibly high capacities and show a slow capacity fading during cycling. In addition, compatibility with the electrolyte must be guaranteed. There are numerous proposed solutions to combine these capabilities in a suitable cathode system. The most common approach is the homogeneous implementation of elemental sulfur in a conductive network, usually a porous carbon matrix via melt infiltration. The sulfur particles are encased in the conductive material and are thereby made electrochemically addressable. Another approach are systems in which (poly)sulfidic species are covalently bound to a carrier matrix.[29] Due to the strength of covalent chemical bonds this type of cathode proves to be particularly stable and can minimize the loss of active material through the polysulfide shuttle. The polysulfide shuttle mechanism is described in detail in Chapter 2.2.5.

2.2.3 Electrolyte

The ions are transported between the electrodes by means of an electrolyte. Ideally, this offers good ion conductivity as well as thermal, electrochemical and chemical stability, low toxicity and flammability.[30,31] In this connection the reversible stripping and plating of the metal must be guaranteed. Still, it turns out to be difficult to combine all these properties. In Me-S batteries usually liquid electrolyte systems consisting of a conductive salt which is dissolved in a solvent or a solvent mixture are used. The composition influences important physical properties such as viscosity and conductivity. Also, the undesirable loss of active material from the cathode via the polysulfide shuttle can be minimized by suitable compositions.[32] The electrolyte thus has a major impact on the performance and cycle stability of the used cell chemistry and is therefore

one of the research priorities in the improvement of Me-S batteries. Since the metals lithium and magnesium partly differ in their chemical properties different electrolytes are required for Li-S and Mg-S batteries.

Due to its good ion conductivity as well as thermal and chemical resistance Lithium bis(trifluoromethylsulfonyl)imide (LiTFSI) is the most widely used electrolyte salt for Li-S batteries.[33] Beside that, Lithium bis(oxalato)borate (LiBOB), lithium difluoro(oxalato)borate (LiFBOB) and lithium hexafluorophosphate ($LiPF_6$) are also frequently used, while organic carbonates and ethers are generally applied as solvents.[32] Ether-based electrolytes enable high sulfur utilization and have a major benefit on electrochemical properties. It is also known, however, that these promote the negative shuttle effect.[2] Carbonate-based electrolytes are less corrosive and more stable to anodic oxidation than ether-based electrolytes, while showing better cycle stability under certain conditions.[24] Indeed, carbonates react with reduced sulfur species that are formed during battery cycling. Therefore, it is necessary to use a modified sulfur cathode that contains for example a high proportion of covalently bound sulfur.[34]

Suitable electrolyte systems for Mg-S batteries are still subject of intensive research. Due to the generally known incompatibility of sulfur with nucleophilic conductive salts, the focus is on electrolyte systems with non-nucleophilic nature. Numerous working groups presented promising solutions based on a non-nucleophilic magnesium salt in ethereal solvents. So far, the organic solvents tetrahydrofuran (THF), ethylene glycol dimethyl ether (DME), diethylene glycol dimethyl ether (DGM) and tetraethylene glycol dimethyl ether (TGDME) have been applied for that purpose.[24] Zhao-Karger *et al.* developed an efficient Mg-ion electrolyte based on Mg-borohydride.[35] The conductive salts are obtained by reacting $Mg[BH_4]_2$ with fluorinated alcohols (R^F-OH) in ethereal solvents (Equation 2.10).

$$Mg[BH_4]_2 + 8R^F - OH \rightarrow Mg[B(OR^F)_4]_2 + 4H_2 \uparrow \qquad (2.10)$$

The $Mg[B(hfip)_4]_2 \cdot 3\,DME$ salt is synthesized using fluorinated alcohol hexafluoro-2-propanol (hfip) and DME as a solvent. Figure 2.4 shows its crystal structure.

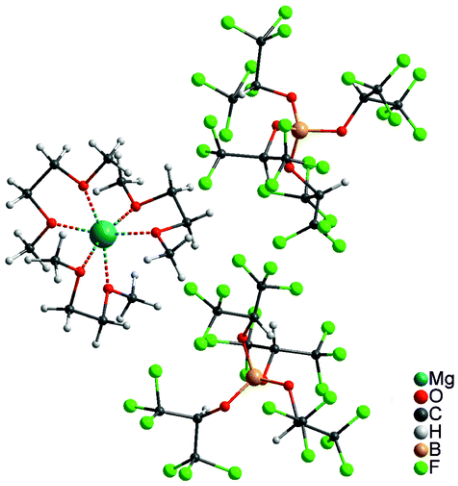

Figure 2.4: Ball-and-stick representation of the $Mg[B(hfip)_4]_2 \cdot 3$ DME salt.[35]

The Mg-ion is solvated by three DME molecules which lead to a distorted octahedral arrangement. The boron atom of the $[B(hfip)_4]^-$ anion is attached to four hexafluoroisopropyloxy groups which create a tetrahedral structure. The electrolyte features a high ionic conductivity (*approx.* $11\ mS \cdot cm^{-1}$ for 0.3 M $Mg[B(hfip)_4]_2 \cdot 3$ DME) as well as a sufficiently high thermal, chemical and electrochemical stability.[36]

2.2.4 Separator

The metal anode and the sulfur cathode are separated from each other by means of a separator in order to avoid current flow and thus to prevent an internal short circuit.[37] Porous insulators are used as separators, which have to meet a number of mechanical, chemical and physical requirements to ensure free ion transport between the two electrodes.[38] Furthermore, the separator also serves as a reservoir for the liquid electrolyte. The use of commercially available glass fiber separators and microporous polymer membranes is widespread.

2.2.5 Polysulfide shuttle

Minimizing the so-called polysulfide shuttle is seen as one of the greatest challenges in improving Me-S batteries. The shuttle effect describes the move of polysulfidic species between the two electrodes and causes significant coulombic loss, insulating deposits on the anode and low sulfur utilization.[39] Partially soluble polysulfides with different chain lengths S_x^{2-} ($2 \leq x \leq 8$) are formed during the step-by-step cathode reaction.[40] Figure 2.5 shows an exemplary discharge/charge profile of a Li-S battery with the polysulfide species formed.

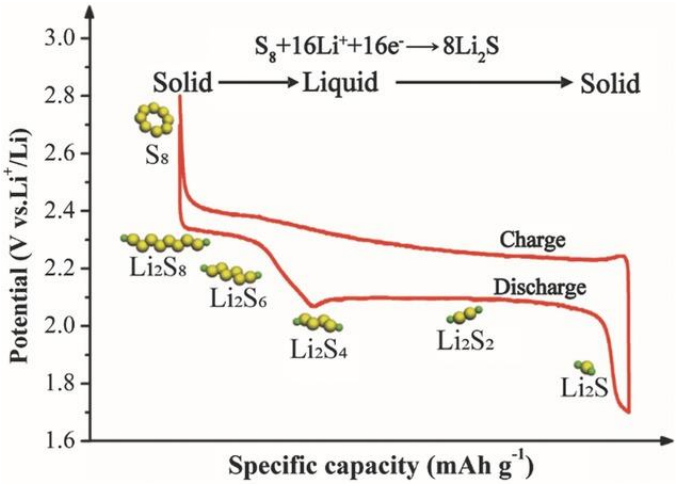

Figure 2.5: Discharge/charge profile including the formed polysulfide species at different state of charges (SOC) using the example of a Li-S battery.[2]

Soluble high-order polysulfides form a concentration gradient during the individual reaction stages and diffuse from the cathode to the anode side. Afterwards they are chemically reduced to low order polysulfides on the metal surface and deposited on the anode. This results in the loss of sulfur on the cathode side. Due to the further development of a concentration gradient short chain polysulfides partially diffuse back to the cathode. This process is repeated in every discharge/charge process. In addition to the influences mentioned above this leads to a constantly changing electrolyte viscosity due to different polysulfide concentrations as well as varying ion conductivities. It thus has a significant influence on the electrochemical processes of Me-S batteries.[41]

2.2.6 Solid electrolyte interface

The solid electrolyte interface (SEI) is a passivating boundary layer at the anode/electrolyte interface. The presence of an SEI on metal electrodes is a crucial parameter for the performance of metal-sulfur batteries.[42,43] It arises mainly during the first discharge/charge cycle due to the parasitic reduction reaction of the electrolyte components with the metal anode.[44] Ideally, a homogeneous passivating layer is formed that is ionically conductive but electronically insulating and mechanically flexible to some extent. Such layers hinder excessive continuous electrolyte decomposition and enables stable cycling without electrolyte consumption. It is also observed that the formation of harmful dendrites is minimized by the SEI.[7] However, the chemical composition of the SEI is complex and mechanically unstable and therefore does not show the optimal properties. In the case of sulfur-based batteries the interface phenomenon appears to be particularly complicated. Due to the polysulfide shuttle there are additional parasitic side reactions between the anode and migrated polysulfide species.[45] This leads to uneven stripping and plating of Li/Li^+ and promotes the formation of dendrites, which has a negative impact on safety. The nature of the SEI is largely influenced by the applied electrolyte system and might be tuned by the right choice of salt, solvent and further additives. In Li-S batteries electrolyte systems based on a linear ether such as DME are often used together with the cyclic ether 1,3-dioxolane (DOL). DME has a higher polysulfide solubility and a faster polysulfide kinetic in comparison to DOL, but is more reactive with respect to the metallic Li. DOL on the other hand can help to form a more stable SEI with improved mechanical properties.[43] Furthermore, lithium nitrate ($LiNO_3$) is an effective additive to improve the properties of the SEI.[46]

The interface behavior of Mg-S batteries has been hardly investigated so far and is therefore not fully understood yet. Although Mg-S is similar in its behavior to the Li-S system some differences are known. In addition to the formation of dendrites a blocking layer is formed on the Mg anode in many conventional electrolytes. This problem occurs primarily with polar aprotic solvents such as carbonates and nitriles and leads to the irreversibility of stripping and plating of Mg/Mg^{2+}, which is why the number of possible electrolyte solvents is limited (Chapter 2.2.3).[42,47] In addition, there is the generally slow solid phase diffusion of Mg^{2+}. However, if Mg-ions cannot diffuse with a certain rapidity through the blocking layer the cell's impedance increases significantly.[48] Nevertheless, it was shown that SEI with sufficiently high Mg^{2+} conductivity can be formed in suitable electrolyte systems and thus reversible stripping

and plating of Mg/Mg^{2+} is possible.[49,50] Gao *et al.* demonstrate a functioning *in-situ* SEI formed on the Mg anode, which enables reversible transport of Mg^{2+} and growth of the Mg deposit underneath.[51] The structure of the SEI proposed by Gao *et al*. on the anode of a Mg-S battery is shown in Figure 2.6.

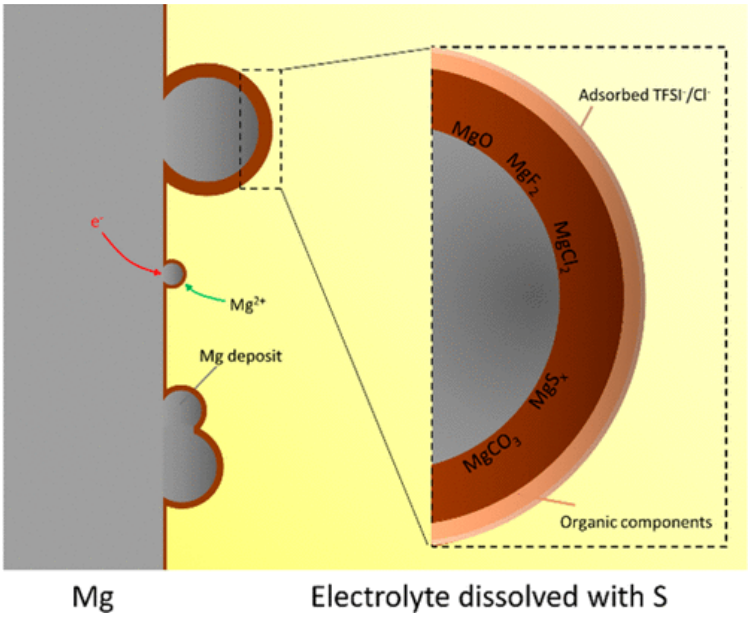

Figure 2.6: Structure of a SEI on the metal anode of a Mg-S battery.[51]

According to Figure 2.6 the SEI consists of three layers: organic components, the adsorbed electrolyte species bis(trifluoromethylsulfonyl)imide ($TFSI^-$) and chloride (Cl^-) as well as inorganic Mg compounds such as halides (MgF_2, $MgCl_2$), polysulfides (MgS_x), oxides (MgO) and carbonates ($MgCO_3$). Nevertheless, the individual composition depends largely on the electrolyte system used. The same group also showed the effectiveness of iodine as an additive in a $MgTFSI_2$/DME electrolyte for a functioning SEI.[52] In order to overcome the inherent disadvantages of the *in-situ* formed SEI most approaches rely on adjusting the electrolyte composition including solvents, salts or additives. However, innovations in electrode and cell configuration are also possible. Here, the implementation of an artificial *ex-situ* SEI with desired properties is a promising approach.

2.3 Artificial solid electrolyte interface on metal anodes

To circumvent the drawbacks of an *in-situ* formed SEI an artificial *ex-situ* SEI can be applied on the metal surface of the anode. Compared to other methods for modifying the anode (Chapter 2.2.1) this method is characterized by its feasibility, variety and controllability.[26] The main goals are the mechanical suppression of dendrites and the reduction of parasitic side reactions at the anode as well as a high selectivity for the transport of the metal ions.[15] Figure 2.7 shows a schematic comparison between Li anodes without and with a protective coating after cycling in the cell.

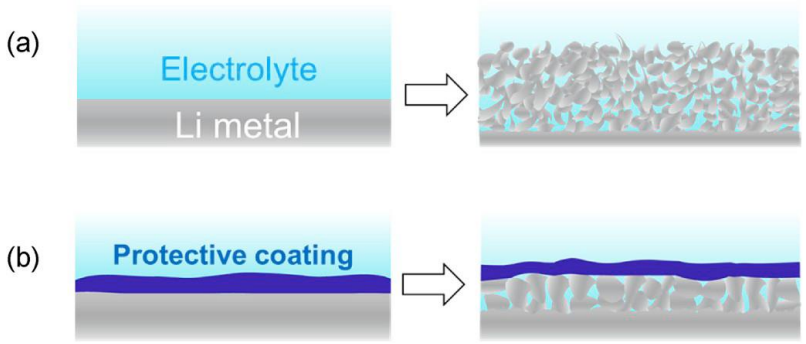

Figure 2.7: a) Porous morphology of a Li metal anode after cycling. b) Less porous morphology of Li metal after cycling under a protective artificial SEI.[15]

As shown in Figure 2.7 the electrodeposition of metal ions under the protective layer is possible and more evenly than on a pristine metal surface. Thus, dead lithium is avoided and a denser morphology is achieved. In addition, the contact area between the electrolyte and the metallic surface is minimized, which reduces parasitic consumption of the electrolyte. In order to protect the metal as effectively as possible and still ensure sufficient ionic conductivity there are some requirements the protective layer should meet. The protective layer must be chemically and electrochemically stable to metal and electrolyte under the operating conditions of the battery. It has to be mechanically stable to effectively prevent the formation of dendrites and still flexible to avoid cracks due to the change in volume during cycling. Moreover, the protective layer should be homogeneous to avoid a differing thickness and uncoated areas. Furthermore, the layer must be electronically insulating and still have excellent ion conductivity.[26] Coating materials have to combine these properties at the best possible rate. Different coating processes

can be used to influence the thickness, but also the homogeneity of the protective layer. Various approaches to the formation of artificial protective coatings are reported in the literature.[15] Depending on the method and coating material the layer thicknesses vary from the nanometer range to a few micrometers. The most widespread technology due to the comparatively simple and quick handling is the direct coating technology. This includes roll coating, doctor blading, dip coating, spin coating and the planetary milling technique. Spray or sputter coating techniques such as magnetron sputtering or airflow spraying can be used alternatively. These techniques promise high film purity, good compactness as well as uniformity. Chemical coating technologies offer another possibility. In this case, the protective coating is produced by a chemical reaction on the metal surface. This can be implemented for example by means of chemical graft modification, chemical vapor deposition or layer assembly.[6] Compared to direct coating and spray or sputter techniques these methods are more complicated to use.

2.3.1 Protection technology of lithium anodes

Artificial SEI for Li metal can be divided into two main groups: protective layers made of inorganic materials and protective layers made of polymeric materials. Due to their robustness and mechanical capabilities inorganic materials have been used for a long time for the coating of separators, current collectors and electrodes of batteries.[18] Metal oxides such as Al_2O_3 are widely used.[53] Jing *et al*. synthesized an Al_2O_3 coating for the anode of a Li-S battery by spin coating. Side reactions of the Li metal with polysulfides could be minimized and the surface morphology of the Li anode could be improved by the coating. Wang *et al*. have been able to increase the coulomb efficiency of a Li-S battery with an artificial SEI based on Li_3PO_4.[54] Furthermore, protective layers based on lithium fluoride, lithium methyl carbonate, lithium sulfide or lithium phosphorus sulfide are reported. [55–58]

Polymeric materials are more flexible than their inorganic representatives and better compensate for volume changes that occur during stripping and plating. Protective layers based on polymers also allow a more facile production using solution-based coating techniques (*e.g.* spin coating or solution casting).[26] Therein, the thickness of the layers can be controlled via viscosity of the polymer solutions. Another advantage is the simple possibility of modifying functional groups or adjusting the degree of crosslinking of the polymers. The influence on the properties of the artificial SEI is therefore exceptionally good. Beside non-polar polymers (*e.g.* poly(dimethylsiloxane) (PDMS)), polar polymers such as poly(vinylidenefluoride)

(PVDF), poly(3,4-ethylenedioxythiophene-co-ethyleneoxide) (PEDOT) or strongly-polar like poly(acrylonitrile) (PAN) or Nafion are known as coating materials.[15] Due to the special structural properties, particularly ionomers based on sulfonate are used frequently. Nafion shows polysulfide repelling characteristics and is highly selective towards cations.[59] The structure of these copolymers is composed of ionic groups that are bound to a non-polar polymer backbone in a phase-separated manner (Figure 2.8).[60]

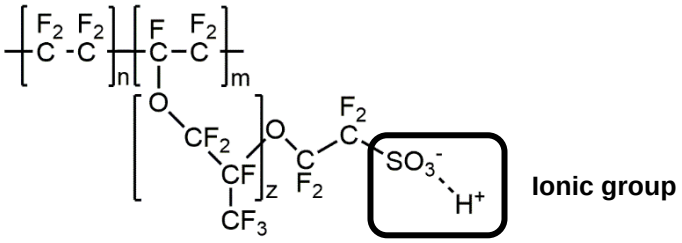

Figure 2.8: Structure of the Nafion ionomer.

On the one hand, the hydrophobic poly(tetrafluoroethylene) (PTFE) chain of the polymer backbone enables high mechanical stability. On the other hand, the hydrophilic area of the sulfonated side chains results in a high proton conductivity. The exchange of H^+ in the sulfonyl hydroxyl group by Li^+ creates a selective conductivity for Li-ions with high transference numbers.[61]

Luo *et al.* synthesized Nafion-based protective coatings on a Li anode using cast-coating solutions which simultaneously minimized the polysulfide shuttle and the growth of dendrites in a Li-S battery.[7] The working group found that the single use of Nafion in ether-based electrolytes (DOL/DME 1 M LiTFSI) leads to swelling of the polymer. This resulted in incomplete coverage of the anode surface. To reduce the swelling tendencies of Nafion they used a 1:1 mixture of Nafion and PVDF as coating material, which showed good mechanical strength. To characterize the electrochemical properties, Nafion and Nafion/PVDF coatings were tested in Li-S cells with high sulfur loading, concluding in the latter being superior. However, even cells with single Nafion coating showed better rate performance and cyclability with improved columbic efficiency than cells without a coating. Song *et al.* investigated Nafion-based protective coatings with several layer thicknesses in carbonate electrolytes (EC/DEC 1 M $LiPF_6$) in symmetrical Li-Li cells. They reported that ionic conductivity and consequently electrochemical properties improve with decreasing coating layer thickness.[62] Haensel *et al.*

presented the development of new sulfonate-based ionomers and suggested the use of sulfonated poly(etheretherketone) (SPEEK) in high-energy batteries.[8] Similar to Nafion the ion exchange of H^+ from the sulfonyl hydroxyl group leads to high ionic conductivities and cation transfer numbers.

2.3.2 Protection technology of magnesium anodes

Artificial SEI for Mg-S batteries are still in their infancy. Based on the knowledge from Li-S research it is known that protective layers can be effective for better battery operation. Many conventional electrolyte systems that contain carbonates or acetonitriles as solvents react deleteriously with the Mg surface of the anode and cannot be used in the Mg-S system.[47] The design of a suitable conductive and protective artificial SEI for the Mg anode is therefore of great importance to increase the variety of potential electrolyte solvents.

Chen *et al.* evaluated potential coating materials for Mg anodes in batteries with an intercalation cathode using a combination of the density functional theory and thermodynamic calculations. Based on their calculations they recommend Mg halides and $Mg(BH_4)_2$ as promising coating materials.[63] The same working group also calculated migration barriers and examined the associated ion transport ability of potential coating materials as shown in Figure 2.9.[64]

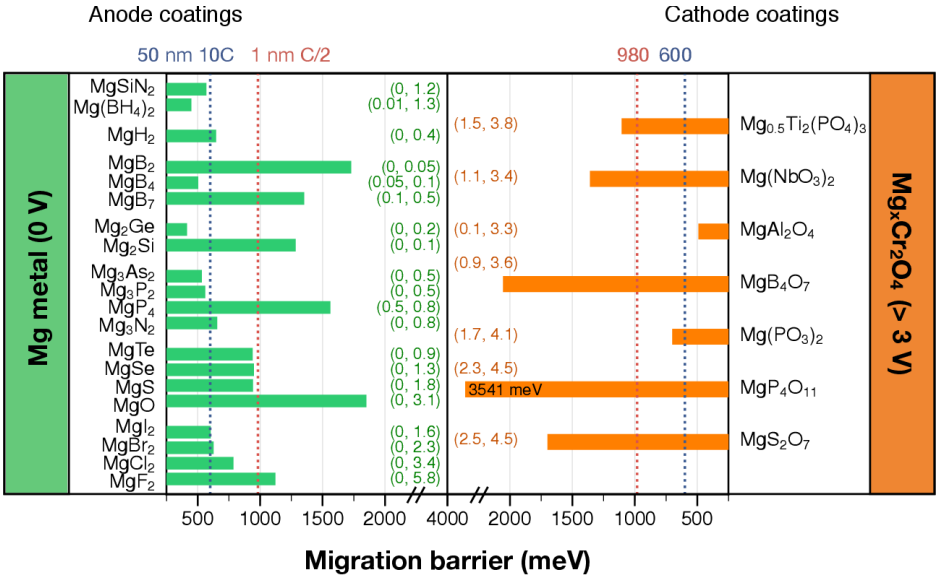

Figure 2.9: Migration barriers of potential coating materials for Mg, with the values of the reductive/oxidative stability limits in V vs. Mg. The migration barriers are compared against E_m^{max} values of 600 meV (50 nm + 25 °C + 10 C) and 980 meV (1 nm + 60 °C + C/2).[64]

Figure 2.9 shows the calculated migration barriers of potential coating materials for Mg anodes. Accordingly, $MgSiN_2$, MgB_4, Mg_2Ge, Mg_3As_2 and Mg_3P_2 are suitable for the Mg anode using a 600 meV mobility threshold. At a milder threshold, Mg selenide, Mg halides and Mg sulfide are also suitable, which have high reductive/oxidative stability limits as well.

In order to achieve more flexible coatings, the use of polymer materials like in the Li-S system can be useful. The feasibility of polymer-based artificial SEI was demonstrated by Son *et al.* who produced a PAN-based protective layer for the anode of a Mg-V_2O_5 battery. For this purpose, they applied a slurry consisting of thermal-cyclized PAN (cPAN), Mg trifluoromethanesulfonate, Mg powder and carbon black via cast coating to a stainless-steel foil. They achieved a Mg^{2+} conductive protective layer, which made reversible stripping and plating of Mg/Mg^{2+} possible – even in carbonate-based electrolytes.[9]

2.4 Characterization techniques

With suitable characterization techniques physical and chemical properties of the coating materials can be examined. Methods such as scanning electron microscope (SEM), Fourier-transform infrared spectroscopy (FTIR) or X-ray photoelectron spectroscopy (XPS) are often used to analyze the composition and morphology of coatings. For the *in-situ* investigation of the coatings during cell operation the electrochemical impedance spectroscopy (EIS) represents a powerful tool.

2.4.1 Scanning electron microscope

Scanning electron microscopy (SEM) is based on the usage of backscattered or secondary electrons to magnify small objects. It is mainly applied to analyze surfaces and their compositions. The grid-like scanning of the surface with a high-energy electron beam creates interactions with the surface of an object. These interactions are used to image micro- and nano-structured surface details. Due to small wavelengths of electrons (39 pm (1 keV) – 7.0 pm (30 keV)) details can be resolved better than in light microscopes. Objects can therefore be enlarged to a million times of their original size and features with a dimension of less than 1 nm can be resolved.[65] Figure 2.10 shows the schematic representation and the working principle of a SEM.

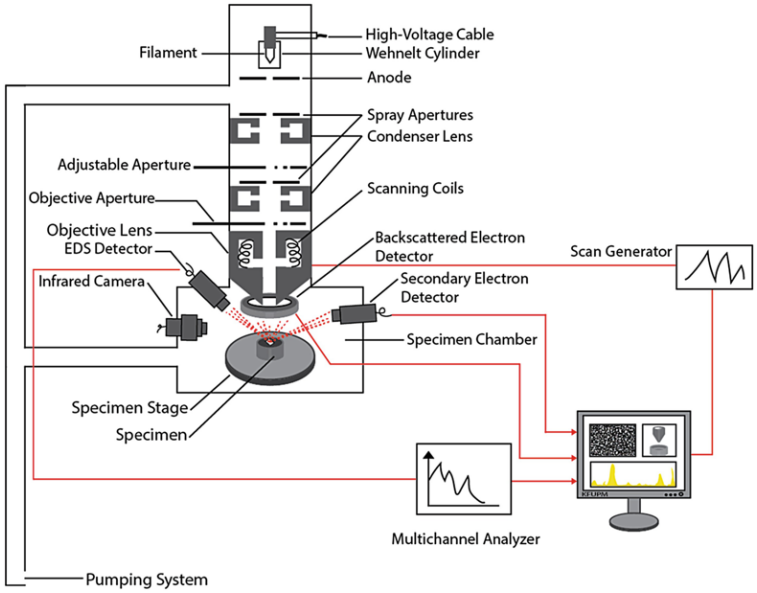

Figure 2.10: Schematic showing construction and working principle of the SEM.[65]

The most important components are the electron column, the sample chamber and the computer control system. Using SEM, a large variety of materials (*e.g.* metals, alloys, polymers, membranes) can be examined as received or prepared (*e.g.* coated, cut, etched). Conductive materials can be analyzed in solid or powder form. Further advantages are the simple sample preparation and the fast imaging. Large depths of the sample can also be analyzed. SEM is often combined with energy-dispersive X-ray spectrometry (EDX) to provide information about composition along with morphology.[15] EDX is based on the interactions between the X-ray radiation that is generated during electron bombardment and the atoms of the sample. The most important interaction processes are the absorption and fluorescence of the X-rays as well as the deceleration of primarily electrons. Depending on the depth of the electron beam entering the sample material there is an activation volume which defines the volume in which interaction processes can be recorded and used for elemental analysis. The material-dependent entry depth of the electron beam results in an activation volume between several hundred nm^3 and a few μm^3.[66]

2.4.2 Fourier-transform infrared spectroscopy

Fourier-transform infrared spectroscopy (FTIR) is a frequently used method to analyze the structure of individual molecules or molecular mixtures and to identify substances. In FTIR spectroscopy the sample is irradiated with electromagnetic radiation in the mid-infrared wavelength range. Certain wavelengths are absorbed by the sample material to stimulate molecular vibrations. In the resulting spectrum absorption wavebands are observed that are characteristic of the molecule or its bonding structure under investigation. For data recording a Michelson interferometer is usually used to analyze the signal. The spectrum is calculated by using the Fourier transform of the measured interferogram.[67] In order to obtain the typical infrared absorption/transmission spectrum the measured intensity-time signal is converted into an intensity-frequency signal. To remove background contributions the single-beam sample spectrum is compared with a reference spectrum.[68]

2.4.3 X-ray photoelectron spectroscopy

X-ray photoelectron spectroscopy (XPS) is a powerful surface-specific analysis tool whose operation principle is based on the photoelectric effect. Surfaces can be examined at a sample depth between 3.0 nm – 10.0 nm at A 1 Kα radiation. For analysis the sample is irradiated with

X-rays of a suitable wavelength which leads to the emission of electrons from lower electron shells.[69] The kinetic energies E_{kin} of the emitted electrons can then be used to calculate the binding energy E_{bond} which is specific to each chemical element.[70]

$$E_{bond} = E_{photon} - E_{kin} - \phi \tag{2.11}$$

with E_{photon} = X-ray energy, ϕ = work of emission.

This enables chemical species to be identified and the ratio of compound on the sample surface to be quantified. Compared to SEM-EDX, XPS is better suited for the accurate characterization of surface layer compositions due to its high surface sensitivity.

2.4.4 Electrochemical impedance spectroscopy

Electrochemical impedance spectroscopy (EIS) is one of the standard methods for the investigation of electrochemical systems such as batteries and their electrodes. It is an *in-situ* method that provides knowledge about the various processes during ongoing test operations. To measure the impedance Z a sinusoidal input signal with a sufficiently large amplitude is applied to the electrochemical system to be examined. The likewise sinusoidal response signal has the same frequency, but a different amplitude and phase. Therefore, the impedance is also generally referred to as an alternating current resistance and is calculated from the ratio between the input signal and the response signal. The impedance spectrum is obtained by varying the frequency of the input signal (typically from few MHz down to the mHz region).[71] A distinction is made between potentiostatic and galvanostatic measurement. With the potentiostatic method a voltage signal is impressed and the current response is measured, whereas in the galvanostatic method a current signal is impressed and the voltage response is measured. By measuring the impedance, qualitative statements about mechanisms, kinetics, structure and topology can be made. In addition, quantitative information about the impedance elements of the resistances, capacitances and diffusion can be gained. To obtain this information, electrical equivalent circuit models (ECM) must be defined. The parameters of the ECM are determined by fitting the measured impedance data. In battery technology, resistors, capacitors and coils are commonly used to create the ECM (Table 2.1).[72]

Table 2.1: Elements frequently used in battery technology to create the ECM.

Element	Symbol
Resistance *R*	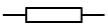
Capacity *C*	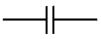
Inductance *L*	
Warburg element *W*	
RC-circuit	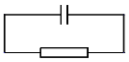

The impedance spectrum of a battery typically contains information about the electrolyte conductivity, diffusion layer and charge transfer at the electrode surface.[73] The spectra are usually displayed by plotting the imaginary part against the real part of the impedance (Nyquist plot). Furthermore, the representation in a Bode diagram is widespread. Therein, the absolute values of phase and impedance are plotted as a function of the frequency.[74]

3 Experimental

This chapter describes the experimental procedure as well as the chemicals and methods used for the production and characterization of *ex-situ* artificial SEI for Me-S batteries.

3.1 Chemicals

All solvents were obtained extra dry under inert gas atmosphere and stored in a glovebox under argon atmosphere (H_2O < 1 ppm; O_2 < 3 ppm) without further treatment. The metal foils Mg, Li as well as the salts $Mg[B(hfip)_4]_2$, Mg trifluoromethanesulfonate and LiTFSI were also stored in a glovebox. Other chemicals in powder form were vacuum dried before use. Air and humidity sensitive work was carried out in gloveboxes GPT4FF from *Jacomex* and Mega 4 E-line from *Glovebox Systemtechnik* under an argon atmosphere at H_2O < 1 ppm and O_2 < 3 ppm. Table 3.1 lists the supplier of the chemical compounds as well as their purities.

Table 3.1: Producer and purity of the chemicals used.

Chemical	**Purity / %**	**Producer**
1,3-Dioxolane (DOL)	99.8	Acros Organics
Aquivion (PW 795)	-	Sigma-Aldrich
Carboxymethyl cellulose (CMC, CRT 2000 PA)	-	Dow Wolff Cellulosics
Diethyl carbonate (DEC)	99.9	Acros Organics
Dimethylacetamide (DMAc)	99.5	Acros Organics
Dimethylformamide (DMF)	99.5	Acros Organics
Hydrocarbon sulfonated poly(phenylene sulfone) (s-PSO2-220)	-	MPI
Ketjenblack EC 600-JD	-	Akzo Nobel
LiTFSI	99.95	Sigma-Aldrich
Lithium foil	99.9	Alfa Aesar
$Mg[B(hfip)_4]_2 \cdot 3$ DME	-	KIT
Magnesium foil	-	Gelon
Magnesium powder	99.8	Alfa Aesar
Magnesium trifluoromethanesulfonate	98.0	Alfa Aesar
Monoglyme, Ethyleneglycoldimethylether (DME)	99.5	Acros Organics
Nafion (NR 50)	-	Fuel Cell Store

Poly(acrylonitrile) (PAN)	99.5	Goodfellow
Poly(ethyleneoxide) (PEO)	-	Acros Organics
Poly(vinylidene fluoride) (PVDF)	-	Solvay
Propylene carbonate (PC)	99.9	Acros Organics
Styrene-butadiene rubber (TRD 102A)	40.4	JSR Micro
Sulfonated poly(etheretherketone) (SPEEK)	-	MPI
Sulfur	99.5	Alfa Aesar
Tetrahydrofuran (THF)	99.9	Sigma-Aldrich

3.2 Metal anode

A 100 µm thick Mg foil was used as the Mg electrode. The natural oxide layer on the surface of the foil was scraped off outside the glovebox on the top and bottom side using a glass object slide. The foil was stored in the glovebox until further use. For battery assembly, anodes with a diameter of 18 mm were punched out of the foil and the oxide layer was scraped off again on both sides using a spatula. The anodes were then used directly for cell construction or coated with an artificial SEI.

Li electrodes with a diameter of 18 mm were punched out of a 750 µm thick lithium foil. The foil was used as received or coated with an artificial SEI.

3.2.1 Coating solutions for magnesium anodes

Coating solutions (inks) for Mg substrates were prepared in air atmosphere. The sulfone-based ionomers s-PSO2-220, Aquivion, Nafion and SPEEK were used as active material in the coatings. PVDF was used as a stabilizer. The structures of the repetition units of the ionomers as well as PVDF are shown in Figure 3.1.

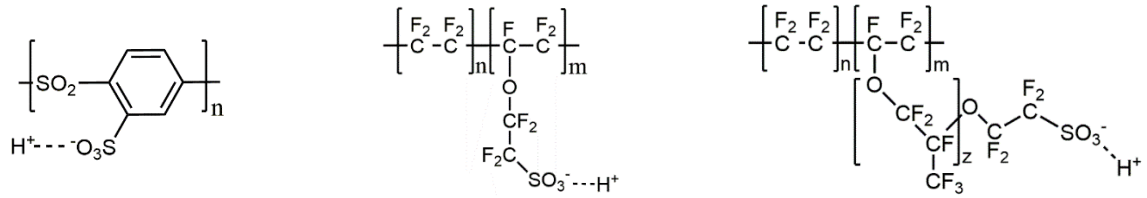

s-PSO2-220 Aquivion Nafion

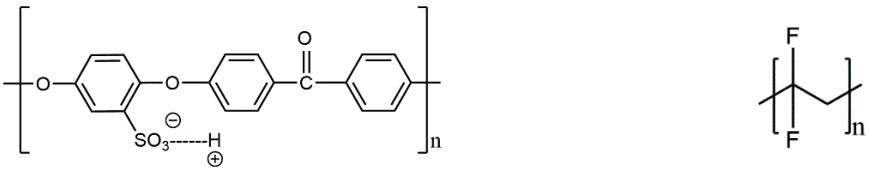

SPEEK PVDF

Figure 3.1: Repetition units of s-PSO2-220, Aquivion, Nafion, SPEEK and PVDF.

Powdered s-PSO2-220 (Figure 3.1) was synthesized and made available by Kreuer *et. al* at the *Max Planck Institute for Solid State Research* in Stuttgart. Nafion was pulverized by means of cryogenic grinding (liquid nitrogen, -196 °C). Other ionomers as well as PVDF were used without further pretreatment. Coating solutions were produced with a solids content of 2.5 wt.% and dimethylacetamide (DMAc) as solvent with stirring at 500 rpm. The polymers were dissolved and subsequently mixed in a ratio of 1:1 with a PVDF solution as stabilizer. Table 3.2 shows the solubility behavior of the individual polymers.

Table 3.2: Solubility behavior of the polymers with a solids content of 2.5 wt.% in DMAc with stirring at 500 rpm.

Polymer	**Temperature *T* / °C**	**Time *t* / h**
PVDF	25	14
s-PSO2-220	100	14
Aquivion	100	2
Nafion	100	14
SPEEK	100	2

In addition, PAN (Figure 3.2) was used as a coating component especially for the Mg anode.

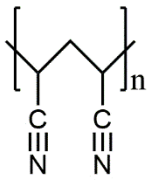

Figure 3.2: Structure of the PAN polymer.

PAN (3.4 wt.%) was dissolved in DMF under an argon atmosphere by stirring at 500 rpm. Dry Mg trifluoromethanesulfonate (PAN:Mg trifluoromethanesulfonate 10:3) was filled into an Erlenmeyer flask and the previously prepared PAN solution was added dropwise while stirring with a magnetic stirrer. The salt has been dissolved for at least three hours afterwards. Further processing was carried out using spin coating. The produced PAN coatings have been stored for one hour at 250 °C under vacuum (-900 mbar) in order to trigger ring polymerization of the PAN polymer.[9]

3.2.2 Coating solutions for lithium anodes

Coating solutions (inks) for Li anodes were prepared with previously dried ionomers s-PSO2-220, Aquivion, Nafion and SPEEK (80 °C, -900 mbar, 14 h) and extra dry solvents in the glovebox. Apart from that, preparation and composition of the solutions were carried out analogously to Chapter 3.2.1.

For coatings using the s-PSO2-220 ionomer a proton exchange of the H^+ ion to Li^+ ion was carried out. For this purpose, a column was packed with Amberlit IR 120 hydrogen ion exchange resin from *Sigma Aldrich*. The resin was loaded with Li^+ ions by repeated rinsing with 1 M aqueous LiCl solution (3x 300 ml). s-PSO2-220 powder was dissolved in demineralized water at 80 °C and then slowly rinsed through the Li^+ resin (15 min resting time). The obtained lithiated s-PSO2-220 solution has been dried for two days at 80 °C *in vacuo* (-1 bar) and transferred to the glovebox in powder form afterwards.

3.2.3 Coating techniques

In this thesis, the solvent-based coating technologies spin coating and dip coating were used to produce artificial SEI. The general procedure for the individual coating techniques is explained in the following.

Spin coating

Spin coating is a simple process for producing thin films on a substrate. In addition to adjustable parameters such as spin speed or duration, the thickness of the coating is influenced by the viscosity of the coating solution. Artificial SEI were produced with a SPIN 150i spin coater from *SPS*. A picture with main components of the spin coater is shown in Figure 3.3.

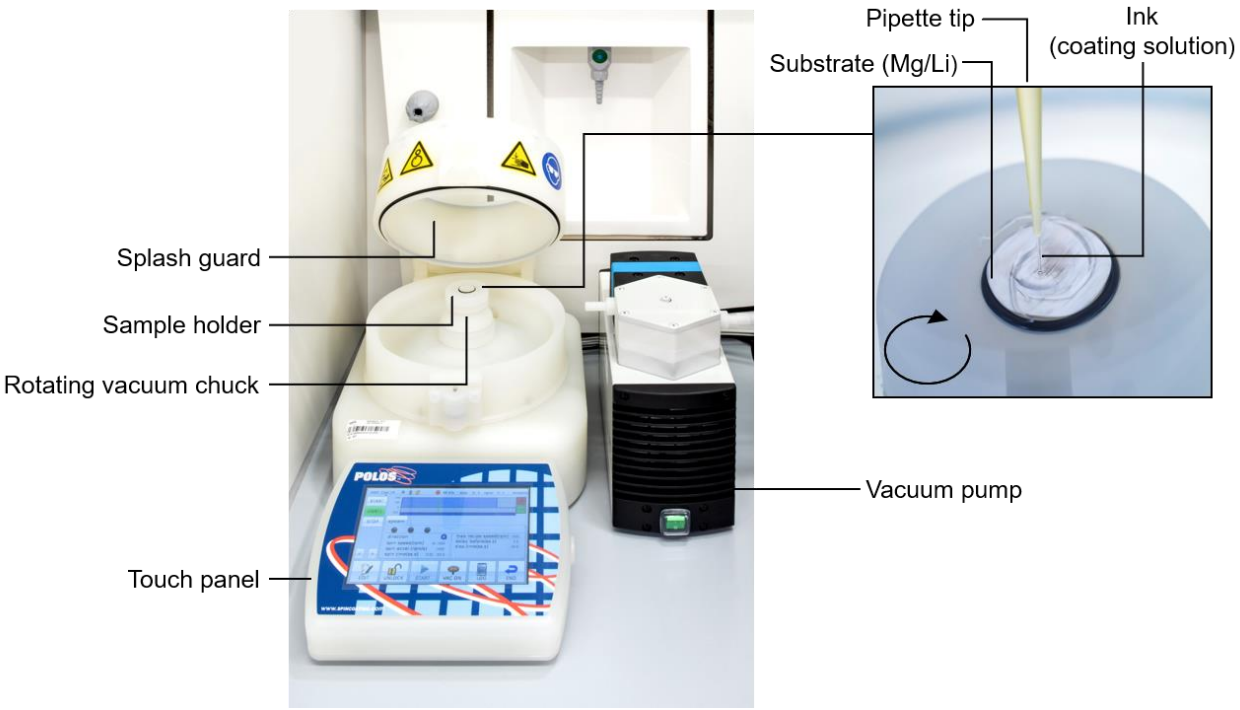

Figure 3.3: Picture of the SPIN 150i spin coater used for the coating of the metal anodes.

The most important components are the touch panel for programming the spin coater, the rotating vacuum chuck with sample holder as well as the vacuum pump. Substrates with a diameter of 18 mm were placed in the middle of the sample holder and fixed by means of vacuum exhaust. The coating was done with the dynamic spin method (adding the solution at

full spin speed). Previously produced coating solutions (Chapter 3.2.1 and 3.2.2) were pipetted with an Eppendorf pipette as close as possible to the center of the substrate without touching it. By default, 150 µl of coating solution was injected quickly and evenly at a spin speed of 1000 rpm. Figure 3.4 shows the application of the coating solution and a coated substrate.

Figure 3.4: Application of coating solution at full spin speed (left) and coated substrate (right).

The subsequent spin period was 30 s in order to spin the substrate until the coating had dried (spin till dry). To ensure that excess solvent had evaporated, the coated substrate was air-dried for a few minutes. The substrate was then transferred to the glovebox for cell assembly.

Dip Coating

Dip coating is a flexible and fast coating method and is therefore suitable to produce thin layers. Coatings were produced under air (Mg coatings) as well as argon atmosphere (Li coatings). For this purpose, 4 ml of coating solution were filled into a Petri dish (100 mm x 20 mm). The surfaces of the substrates (Li/Mg) with diameters of 18 mm were wetted by pulling through the coating solution once. Care was taken to coat the surface as evenly as possible and to not completely immerse the substrates in the solution. Afterwards the coating was dried for at least 45 min at ambient temperature.

3.3 Other cell components

The components that have been used in addition to the varying anodes for cell assembly namely the sulfur cathode, electrolyte and separator are described in the following.

3.3.1 Sulfur cathode

Sulfur/Ketjenblack (ball milled)

Ketjenblack was vacuum dried overnight at 100 °C and then transferred into the glovebox. Sulfur (S) (m = 4.50 g) and Ketjenblack (KB) (m = 3.60 g) were weighed into a zirconium oxide grinding beaker. The mixture was ball milled in a Pulverisette 7 planetary ball mill from *Retsch* for 15 min at 600 rpm. Zirconium oxide balls (approx. 100 g) with a diameter of five millimeters were used for grinding. A part of the ball milled mixture (m = 2.25 g) was weighed into a slurry vial together with an aqueous 3.7 wt.% carboxymethyl cellulose (CMC) binder solution (m = 2.61 g). Deionized water was added to a solids content of 30 wt.%. The vial was sealed airtight and the mixture was stirred overnight at 400 rpm at room temperature. An aqueous 40.4 wt.% styrene-butadiene rubber (SBR) binder solution (m = 0.42 g) was subsequently added to achieve a ratio of 50:40:10 S:KB:CMC/SBR (1:2). The slurry was stirred for a further three hours at room temperature.

Doctor blading

The previously produced 50:40:10 S:KB:CMC/SBR (1:2) slurry was coated onto a 20 µm carbon-primed aluminum foil using doctor blading. The coating process is shown in Figure 3.5.

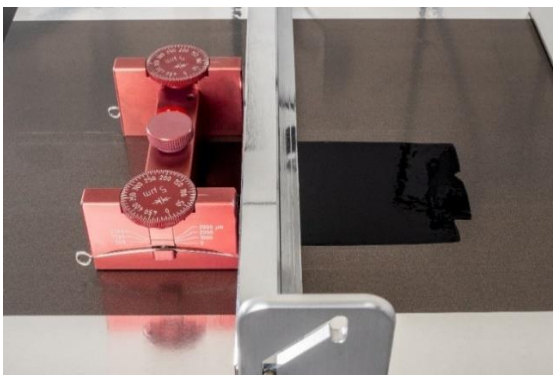

Figure 3.5: Sulfur cathode preparation using doctor blading.

A ZAA 2300 Automatic Film Applicator with a ZUA 200 Applicator from *Zehntner* was used to produce cathode coatings. The wet layer thickness was set to 90 µm. Coatings were dried at room temperature and cathodes with a diameter of 18 mm were stamped out. Subsequently the cathodes were dried *in vacuo* prior to use (80 °C, -0.5 bar, 2 h). The sulfur loading of the cathodes is 1.0 $mg \cdot cm^{-2}$.

Sulfur/Ketjenblack (melt infiltration)

Melt infiltrated S/KB cathodes with a S:KB:binder ratio before infiltration of 54:36:10 were used in Li-S cells. CMC and poly(ethyleneoxide) (PEO) in a ratio of 3:7 were used as binders. After drying, a sulfur content of 45% was determined by means of thermogravimetric analysis (TGA). Cathode coatings were produced by doctor blading as shown above. With a wet layer thickness of 50 µm, the stamped out cathodes (diameter of 18 mm) have a sulfur loading of 0.45 $mg \cdot cm^{-2}$.

Sulfur/Carbon – Aerogel (gas infiltration)

Gas infiltrated Sulfur/Carbon-Aerogel cathodes (S/CA) were produced with CMC and PEO as binders (3:7 CMC:PEO) in a ratio of 50:40:10 S:CA:binder for usage in Li-S cells. TGA shows a sulfur content of 20% after drying. The sulfur loading of the cathodes, which were produced with a wet layer thickness of 180 µm (doctor blading) was 0.5 $mg \cdot cm^{-2}$ (diameter of 18 mm).

3.3.2 Electrolyte

All electrolyte solutions were prepared and stored under an argon atmosphere. In Mg-S cells a 0.2 M $Mg[B(hfip)_4]_2$ in DME electrolyte solution was used, whereas a 1 M LiTFSI in DOL/DME electrolyte was prepared for usage in Li-S cells.

0.2 M $Mg[B(hfip)_4]_2$ in DME

$Mg[B(hfip)_4]_2 \cdot 3$ DME was synthesized and made available by Zhao-Karger *et al.* at the *Karlsruhe Institute for Technology* (KIT). For 5 ml of a 0.2 M electrolyte solution the salt (m = 1.652 g; n = 0.001 mol) was dissolved in 3.75 ml DME overnight with stirring at 500 rpm at ambient temperature and filtered with a syringe filter before use.

1 M LiTFSI in DOL/DME

To prepare 5 ml of 1 M electrolyte solution, LiTFSI (m = 1.435 g; n = 0.005 mol) was dissolved in a 1:1 by volume solvent mixture of DOL and DME. To completely dissolve the salt the mixture was stirred at 500 rpm for a few hours at ambient temperature. The electrolyte solution was filtered with a syringe filter before use.

3.3.3 Separator

Binder-free Whatman® GF/C glass fiber separators with pore sizes < 1.2 µm and a thickness of 260 µm were used in cells with Mg anodes. Separators with diameters of 21.6 mm and 18.0 mm were stamped out for cell construction with ECC-PAT-Core cells (Chapter 3.4.1). Before use, the separators were dried for 48 h at 120 °C *in vacuo* (-900 mbar).

Cells with Li anode were assembled with 25 µm thick polypropylene Celgard® 2500 separators with diameters of 21.6 mm and pore sizes of 0.64 µm. Applied separators were dried *in vacuo* bevor use (60 °C, -900 mbar, 14 h).

3.4 Electrochemical characterization

Electrochemical experiments were carried out in stainless-steel ECC-PAT-Core cells from *EL-Cell*. Cell assembly was done in an argon filled glovebox. The cell consists of a cell base with reference pin, lower plunger, insulation sleeve, upper plunger, lid with PE-seal and spring as well as the electrodes, separator and electrolyte. An assembled cell and the individual cell parts are shown in Figure 3.6.

Figure 3.6: ECC-PAT-Core cell with cell holder (left). Consisting of cell base with reference pin, lower plunger, insulation sleeve, upper plunger and lid with PE-seal and spring (from left to right).

3.4.1 Cell assembly

For electrochemical experiments, Mg-S and Li-S full cells as well as symmetrical Mg-Mg cells were assembled.

Mg-S full cells

To collect half-cell impedance spectra, Mg-S full cells were built in a three-electrode assembly with a Mg reference ring from *EL-Cell*. The outer clips ring of the insulation sleeve was equipped with a stainless-steel reed contact as described in Figure 3.7. A GF/C separator with a diameter of 21.6 mm was placed on the reference ring. The insulation sleeve was turned over

and a second GF/C separator with a diameter of 18 mm was placed inside. The Mg anode was fixed on top with a 300 µm thick lower plunger. Subsequently, the insulation sleeve was turned again and the separators were wetted with 200 µl of the 0.2 M $Mg[B(hfip)_4]_2$ in DME electrolyte. The cathode was fixed with the upper plunger and the closed cell was installed in the cell holder. For galvanostatic cycling tests a two-electrode arrangement without Mg reference ring was used.

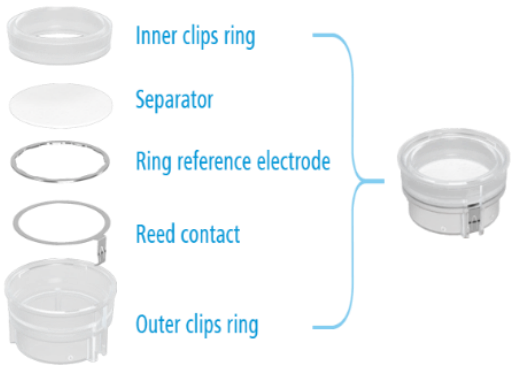

Figure 3.7: General assembly of the insulation sleeve with inner and outer clips rings, reed contact, ring reference electrode and separator.[75]

Mg-Mg symmetrical cells

Mg-Mg symmetrical cells were built analogously to Mg-S full cells with Mg reference ring. A second identical Mg anode was used instead of the cathode.

Li-S full cells

Li-S full cells were built in a two-electrode arrangement. A Celgard® 2500 separator with a diameter of 21.6 mm was placed directly on the reed contact. Afterwards, the sleeve was closed with the inner clips ring. The closed insulation sleeve was turned over and the sulfur cathode was placed and fixed with a 50 µm thick lower plunger. The sleeve was installed in the cell base and the separator was wetted with 100 µl 1 M LiTFSI DOL/DME electrolyte. Finally, the Li anode was placed and fixed with the upper plunger. The closed cell was carefully installed in the cell holder and sealed airtight using the wing nut.

3.4.2 Galvanostatic cycling

Galvanostatic cycling tests were carried out with a *BaSyTec* battery test system at a constant temperature of 25 °C in a climatic chamber. The tests was performed at constant C-rates which were defined by the theoretical capacity of sulfur (1 C = 1675 $Ah \cdot kg^{-1}$). Mg-S cells were cycled at a C-rate of C/10 after 1 h rest at OCV without any forming process. Forming of Li-S cells was carried out at C/10, whereas the cells were cycled with C/3. The respective test plans are given in Figure 3.8 and Figure 3.9.

	Ebene	Label	Befehl	Parameter	Abbruchkriterium	Aktion	Registrierung	Kommentar
1			Start					
2			Pause		t>1h		t=30s U=10mV	
3			Cycle-start					
4			Set	Ah-Set=0Ah t-Set=0s				
5			Discharge	I=167.5A/kg	U<50mV&t>5s		t=5s U=5mV	C/10
6			Set	Ah-Set=0Ah t-Set=0s				
7			Charge	I=167.5A/kg	U>3000mV&t>5s t>10h		t=5s U=5mV	C/10
8			Cycle-end	Count=500				
9			Stop					

Figure 3.8: Test plan for galvanostatic cycling of Mg-S cells.

	Ebene	Label	Befehl	Parameter	Abbruchkriterium	Aktion	Registrierung	Kommentar
1			Start		U>4V&t>1s U<0.5V&t>1s T1>80°C			
2			Pause		t>12h		U=50mV	
3			Cycle-start					
4			Set	Ah-Set=0Ah t-Set=0s				
5			discharge	I=167.5A/kg	U<1V&t>1s		U=5mV	
6			Set	Ah-Set=0Ah t-Set=0s				
7			Charge	I=167.5A/kg	U>3.3V&t>1s t>12h		U=5mV	
8			Cycle-end	Count=3				
9			Pause		t>10s			
10			Cycle-start					
11			Set	Ah-Set=0Ah t-Set=0s				
12			discharge	I=558.333A/kg	U<1V&t>1s		U=5mV	
13			Set	Ah-Set=0Ah t-Set=0s				
14			Charge	I=558.333A/kg	U>3.3V&t>1s t>3h		U=5mV	
15			Cycle-end	Count=1000				
16			Stop					

Figure 3.9: Test plan for galvanostatic cycling of Li-S cells.

3.4.3 Electrochemical impedance spectroscopy

EIS measurements were carried out with a three-electrode assembly with a Mg reference ring in symmetrical Mg-Mg cells as well as Mg-S cells (Chapter 3.4.1) using a *Zahner* ZENNIUM or IM6 workstation. The evaluation was carried out using RelaxIS3 from *rhd instruments*. The respective workstation was connected to a CTS LAB 733 potentiostat from *BaSyTec* with a customized switch.

Mg-Mg symmetrical cells

Half cell (HC) EIS measurements were carried out as described in Figure 3.10 between the reference electrode (RE) and the working sense electrode (WE-Sense). The two-electrode potential was logged between the working electrode (WE) and the counter electrode (CE).

Figure 3.10 illustrates the cell connections of the ECC-PAT-Core cells and a schematic representation of the cell assembly.

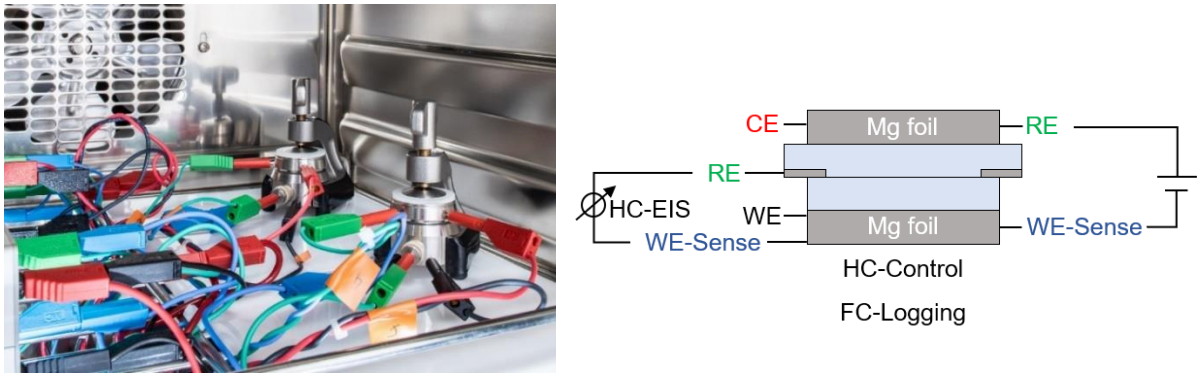

Figure 3.10: Cabling of the ECC-PAT-Core cells for EIS measurements and a schematic representation of the cell assembly of symmetrical Mg-Mg cells with Mg reference ring.

Impedance measurements were performed in a frequency range between 100 mHz – 0.3 MHz at room temperature. The cells were held at OCV for 50 h with EIS spectra being recorded potentiostatic at 5 mV amplitude immediately after the cell assembly as well as after 5 h, 10 h, 20 h, 30 h, 40 h and 50 h. After OCV, pseudo-galvanostatic impedance measurements were carried out. Therefore, a constant polarization current of 0.1 $mAh \cdot cm^{-2}$ was applied and oscillated around it with an amplitude of 5 mV. Ten galvanostatic cycles, each with a 10 min resting time between the cycles, were performed. EIS spectra were recorded in the cycles 1, 2, 3 and 10. Afterwards, the cell was held at OCV for 10 h and the processes were repeated at the polarization currents 0.2 $mA \cdot cm^{-2}$, 0.5 $mA \cdot cm^{-2}$ and 1.0 $mA \cdot cm^{-2}$. At the end of the measurements, another ten galvanostatic cycles were carried out with the initial polarization current of 0.1 $mA \cdot cm^{-2}$.

Mg-S full cells

A schematic representation of the cell assembly of Mg-S cells with Mg reference ring is shown in Figure 3.11.

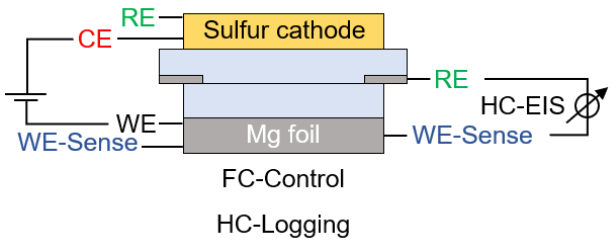

Figure 3.11: Schematic of the cell assembly of Mg-S cells with Mg reference ring.

The impedance was measured between RE and WE-Sense in a frequency range between 100 mHz – 1 MHz at room temperature. It was measured pseudo-galvanostatic during the first ten galvanostatic cycles at a constant current of 0.1 $mA \cdot cm^{-2}$ in a voltage range between 0.05 V – 3.0 V. The OCV was registered by means of HC-logging between the RE and WE-Sense using a second test channel.

3.5 Micro- and spectroscopic characterization

SEM and XPS analysis were carried out at the *Institute for Technical Thermodynamics* at the *German Aerospace Center* (DLR). IR spectroscopy was carried out at the *Institute of Inorganic Chemistry* at the University of Stuttgart.

Scanning electron microscope

SEM images were taken with an ULTRA Plus microscope from *Zeiss*® using an SE and ESB detector. Images of the samples were taken at 30x, 70x, 400x and 1000x magnification. SEM analysis were usually carried out in combination with EDX for which a QUANTAX 400 spectrometer with XFlash® detector 5010 from *Bruker*® was used.

X-ray photoelectron spectroscopy

XPS samples were placed in a transfer shuttle together with a gold metal foil serving as reference material under an argon atmosphere and after transfer from the glovebox directly connected to the XPS ante chamber. Spectra were recorded with a *Thermo Fisher Scientific* ESCALAB 250. A hemispherical analyzer was used in an ultrahigh vacuum chamber with a base pressure of $4 \cdot 10^{-4}$ mbar together with an A 1 Kα source XR4 from *Thermo Fisher Scientific* as the electron source. Peak fitting was done using UNIFIT.

Fourier-transform infrared spectroscopy

Infrared spectra of coated anodes and powdered samples were recorded with a Nicolet iS5 FTIR-spectrometer from *Thermo Fisher Scientific*. The evaluation was carried out using OMNIC.

4 Results and discussion

This chapter presents the gained results from the characterization of organic-based coatings as artificial SEI on Mg and Li metal anodes. Therein, the findings of the characterization using XPS, SEM and FTIR spectroscopy as well as the results of the electrochemical experiments in Mg-S, Mg-Mg as well as Li-S cells are presented and discussed.

4.1 Solvent compatibility with magnesium anode

Using XPS analysis, the chemical compatibility of the polar aprotic solvents DME, THF, DMAc, DMF, PC and DEC with the Mg anode was examined. One of the main distinguishing features of theses solvents is the solvent polarity, which is expressed by the relative permittivity. With increasing permittivity the solvent polarity and thus the ionic conductivity increases.[8] In addition, lower donor numbers lead to stronger solvation. Table 4.1 shows the values of the relative permittivities as well as the donor numbers, density, boiling and melting temperatures of the selected solvents.[76–79]

Table 4.1: Properties of the solvents DME, THF, DMAc, DMF, PC and DEC.

	DME	**THF**	**DMAc**	**DMF**	**PC**	**DEC**
Chemical formula	$C_4H_{10}O_2$	C_4H_8O	C_4H_9NO	C_3H_7NO	$C_4H_6O_3$	$C_5H_{10}O_3$
Density (20 °C) / g · cm^{-3}	0.87	0.89	0.94	1.03	1.21	0.98
Melting temperature / °C	-58	-109	-20	-61	-49	-43
Boiling temperature / °C	84	65	165	153	242	126
Relative permittivity	7.2	7.5	37.8	38.3	66.1	2.8
Donor number / kcal · mol^{-1}	18.6	20.0	27.8	26.6	15.1	16.0

The recorded Mg 2p spectra of Mg anodes immersed the respective solvent for 24 h as well as the spectrum of a Mg anode without solvent contact are illustrated in Figure 4.1.

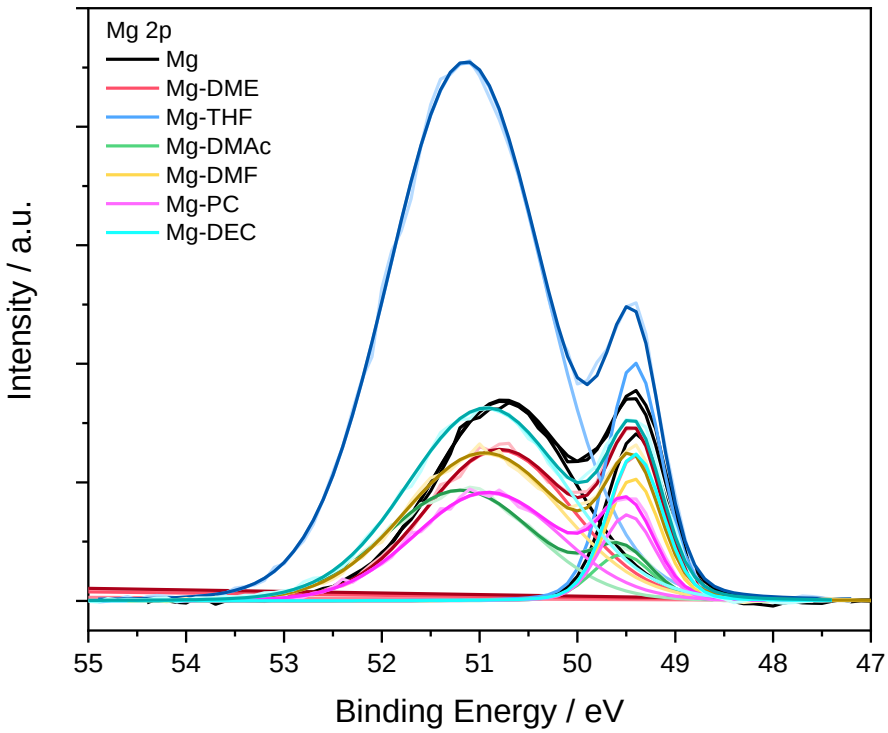

Figure 4.1: XPS Mg 2p spectra of Mg anodes that were contacted with various solvents (DME, THF, DMAc, DMF, PC, DEC) and spectrum of a Mg anode without solvent contact.

The Mg 2p spectra show an intense peak at 49.4 eV, which is assigned to elemental Mg. All peaks between 50.8 eV and 51.1 eV correspond to magnesium oxide (MgO) and confirm the expected formation of a MgO migration barrier due to the highly reductive properties of Mg.[80]. For the pristine Mg reference sample, the comparison of the percentage of the MgO peak with the associated Mg peak results in a percentage of 74% MgO due to the natural oxide layer compared to 26% elemental Mg. Compared to the reference sample, the percentage of MgO in the anodes contacted with the solvent is between 74% and 86%. This shows that even after intensive surface scraping, an oxide layer is still present on the Mg surface. Solvents might increase the oxide surface coverage. The exact percentages for all MgO and Mg peak areas are summarized in Table 4.2.

Table 4.2: Percentage of the Mg and MgO peak areas in the Mg 2p spectra.

	DME	**THF**	**DMAc**	**DMF**	**PC**	**DEC**	**Mg (reference)**
Mg ratio / %	26	14	15	23	23	22	26
MgO ratio / %	74	86	85	77	77	78	74

4.2 Morphology of the modified anode surfaces

The surface morphology of the coatings prepared on Mg via spin coating were examined by means of SEM before and after galvanostatic cycling (> 150 cycles). Figure 4.2 depicts the comparison of the surface morphology of the spin coated Mg anodes using s-PSO2-220/PVDF, Aquivion/PVDF, Nafion/PVDF SPEEK/PVDF, and PAN before galvanostatic cycling. The associated EDX analysis is attached (Figure A1).

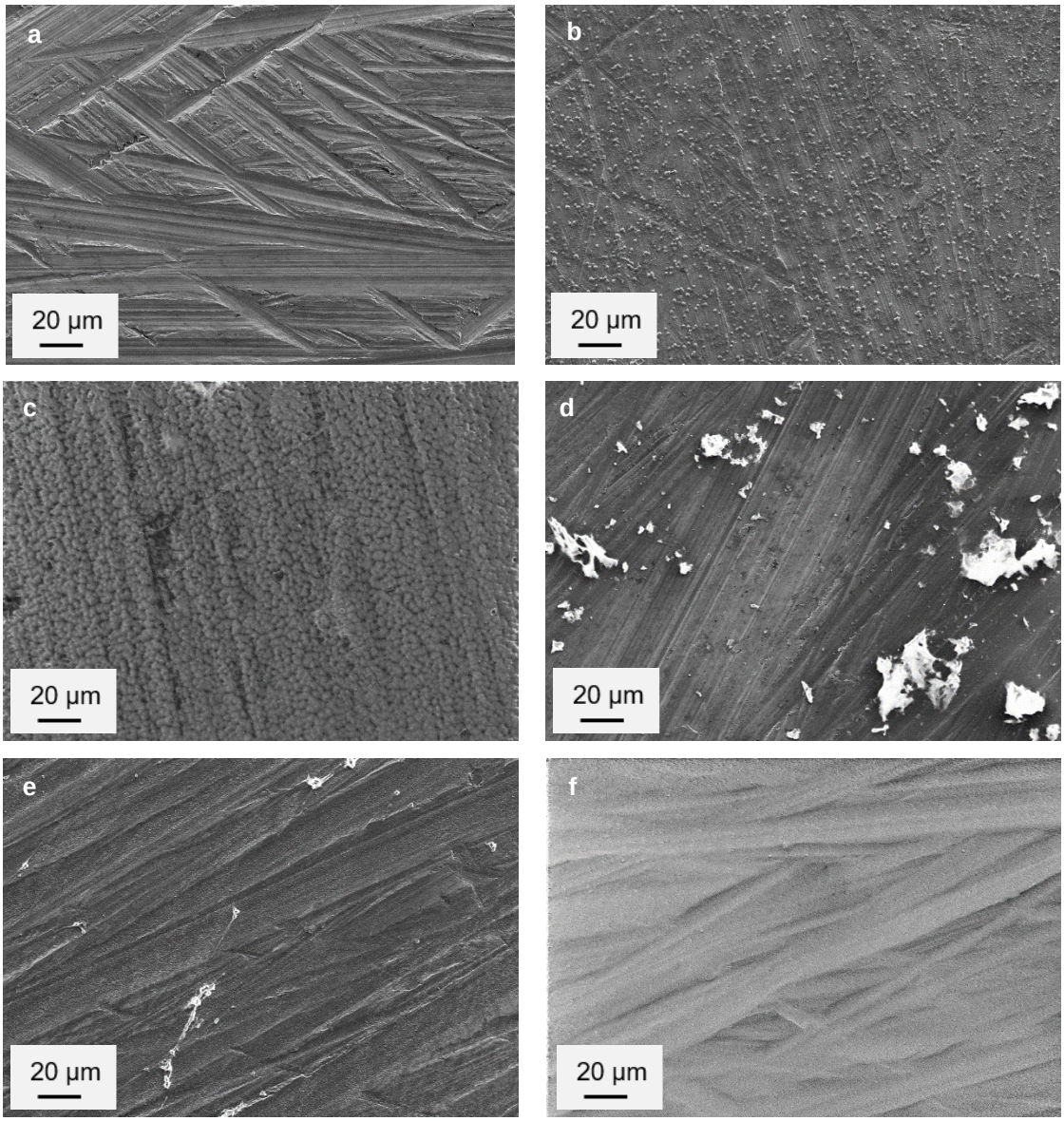

Figure 4.2: Surface morphology of (a) the pristine Mg anode, (b) Mg-s-PSO2-220/PVDF, (c) Mg-Aquivion/PVDF, (d) Mg-Nafion/PVDF, (e) Mg-SPEEK/PVDF and (f) Mg-PAN.

The pristine Mg anode (a) has a flat surface with visible scratches that originate from the removal of the native oxide layer using a glass object slide or spatula (Chapter 3.3). In comparison, the Mg-s-PSO2-220/PVDF anode only has slight scratches due to the coating. In addition, finely distributed grains on the surface are assigned to coating components using EDX analysis. Apart from that, the only slightly reduced mass fraction of Mg compared to the reference indicates a very thin coating of the Mg surface. The SEM image of the Mg-Aquivion/PVDF anode (c) clearly shows a completely covered surface with spherical granules with a diameter of a few micrometers. The complete coating of the Mg surface is confirmed by the EDX analysis. In contrast in the SEM images of the Mg-Nafion/PVDF anode (d) and Mg-SPEEK/PVDF anode (e) the surface structure of the pristine Mg anode is still recognizable. The EDX analysis shows a lower Mg content compared to the reference, which indicates a thin coating of the surface. However, light spots appearing at certain points showing an inhomogeneous coating. Mg-PAN anodes (f) have a denser and smoother surface. The Mg salt used for the PAN coating gives the coating a light grayish tint. The complete coating of the surface can therefore be optically analyzed without magnification.

The change in the surface morphology of the anodes during cycling was reviewed *post-mortem*. Figure 4.3 compares the uncoated anode (a) and the coated anodes (b-f) after > 150 galvanostatic cycles at C/10.

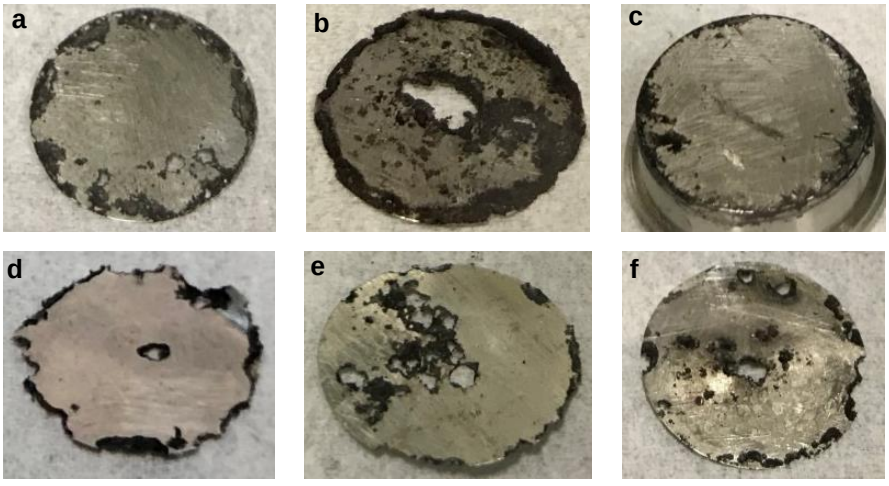

Figure 4.3: *Post-mortem* images of (a) the uncoated Mg anode as well as (b) Mg-s-PSO2-220/PVDF, (c) Mg-Aquivion/PVDF, (d) Mg-Nafion/PVDF, (e) Mg-SPEEK/PVDF and (f) Mg-PAN.

Figure 4.4 shows the corresponding SEM images. The respective EDX analyzes as well as further *post-mortem* SEM images of the Mg-Aquivion/PVDF anode at different magnifications are given in the appendix (Figure A2 and Figure A3).

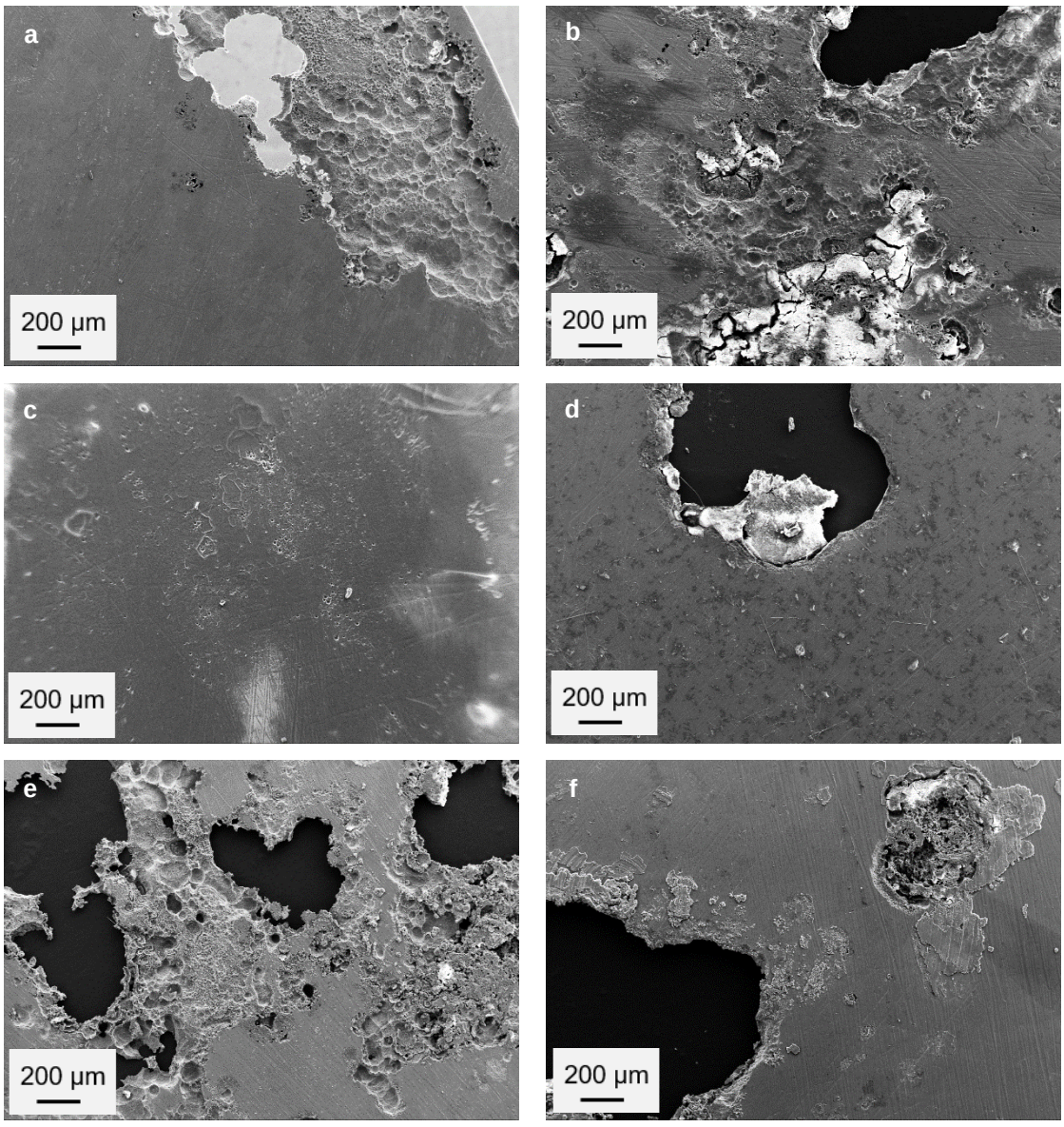

Figure 4.4: Surface morphologies of (a) the Mg anode, (b) Mg-s-PSO2-220/PVDF, (c) Mg-Aquivion/PVDF, (d) Mg-Nafion/PVDF, (e) Mg-SPEEK/PVDF and (f) Mg-PAN after > 150 galvanostatic cycles at C/10 in a Mg-S cell.

The aging of the uncoated Mg anode during cycling (Figure 4.3 a) mainly took place at the edge, which is shown by an increasing porosity up to the formation of holes at the edge of the

anode (Figure 4.4 a). This is also observed to a lesser extent with the Mg-Aquivion/PVDF anode (Figure 4.3 and 4.4 c). The SEM image shows the formation of bubbles, which are attributed to the localized cracking of the layer. However, the EDX analysis proves a low Mg content overall and confirms the durability of the coating. In the case of the s-PSO2-220 coating (Figures 4.3 and 4.4 b) a central hole has formed in the anode. Nevertheless, the previously observed increased aging of the anodes at the edge also occurs. This fading is particularly emphasized with the Mg-Nafion/PVDF anode (Figure 4.3 and 4.4 d). The surfaces of the Mg-SPEEK/PVDF anode and Mg-PAN anode (Figure 4.3 and 4.4 e-f) have several small holes. Especially the entire surface of the SPEEK/PVDF coating is already heavily roughened and the coating is no longer present (EDX).

4.3 Galvanostatic cycling of Mg-S cells

The cycling behavior of the coated Mg anodes during galvanostatic cycling was first investigated in Mg-S cells. Active materials of the coatings were the hydrocarbon-based ionomers s-PSO2-220 and SPEEK, as well as the perfluorinated ionomers Aquivion and Nafion. Based on the publication by Son *et al.*, thermal-cyclized PAN was additionally applied as a coating component.[9] For better Mg^{2+} conductivity, the conductive salt Mg trifluoromethanesulfonate was added to the PAN coating.

4.3.1 Properties of s-PSO2-220, SPEEK, Aquivion and Nafion

Ionomers are single ion conductors, which means that only one type of ion (anion or cation) participates at the electrochemical process. In comparison to the classic polymer electrolyte, there is therefore no unnecessary accumulation of inactive ions on the *in-situ* SEI. The used ionomers generally have good ionic conductivities in the range of 10^{-4} $S \cdot cm^{-1}$ due to the polar sulfonic acid groups at the ends of the side chains (Figure 3.1).[8] Furthermore, the polar groups result in high acidity and high cation transference numbers. The ionomers, however, differ in terms of their ion exchange capacity.[81,82] This is primarily due to the different structure of the repetition unit of the polymer backbone. A larger number of functional sulfonic acid groups results in a higher polarity and the sum of the exchangeable ions increases. The following order of priority applies to the ionomers used: $IEC_{s\text{-}PSO2\text{-}220} > IEC_{SPEEK} > IEC_{Aquivion} \geq IEC_{Nafion}$. It must be noticed, that the exact values of the IEC depends on the degree of sulfonation of the respective ionomer and thus varies depending on the manufacturer. The ion exchange capacities of the ionomers used for the coatings are listed in Table 4.3.

Table 4.3: IEC of the ionomers used for the coatings.

Ionomer	Ion exchange capacity / $\mathbf{meq \cdot g^{-1}}$
s-PSO2-220	4.55
SPEEK	2.7
Aquivion	1.3
Nafion	0.9

4.3.2 *In-situ* proton exchange

The successful *in-situ* exchange of the protons (H^+) of the sulfonic acid group of the ionomers s-PSO2-220, Aquivion, Nafion and SPEEK with Mg^{2+} ions during galvanostatic cycling in Mg-S cells was confirmed by FTIR spectroscopy. In Figure 4.5 an exemplary FTIR spectrum of Aquivion (H^+ powder form) before cycling and the FTIR spectrum of the Mg-Aquivion/PVDF anode, which was recorded *post-mortem* is shown.

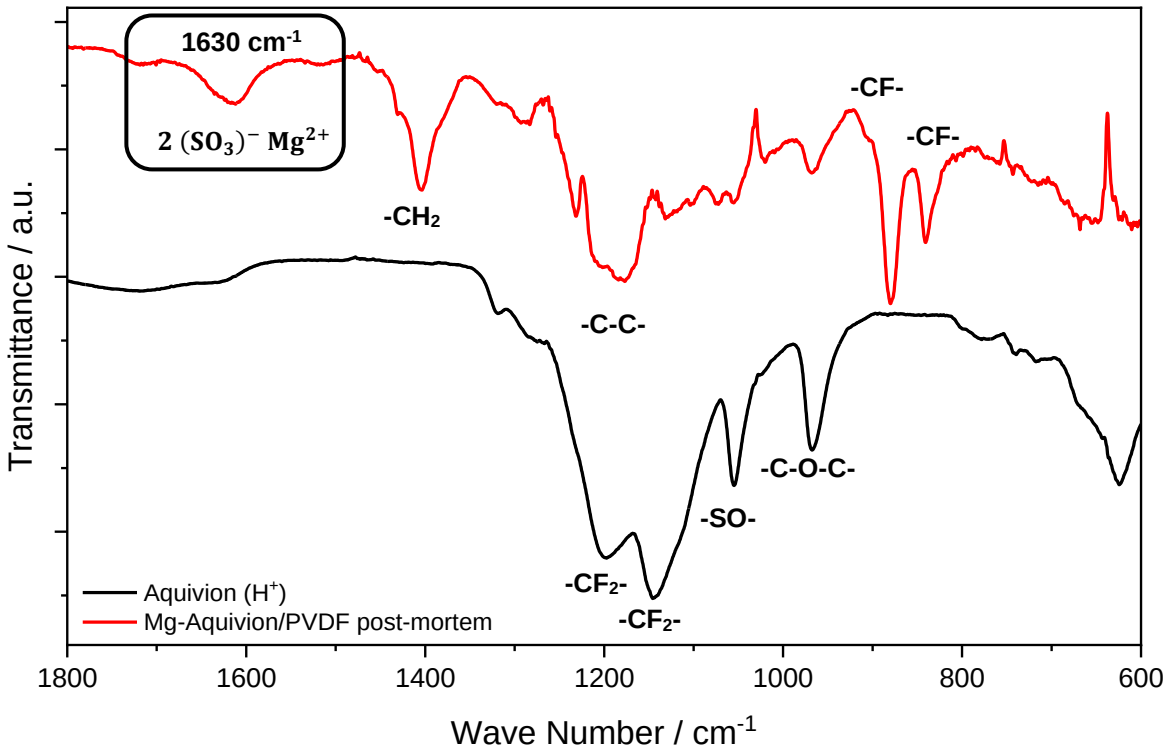

Figure 4.5: FTIR spectra of Aquivion (H^+) before cycling and the corresponding Mg-Aquivion/PVDF anode (*post-mortem*) over the range of 600 – 1800 cm^{-1}.

The conversion from the H^+ form to the Mg^{2+} form was verified by the appearance of the 1630 cm^{-1} band in the *post-mortem* spectrum of the Mg-Aquivion/PVDF anode and is comparable to the Li^+ proton exchange.[83] An additional intense band at 1403 cm^{-1} corresponds to a CH_2 wagging vibration of PVDF.[84] The characteristic bands of the Aquivion H^+ form in the fingerprint range < 1300 cm^{-1} are attributed to the asymmetrical and symmetrical stretching vibration of -CF_2- (1200 cm^{-1}, 1148 cm^{-1}), the symmetrical stretching vibration of -SO- (1055 cm^{-1}) and the symmetrical stretching vibration of -C-O-C- (970 cm^{-1}). In the *post-mortem*

sample, these bands partly overlap with the bands of PVDF. The spectrum of the Mg-Aquivion/PVDF anode shows the characteristic band of the -C-C vibration at a wave number of 1185 cm^{-1} as well as the symmetrical and asymmetrical -CF- stretching vibration (887 cm^{-1}, 840 cm^{-1}).[85] A comparison of the *post-mortem* recorded spectrum of a chemically similar Mg-Nafion/PVDF anode with the corresponding reference sample shows an identical result (Figure A4). In the spectrum of the Mg-SPEEK/PVDF anode the intensity of the characteristic broad band of the -OH stretching vibration decreases significantly due to the reduced OH groups compared to the SPEEK reference spectrum (Figure A5). The *in-situ* exchange of H^+ to Mg^{2+} is also confirmed by the appearance of the band at 1200 cm^{-1}, which is assigned to an asymmetrical Mg-O-Mg stretching vibration.[86] Moreover, an additional characteristic band (-C-C-, 1160 cm^{-1}) occurs due to PVDF. The break-up of the SEI during cycling resulting in no detectable Mg-s-PSO2-220/PVDF coating. Thus, no intense bands are shown in the *post-mortem* recorded spectrum (Figure A6).

4.3.3 Influence of coated Mg anodes on cycling behavior

The influence of the artificial SEI on the cycling behavior of Mg-S cells is shown in comparison to a Mg reference cell without a coating. Figure 4.6 shows the specific discharge capacity of Mg-S cells consisting of Mg anodes with and without artificial SEI at C/10. Ball milled S/KB cathodes with a sulfur content of $1.0\,mg \cdot cm^{-2}$, two GF/C separators and a 0.2 M $Mg[B(hfip)_4]_2$ DME electrolyte were used.

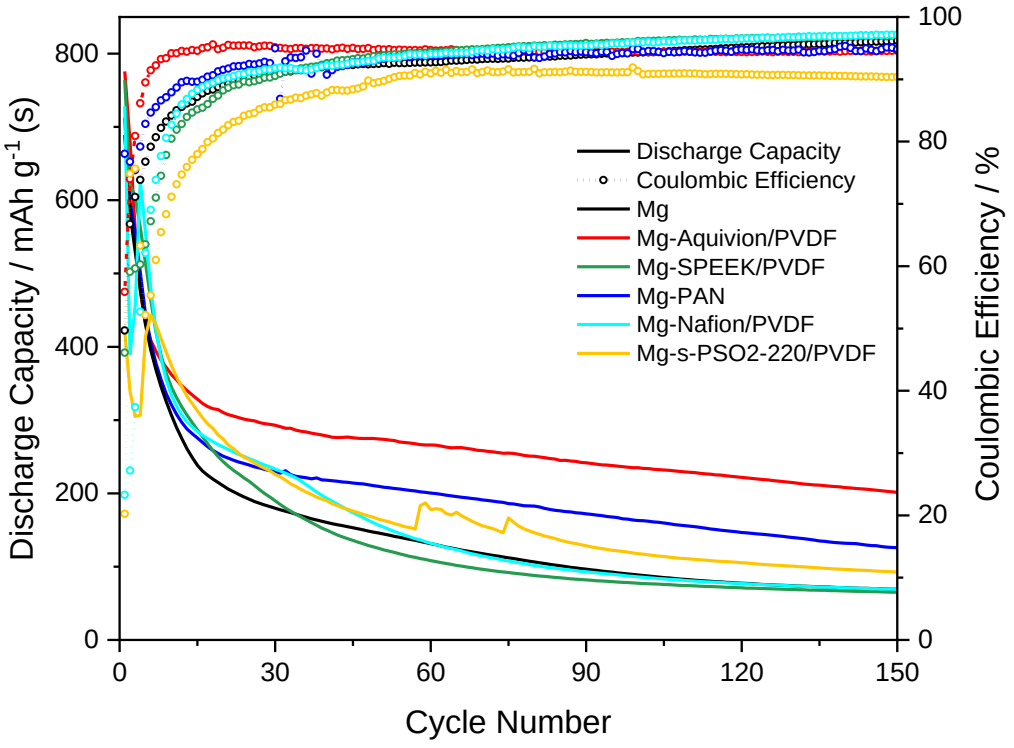

Figure 4.6: Cycling performance of Mg-S cells with different artificial SEI at C/10 (electrolyte: 0.2 M $Mg[B(hfip)_4]_2$ DME, separator: GF/C, cathode: S/KB ball milled, sulfur loading: 1.0 $mg \cdot cm^{-2}$).

As shown in Figure 4.6 Mg-Aquivion/PVDF anodes demonstrate a good long-term performance. However, similar to the uncoated Mg reference sample a loss of capacity is observed in the first ten cycles. In the initial cycles, the discharge capacity of the Mg-Aquivion/PVDF anode is higher than that of the uncoated Mg reference, since no polysulfides react with Mg metal due to the already present artificial SEI. The formation of the *in-situ* SEI on the uncoated anode results in an equalization of the discharge capacities of the uncoated and coated anode between cycle three and cycle six. The subsequent loss of capacity, which is mainly caused by the polysulfide shuttle and the associated loss of the active material, is lower with the Mg-Aquivion/PVDF anode. This results in a constant capacity offset of around 130 $mAh \cdot g^{-1}$ and a discharge capacity of 202 $mAh \cdot g^{-1}$ compared to 69 $mAh \cdot g^{-1}$ for the uncoated Mg reference after 150 cycles, which equals a capacity gain of almost 200%. The coulombic efficiency of the Mg-Aquivion/PVDF anode reaches a constant value of around 95% after ten cycles, suggesting that the system is stable. With the uncoated anode a constant value of 95% is only reached after about 40 cycles.

Using a Mg-PAN anode an 85% higher discharge capacity was achieved compared to the Mg reference after 150 cycles. However, due to the lower conductivity of the PAN polymer compared to the Aquivion ionomer, the discharge capacities are constantly lower than those of the Mg-Aquivion/PVDF anode. Coulombic efficiency is initially between that of the Mg-Aquivion/PVDF anode and the Mg reference, before a constant value of around 95% is also reached after 40 cycles.

The Mg-s-PSO2-220/PVDF anode shows the best performance in capacity retention of all coatings. The initial capacity, however, is well below the values of the other coatings. It is noticeable that the discharge capacity decreases in the first three cycles and then increases again up to the sixth cycle. Therefore, it is assumed that due to an inhomogeneous coating some in *in-situ* SEI components are deposited on the anode and cause the change in capacity. The comparatively lowest coulombic efficiency suggests a more unstable system. Nevertheless, the discharge capacity after 150 cycles is 33% higher than that of the Mg reference.

Decrease and the subsequent increase in the discharge capacity at the initial cycles is also observed with the Mg-Nafion/PVDF anode. An improved cycle stability compared to the Mg reference sample is shown during the first 60 cycles. From the 60th cycle onwards the capacity in comparison to the uncoated anode is almost the same. Due to the similar chemical structure of Nafion and Aquivion, comparable cycling behavior was expected. Contrary to the expectations, low discharge capacities of the Mg-Nafion/PVDF anode indicate an inhomogeneous inadequate coating of the anode.

The artificial SPEEK/PVDF coating results in the highest initial capacity ($764\ \mathrm{mAh \cdot g^{-1}}$) of all cells. However, there is a rapid loss of capacity. After 30 cycles the discharge capacity is lower than that of the Mg reference. This suggests a break-up of the coating due to a small thickness or an inhomogeneous coating and confirms the observations made using SEM-EDX.

Complementary to the previously characterization of the different coated anodes a comparison of the initial discharge/charge cycles 1, 3, 5 and 20 is illustrated in Figure 4.7.

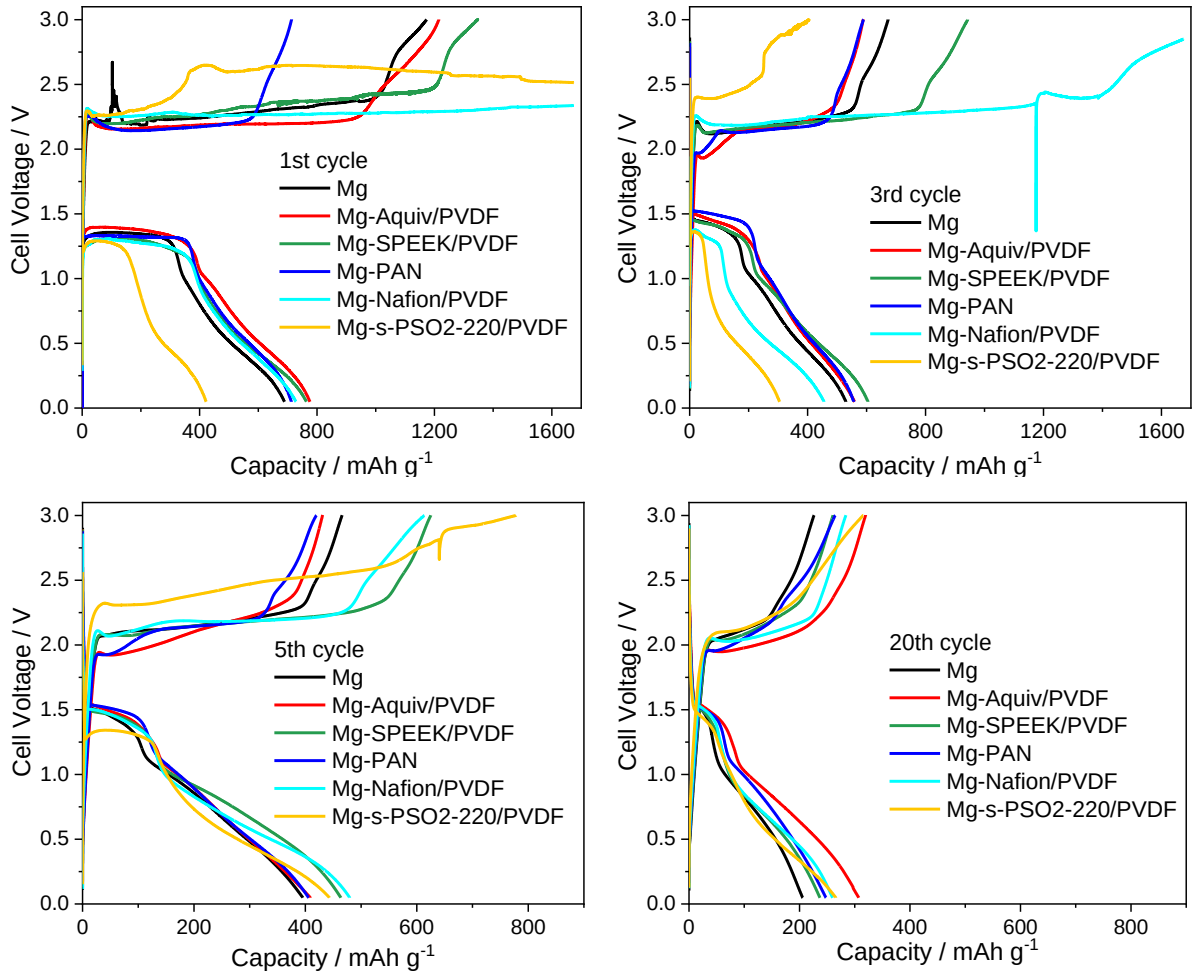

Figure 4.7: Comparison of the initial discharge/charge cycles 1, 3, 5 and 20 of Mg-S cells with different artificial SEI at C/10 (electrolyte: 0.2 M $Mg[B(hfip)_4]_2$ DME, separator: GF/C, cathode: S/KB ball milled, sulfur loading: 1.0 $mg \cdot cm^{-2}$).

In the first three cycles, there is no clear trend towards higher capacities of SEI-coated anodes compared to uncoated anodes, whereas from the 5th cycle onwards the discharge capacities with artificial SEI are increased. Cells with Nafion/PVDF or s-PSO2-220/PVDF SEI show an inconstant charging behavior in the initial cycles. However, in the 20 cycle, all cells with a coated anode show higher charge and discharge capacities than the uncoated reference.

4.3.4 Variation of the coating thickness

The influence of the thickness of the artificial SEI on the cycling performance in Mg-S cells was investigated using various Aquivion/PVDF coatings. For this purpose, Mg anodes were

coated once, twice, three and five times by means of spin coating. In addition, these artificial SEI were compared with a dip coated Aquivion/PVDF SEI. Figure 4.8 shows the specific discharge capacities at C/10 in Mg-S cells consisting of Mg anodes with Aquivion/PVDF coatings with various layer thicknesses.

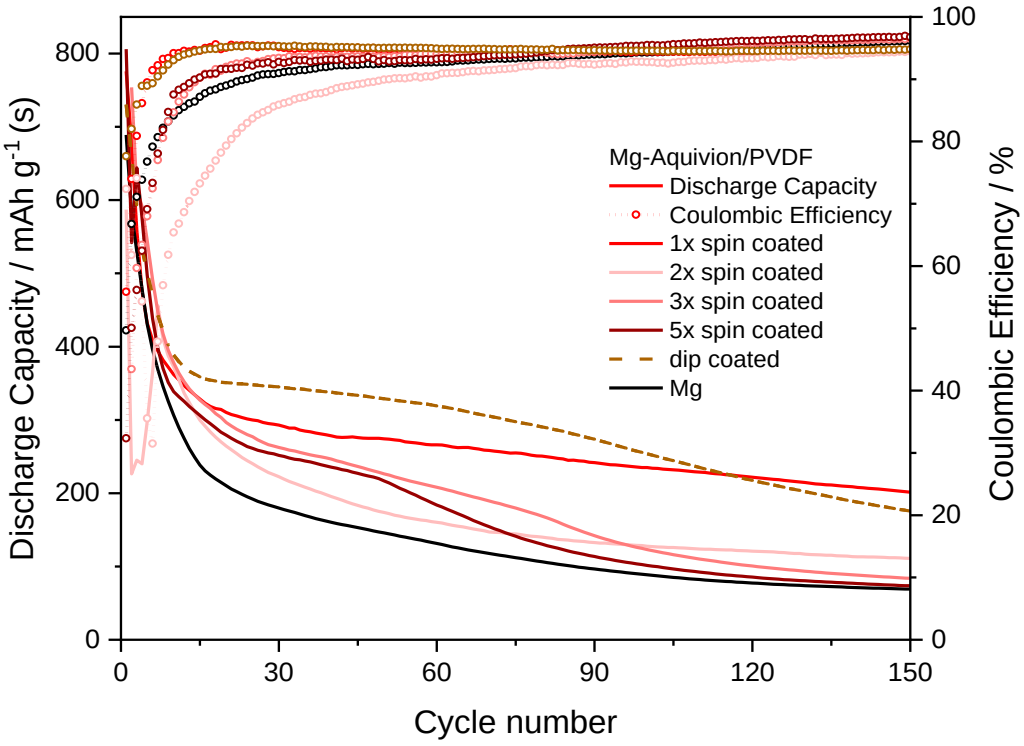

Figure 4.8: Influence of coating thickness on the cycling performance of Mg-S cells with artificial Aquivion-PVDF-SEI at C/10 (electrolyte: 0.2 M $Mg[B(hfip)_4]_2$ DME, separator: GF/C, cathode: S/KB ball milled, sulfur loading: 1.0 mg · cm^{-2}).

There are significant differences in terms of capacity retention with various thicknesses of the anode coatings (Figure 4.8). Three times and five times coated anodes lead to a sudden loss of capacity after 90 and 50 cycles, respectively. Due to the multiple coating, artificial SEI result in locally thicker and thinner areas. Thin areas with lower resistance can trigger a localized Mg deposition, which explains the sudden loss of capacity.[62] In comparison, anodes that have been coated only once or twice show better cycle stability. However, it must be noted that the double-coated anode initially has a lower capacity than the three times or five times coated anode. This suggests that initially with thicker coatings the polysulfide repelling character predominates

until the layer breaks up locally. As expected, the thinnest layer has the most constant cycling performance due to the best ion conductivity and more homogeneous Mg deposition. The artificial SEI produced by means of dip coating leads to advantages in terms of the discharge capacity during the first 60 cycles compared to the coatings produced by means of spin coating. Similar to the three times and five times spin coated anodes a faster loss of capacity is shown in the following cycles.

4.3.5 Influence of PVDF on coating stability

The influence of the PVDF binder as a coating component is explained below. For this purpose, simple ionomer coatings were compared with ionomer/PVDF coatings in Mg-S cells. Figure 4.9 illustrates the specific discharge capacities of the Mg-S cells at C/10.

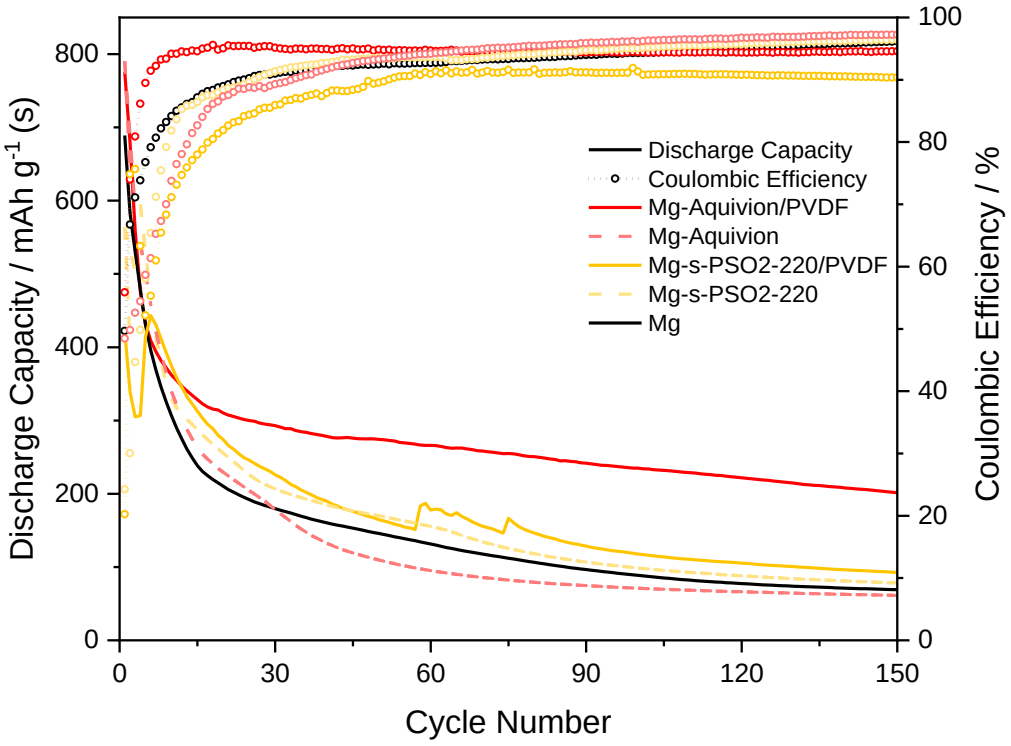

Figure 4.9: Influence of PVDF on the cycling performance of Mg-S cells with artificial SEI at C/10 (electrolyte: 0.2 M $Mg[B(hfip)_4]_2$ DME, separator: GF/C, cathode: S/KB ball milled, sulfur loading: 1.0 $mg \cdot cm^{-2}$).

The addition of PVDF binder as coating component results in an improved cycling performance in Mg-S cells due to a more stable artificial SEI. The binder fixes the ionomers on the surface and prevents the SEI from dissolving.[7,8] Ionomers can swell on the surface without breaking the SEI. In particular, the Aquivion/PVDF SEI shows a significantly better capacity retention of the Mg-S cell than the pure Aquivion coating.

4.4 Electrochemical impedance spectroscopy of symmetrical Mg-Mg cells

In addition to the cycling performance in Mg-S full cells, the electrochemical characterization of the artificial SEI was carried out in symmetrical Mg-Mg cells.

4.4.1 Overpotentials during Mg stripping/plating

First, the electroplating behavior of a cell with artificial Aquivion/PVDF SEI and a cell with an uncoated Mg anode was compared. Figure 4.10 shows the reversible stripping and plating in both cells at 0.1 and 1.0 mA · cm^{-2}.

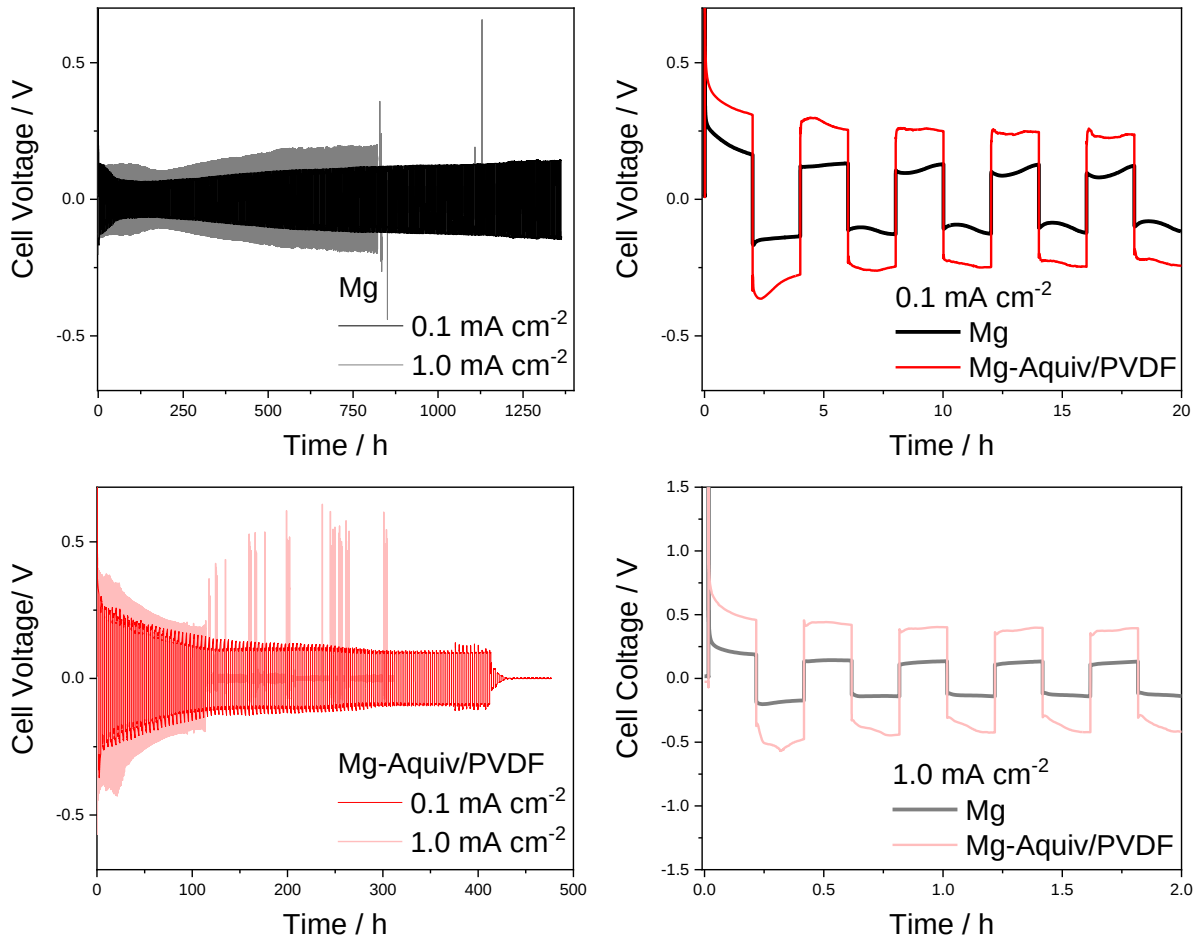

Figure 4.10: Potential profiles of symmetrical Mg-Mg cells without artificial SEI and Mg-Mg cells with artificial Aquivion/PVDF SEI at 0.1 and 1.0 mA · cm^{-2}.

The overserved overpotentials are mainly caused by mass transport processes such as solvation or SEI diffusion. The latest findings from Eaves-Rathert *et al.* also show, that the current density relates to the deposition morphology of Mg and a distinction must be made between kinetic and diffusive limitation. The latter promote the growth of 3D Mg deposits on the Mg anode, which can lead to mossy dendrites.[23] As shown in Figure 4.10 cells with Aquivion/PVDF coated anodes exhibited higher overpotentials than the uncoated cells at the respective currents of $0.1\ \mathrm{mA \cdot cm^{-2}}$ and $1.0\ \mathrm{mA \cdot cm^{-2}}$. In cells with an uncoated anode a decrease in the overpotential up to a certain voltage is observed initially. Freshly deposited magnesium increases the surface area, which in turn increases the resistance. In the further course, the overpotentials increase with increasing polarization time. Compared to cells with an uncoated anode, both the low current density of $0.1\ \mathrm{mA \cdot cm^{-2}}$ and the higher current density of $1.0\ \mathrm{mA \cdot cm^{-2}}$ lead to faster cell failure of artificial SEI coated cells.

In the following a Mg reference electrode was used to distinguish between stripping and plating. The positive potentials of the Mg appear during Mg stripping, whereas the negative potentials represent the overpotentials during Mg plating on the anode. As illustrated in Figure 4.11, the cells were alternately kept in a resting phase for a defined time period and then polarized for ten cycles at 0.1, 0.2, 0.5, 1.0 and again $0.1\ \mathrm{mA \cdot cm^{-2}}$.

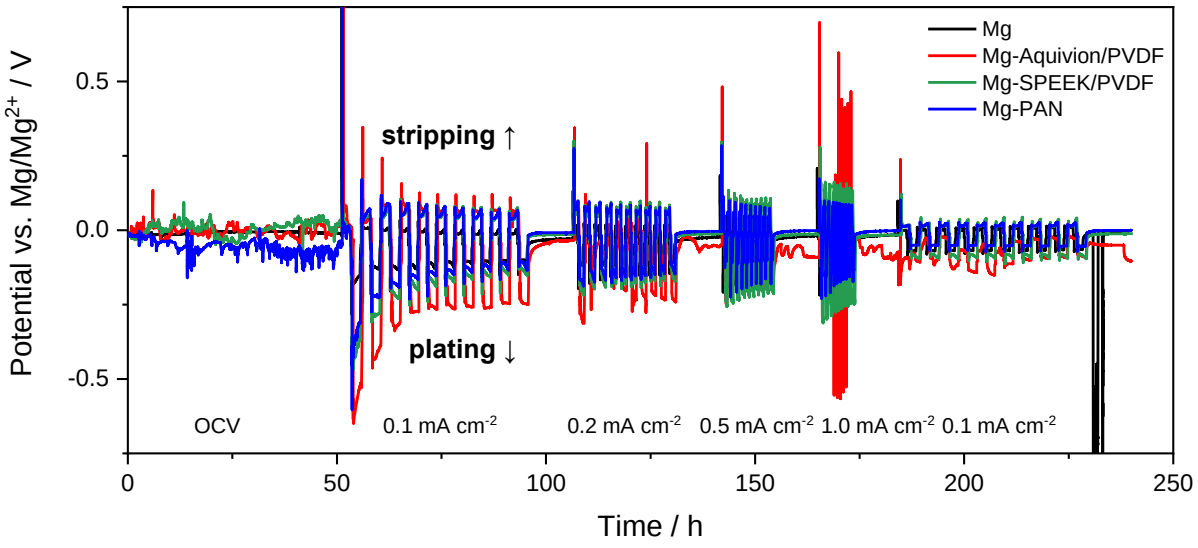

Figure 4.11: Potential profiles of Mg-Mg cells with artificial Aquivion/PVDF, SPEEK/PVDF and PAN SEI as well as the potential profile of a Mg-Mg cell without artificial SEI during OCV and polarization at different current densities.

As already described before, the anode coatings lead to higher overpotentials. A discontinuous potential can be observed during the OCV phases. In addition, significantly higher overpotentials are generated in plating than in stripping. Aquivion/PVDF anodes show the highest overpotential. Figure 4.12 shows an enlarged representation of the polarization cycle at 0.1 mA · cm^{-2}.

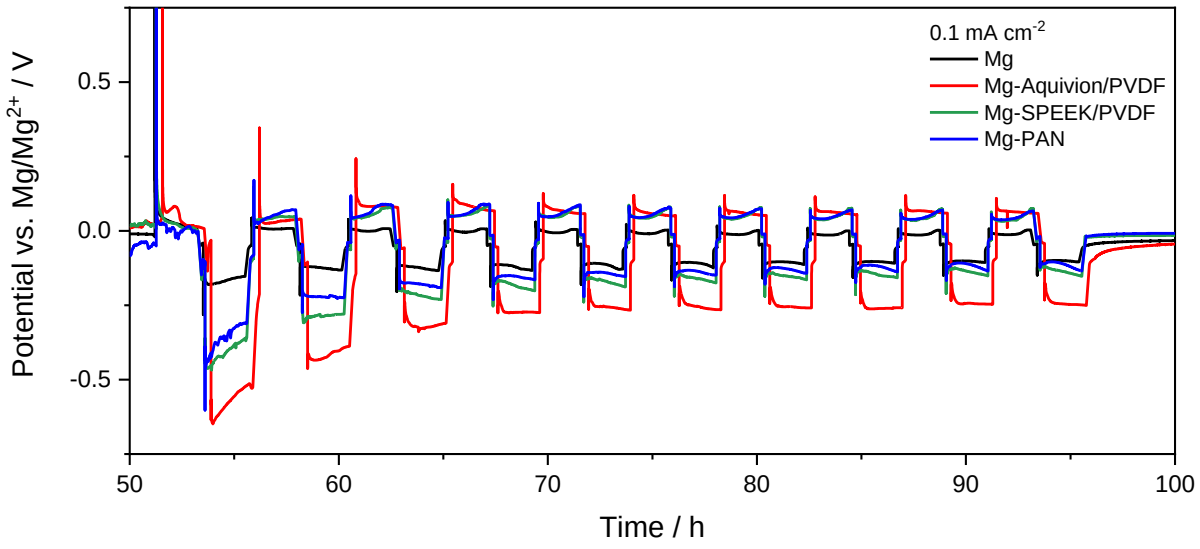

Figure 4.12: Potential profiles of Mg-Mg cells with artificial Aquivion/PVDF, SPEEK/PVDF and PAN SEI as well as the potential profile of a Mg-Mg cell without artificial SEI at 0.1 mA · cm^{-2}.

The enlargement clearly shows the higher overpotentials during plating. It is assumed that this is mainly due to the desolvation. Low overpotentials of the cell with an uncoated anode probably result from the smaller thickness of the *in-situ* formed SEI compared to the artificial SEI.[87] To get more insights about the processes occurring at the interface between anode and electrolyte, pseudo-galvanostatic EIS measurements were carried out.

4.4.2 Process assignment in anode impedance spectra

In the following, the differences between an uncoated Mg anode and an anode protected with artificial Aquivion/PVDF SEI during OCV are considered. Figure 4.13 compares the respective Bode plots. In addition, Bode plots of the cells at OCV after polarization at 0.2 mA · cm^{-2} and 1.0 mA · cm^{-2} are given in the appendix (Figure A7 and Figure A8).

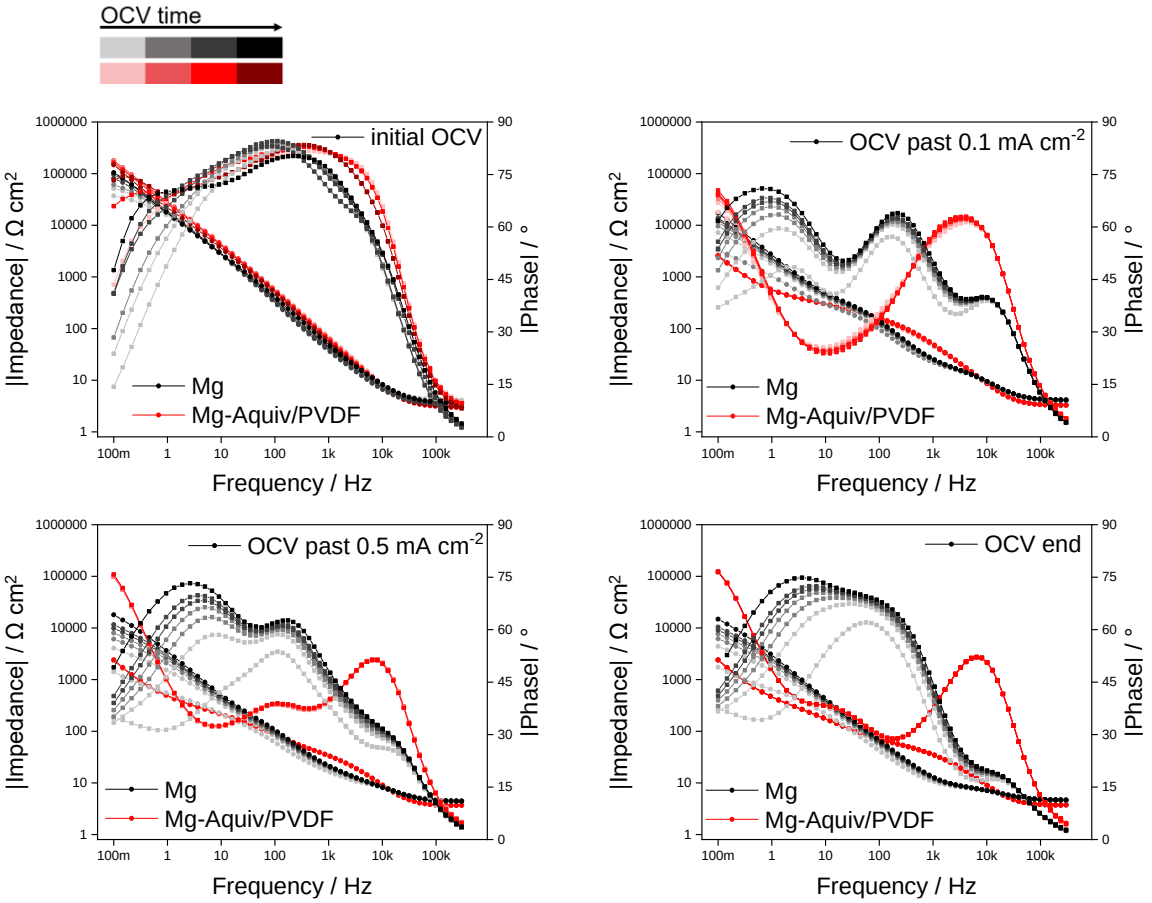

Figure 4.13: Bode plots of Mg-Mg cells without artificial SEI (black) and with Aquivion/PVDF SEI (red) during 50 h OCV (start) and after ten galvanostatic cycles at 0.1, 0.5 and concluding 0.1 mA · cm^{-2}.

Figure 4.13 shows overlapping processes in the initial resting phase. After the first polarization at 0.1 mA · cm^{-2} three overall processes are distinguishable. A constant process in the high-frequency (HF) region (~ 10^4 Hz), a process in the middle-frequency (MF) region and a process in the low-frequency (LF) region. With an Aquivion/PVDF coated anode the MF process only builds up over time – as illustrated in the Bode plot of the OCV after polarization at

$0.5\ \mathrm{mA}\cdot\mathrm{cm}^{-2}$. Since the assignment of the HF and MF process to particular processes at the Mg electrolyte interface is complex a comparison of the two cells during polarization at different current densities is needed. In contrast, the ohmic resistance is well-defined at a phase angle of zero degree in the HF region and can be assigned to the electrolyte resistance, i.e. its ionic conductivity. In addition, the process in the low frequency (LF) region correlates with the formation of an adsorption layer through electrolyte species. The adsorption layer is removed during the polarization of the cell and typically forms again during OCV.[88] In the case of the Aquivion/PVDF coated anode this process is significantly slower compared to the uncoated Mg anode due to the hindered bidirectional diffusion of Mg^{2+}. As a result, the LF process shifts to a lower frequency area. It must be noted that the adsorption process does not build up further after polarization at $0.1\ \mathrm{mA}\cdot\mathrm{cm}^{-2}$. A probable reason are the similar time constants for the adsorption and the diffusion through the artificial SEI, which causes an overlay of the impedance response in the LF region.

In order to investigate this more closely, the development of the processes in the Mg-Mg cell with uncoated Mg anodes and the Mg-Mg cell with Aquivion/PVDF SEI during polarization was considered. The comparison of the Bode representations of the two cells during polarization at different current densities is given in Figure 4.14 (stripping) and Figure 4.15 (plating). Bode plots of stripping and plating of the cells at $0.5\ \mathrm{mA}\cdot\mathrm{cm}^{-2}$ are attached (Figure A7 and Figure A8).

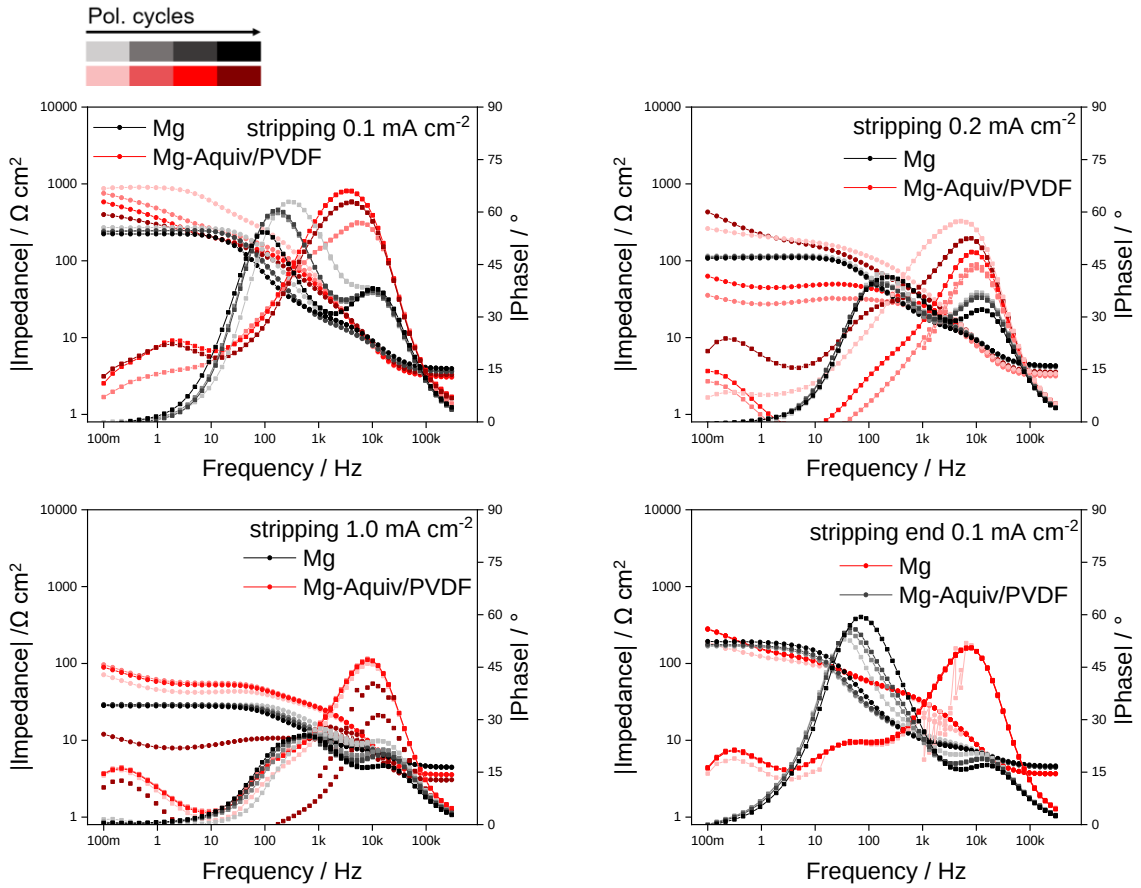

Figure 4.14: Bode plots of the stripping process of Mg-Mg cells without artificial SEI (black) and with Aquivion/PVDF SEI (red) at 0.1, 0.2, 1.0 and concluding 0.1 $mA \cdot cm^{-2}$.

During stripping (Figure 4.14) and plating (Figure 4.15), a current-rate-dependent formation of the MF process is shown. Another important difference between the two cells can be observed in the LF region. The coating of the anode with an artificial SEI causes an additional process, which with the exception of the plating at 0.1 and 0.2 $mA \cdot cm^{-2}$ cannot be seen in cells with uncoated Mg anodes (Figure 4.15). This confirms the observations during OCV and is a further indication that the processes of adsorption and artificial SEI exhibit similar time constants.

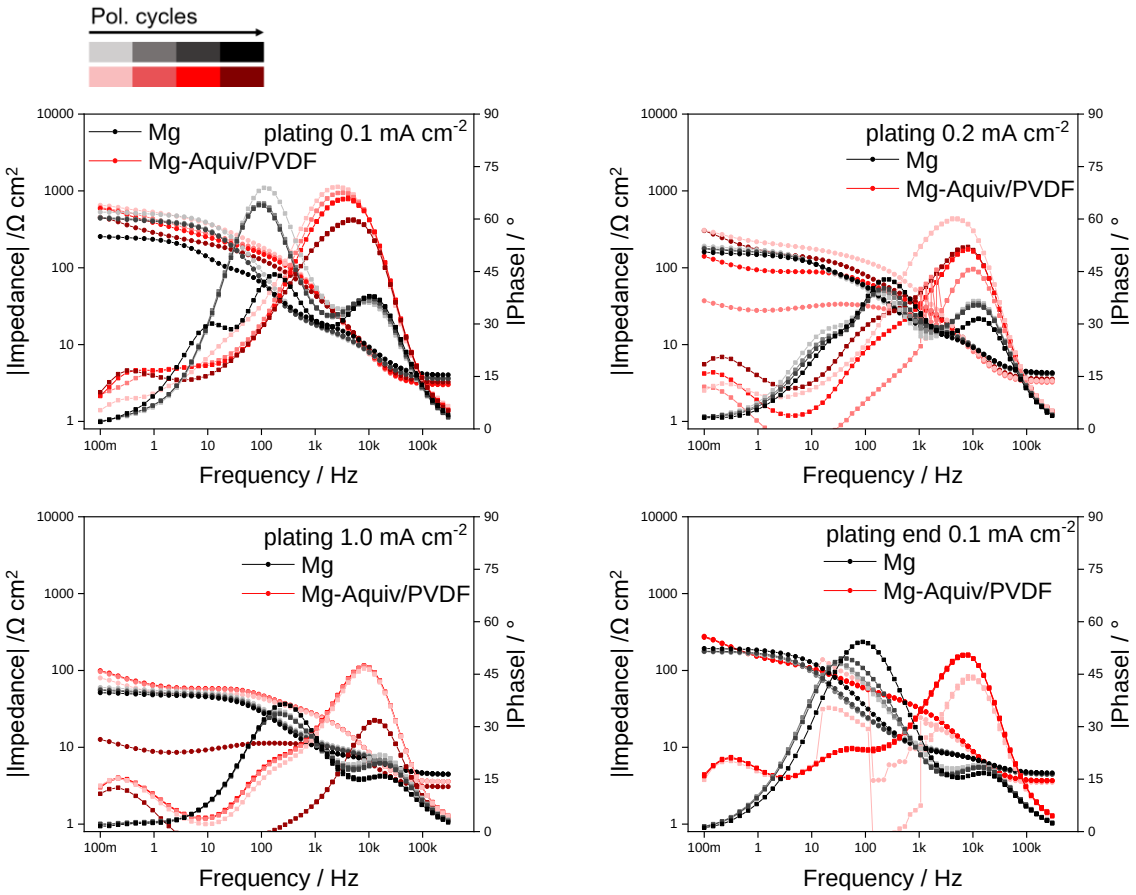

Figure 4.15: Bode plots of the plating process of Mg-Mg cells without artificial SEI (black) and with Aquivion/PVDF SEI (red) at 0.1, 0.2, 1.0 and concluding 0.1 $mA \cdot cm^{-2}$.

It is assumed that this is due to the artificial SEI, what is supported by the only slight change in the process during the polarization phase. In addition, the current density and test-duration-dependent formation of the MF process in the case of cells with Mg-Aquivion/PVDF anodes promote the assignment of the LF process to the artificial SEI. SEM analyses have shown that the artificial SEI partially breaks up over time, which allows an *in-situ* SEI to be formed on the locally unprotected Mg anode. Therefore, the MF process relates to the *in-situ* formed SEI. As shown in Figures 4.14 and 4.15, the frequency ranges of the MF processes of the uncoated anode and the artificial Aquivion/PVDF SEI are in good agreement. This confirms the observations during the resting phase, in which the MF process is also recognizable. Since Mg is highly reductive, SEI formation through electrolyte decomposition even takes place without applying a current.[51,88] Furthermore, XPS analysis (Chapter 4.1) has shown that the bare contact of the solvent is sufficient to generate a migration barrier on the Mg anode.

The process with the fastest kinetics (HF process) is assigned to the charge transfer (CT). This is backed by the constant position of the process during the OCV and polarization phases between 10 kHz and 12 kHz.

4.4.3 Resistance evolution during polarization

When interpreting the Bode plots of pristine and Aquivion/PVDF-coated Mg anodes, two and three overall processes during the polarization are assumed for the creation of the ECM, respectively. These processes can be represented by RC elements connected in series in an ECM. Instead of ideal capacitors, constant phase elements (CPE) were used to account for surface roughness and inhomogeneities. Figure 4.16 shows the proposed models for the simplified description of the processes at the anode/electrolyte interface in a symmetrical Mg-Mg cell (a) without artificial SEI and (b) with artificial SEI. It must be noted that the proposed model is only valid with an intact artificial SEI. Normally, most coatings degrade with time, resulting in a more complex behavior.[89]

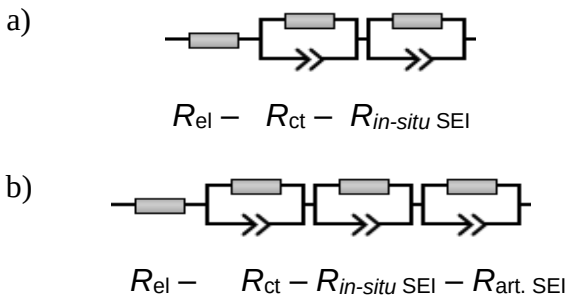

Figure 4.16: ECM used for fitting of impedance data a) Mg and b) Mg-Aquivion/PVDF.

The Bode plots of the Mg-Mg cell with uncoated anode were fitted according to model a), comprising the ohmic resistance R_{el} as well as R_{ct} and $R_{in\text{-}situ\ SEI}$, both in parallel with a CPE. Model b) was used for the cell with artificial Aquivion/PVDF SEI and contains another R-CPE element that represents the artificial SEI.

Figure 4.17 illustrates the development of the individual resistances during polarization at 0.1, 0.2, 0.5, 1.0 and concluding 0.1 $mA \cdot cm^{-2}$.

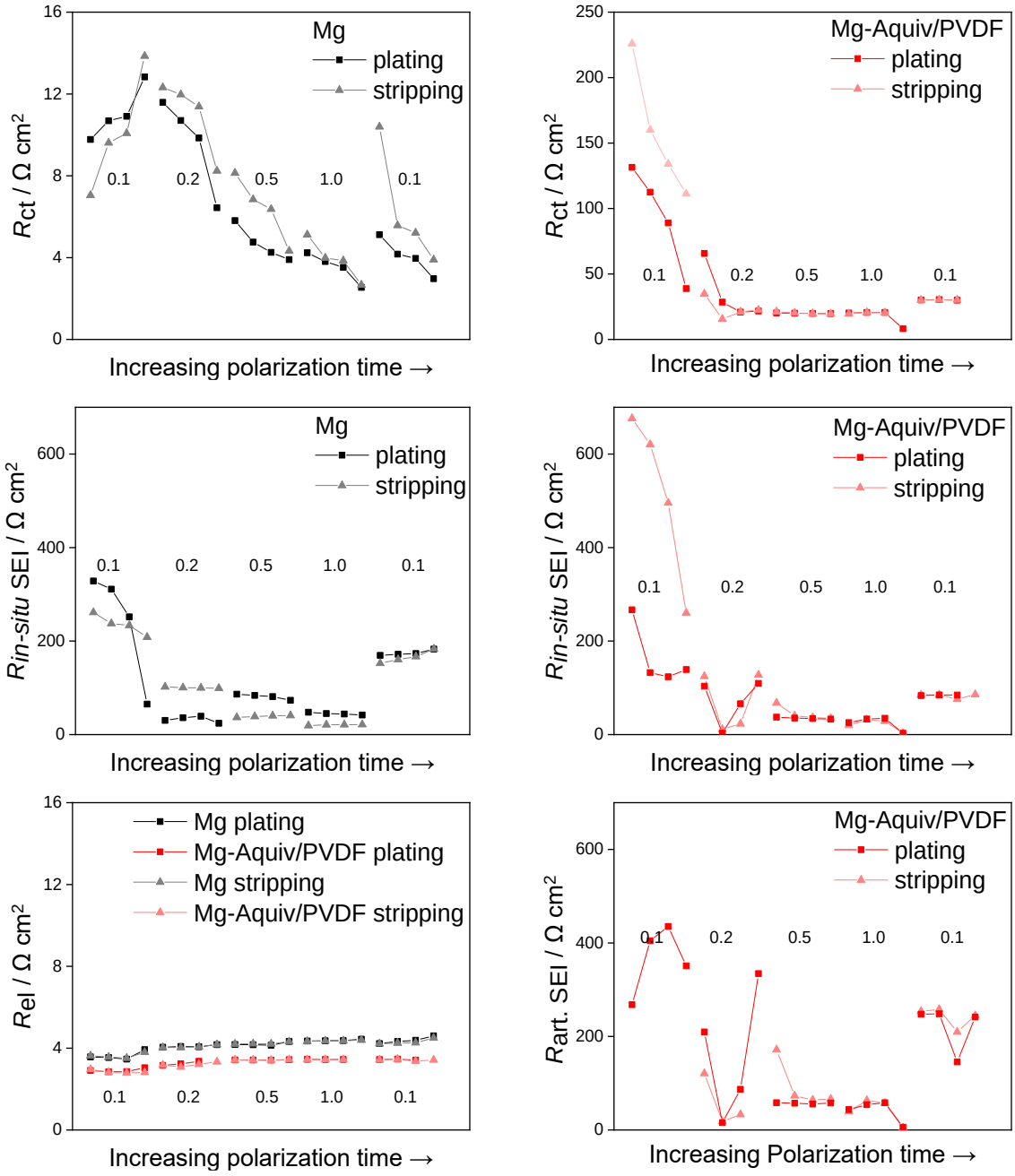

Figure 4.17: Resistance evolution of Mg-Mg cells without artificial SEI (black) and with Aquivion/PVDF SEI (red) during stripping and plating at the current densities of 0.1, 0.2, 0.5, 1.0 and concluding 0.1 mA · cm^{-2}.

The ohmic resistance R_{el} remains approximately constant during the entire duration of the experiment. Since the same electrolyte was used in both cells, there is no significant difference. In contrast, the charge transfer resistance R_{ct} decreases with increasing current density (i). This correlates with equation 4.1.

$$R_{\mathrm{ct}} = \frac{b}{i} \tag{4.1}$$

The current density in the denominator results in a decrease in *R*ct with increasing values. Aquivion/PVDF coated anodes result in a $R_{\mathrm{ct}} > 200\,\Omega \cdot \mathrm{cm}^2$ at a current density of $0.1\ \mathrm{mA} \cdot \mathrm{cm}^{-2}$. R_{ct} is thus significantly increased compared to cells with an uncoated anode. Mass transport is inhibited by the thicker artificial SEI, especially during stripping at low current densities, whereas at higher current densities an equalization of the values of R_{CT} is observed. Although the trend of $R_{\textit{in-situ}\ \mathrm{SEI}}$ is not as clearly recognizable as with R_{ct}, there is a general decrease with increasing current density. CT and the formation of the SEI thus represent the processes at the anode/electrolyte interface in the cell with an uncoated anode. The artificial Aquivion/PVDF SEI cause a third dominant resistance $R_{\mathrm{artificial\text{-}SEI}}$. Especially at low current densities, $R_{\mathrm{artificial\text{-}SEI}}$ is temporarily above $400\,\Omega \cdot \mathrm{cm}^2$. Similar to the *in-situ* formed SEI, there is a trend towards lower resistances at higher current densities. It must be noted that the higher surface area results in a general decrease in all resistances with increasing test duration.

4.4.4 Mg-Mg cell with artificial SPEEK/PVDF SEI

In addition to the artificial Aquivion/PVDF SEI, the influence of the SPEEK/PVDF SEI on the processes on the Mg surface was investigated. Previous SEM analyses as well as the galvanostatic cycling test have shown an inhomogeneous coating of the anode in this case. The Bode representations of a Mg-Mg cell with Mg-SPEEK/PVDF anodes during OCV before and after polarization at different current densities are given in Figure 4.18. To complete, the Bode plots during OCV after the respective polarization phases after 0.1, 0.2, 0.5 and 1.0 $mA \cdot cm^{-2}$ are attached (Figure A9).

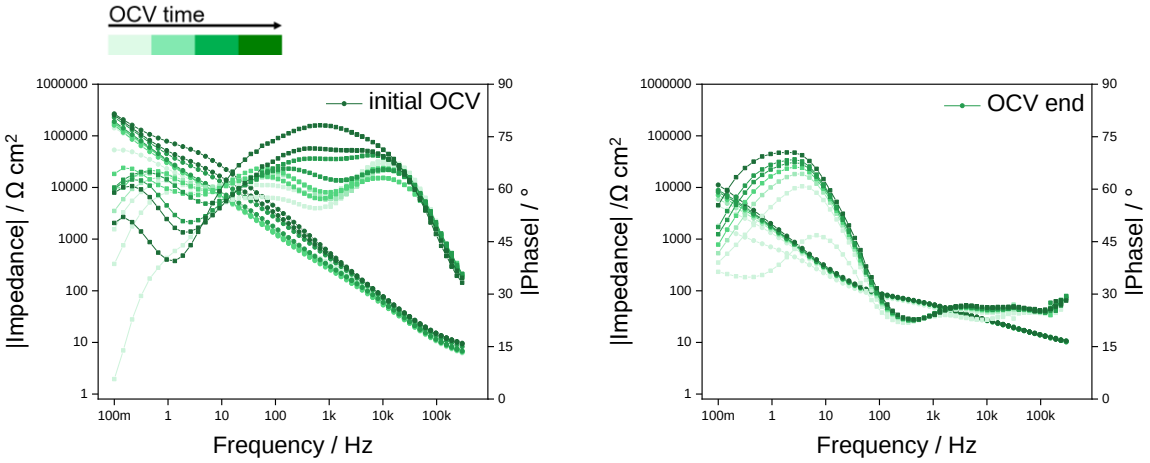

Figure 4.18: Bode plots of a Mg-Mg cell with artificial SPEEK/PVDF SEI during OCV before and after polarization at different current densities.

Compared to the cell with Aquivion/PVDF SEI described above, the individual processes in the OCV overlap less after assembly of the cell and the subsequent 50 h resting time. Three processes build up immediately after the cell has been assembled (light green). With increasing resting time (dark green), the distinction between HF and MF processes is no longer possible. After polarizing the cell at different current densities, the processes are shifted significantly to lower frequencies to be seen in the Bode plot of the last OCV phase (OCV end). In contrast to cells with artificial Aquivion/PVDF SEI, the adsorption layer continues to build up during the OCV phase and is not influenced by the artificial SEI. Based on the insights from the previous impedance characteristics, the relations of the CT, the *in-situ* SEI formation and the artificial SEI to the particular processes at the Mg electrolyte interface are described below. An overview

of the Bode representations of the Mg-Mg cell with SPEEK/PVDF SEI during stripping and plating at different current densities is given in Figure 4.19.

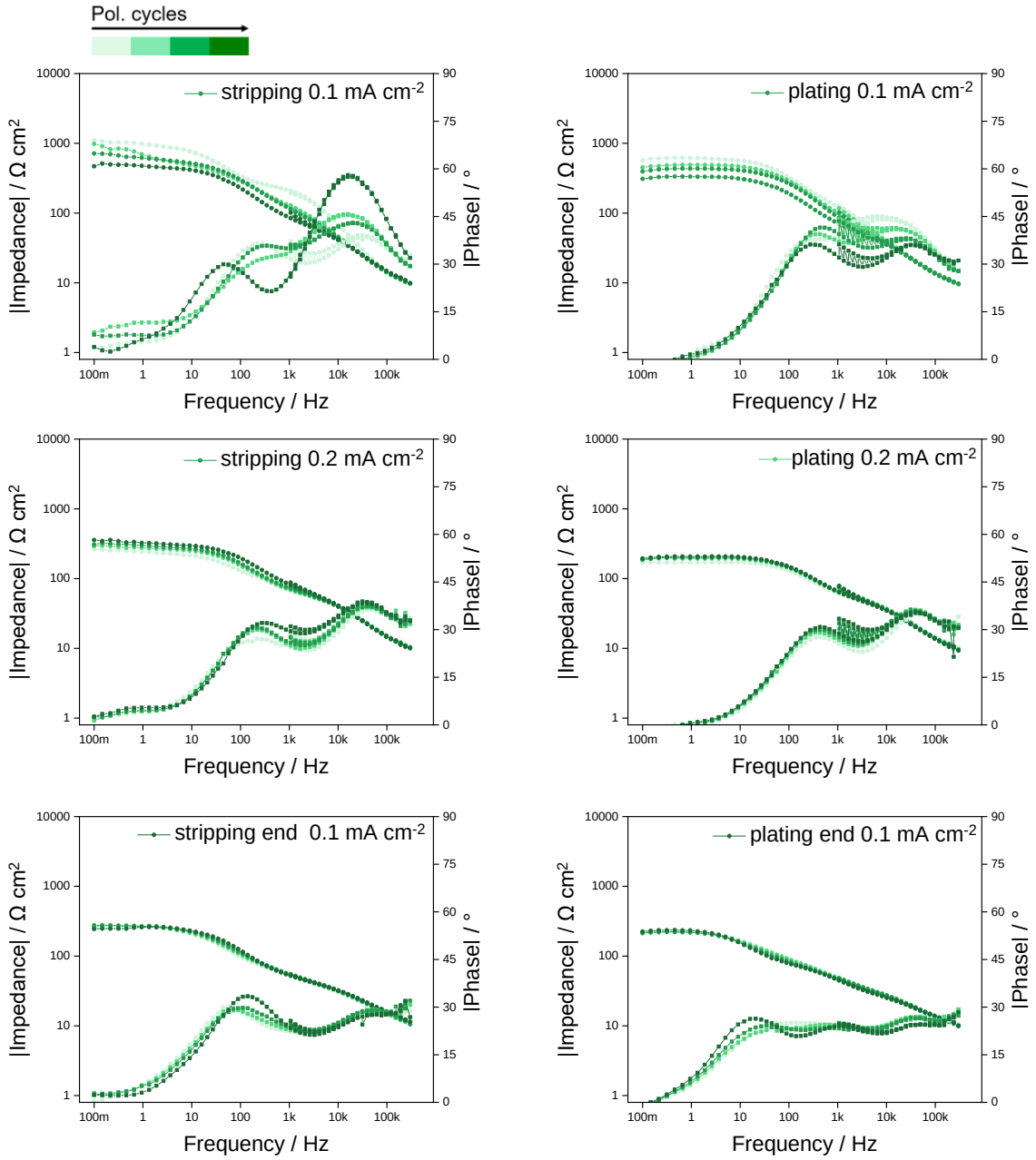

Figure 4.19: Bode plots of stripping and plating of a Mg-Mg cell with artificial SPEEK/PVDF SEI at 0.1, 0.2 and concluding 0.1 $mA \cdot cm^{-2}$.

During stripping and plating, two overall processes are present in the HF and MF regions. The HF process is assigned to the CT analogous to the previous characterization. In contrast to the

observations with the artificial Aquivion/PVDF SEI, the MF process occurs right from the start of the polarization at $0.1\ mA \cdot cm^{-2}$ due to the inhomogeneous distribution of the artificial SPEEK/PVDF SEI on the Mg anode. *In-situ* formed SEI components are deposited on the free Mg metal and cause the formation of the MF process. The inadequate coating also explains the lack of LF process compared to the artificial Aquivion/PVDF SEI. Furthermore, the large surface porosity during polarization (recognizable by the decreasing phase of all processes) is additional an indication of the inhomogeneity of the surface.

4.4.5 Mg-Mg cell with artificial PAN SEI

As described in Chapter 4.3, PAN differs in chemical and physical properties from the ionomers Aquivion and SPEEK. The conductivity of the artificial PAN SEI results mainly from the addition of the Mg conductive salt. The effects on the impedance characteristics are described below. Figure 4.20 shows the Bode representations of a Mg-Mg cell with Mg-PAN anode during OCV before and after polarization at different current densities. Supplementing this, the Bode plots of the OCV after the polarization at 0.1, 0.2, 0.5 and 1.0 $mA \cdot cm^{-2}$ are given in the appendix (Figure A11).

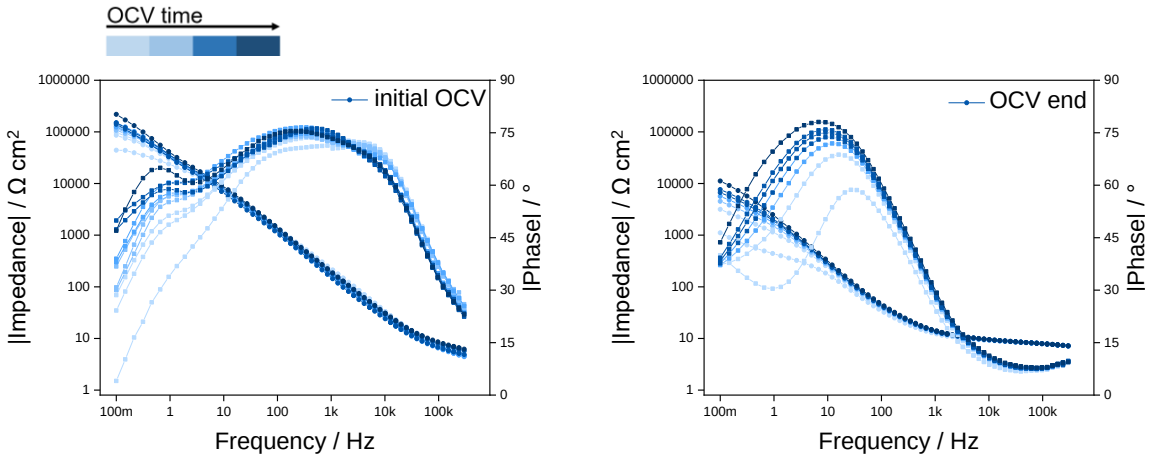

Figure 4.20: Bode plots of a Mg-Mg cell with artificial PAN SEI during OCV before and after polarization at different current densities.

As shown in Figure 4.20, there are no significant differences to the previous observations in the Bode plot of the OCV during the initial 50 h resting time (OCV start). However, in addition to

the known formation of the process in the HF region, another process in the LF region is identified in the following OCV spectra (Figure A11). After the polarization of the cell, the processes shift to lower frequencies and only one overall process builds up in the MF region (Figure 4.20 OCV end). Due to the increase in impedance in the range < 100 mHz it is assumed that there is another process in the LF region that is not visible in the frequency range of the experiment.

Bode representations of the cell with PAN-coated anodes during stripping and plating at different current densities are given in Figure 4.21.

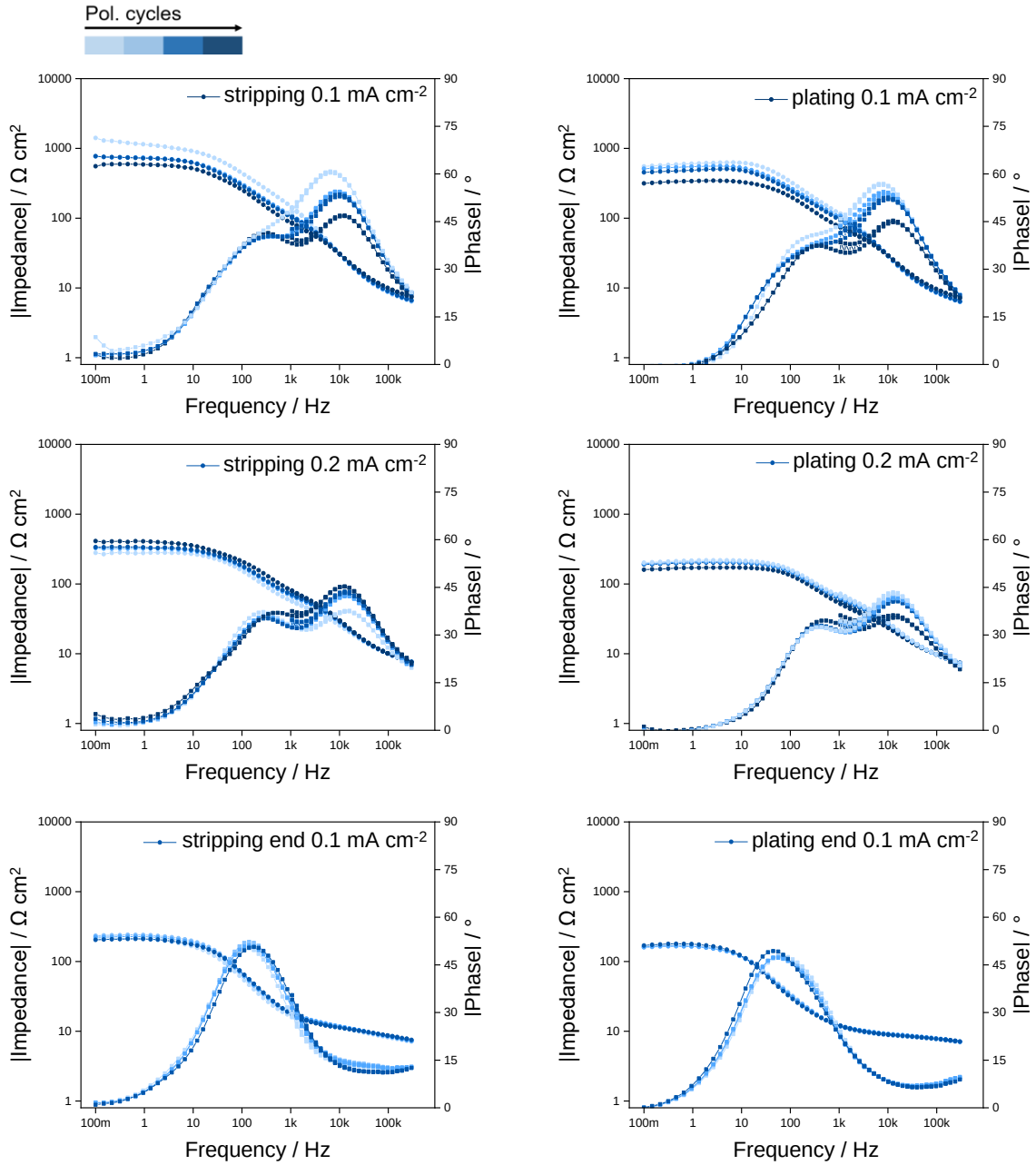

Figure 4.21: Bode plots of stripping and plating of a Mg-Mg cell with artificial PAN SEI at 0.1, 0.2, 1.0 and concluding 1.0 mA · cm^{-2}.

During stripping and plating at 0.1 and 0.2 mA · cm^{-2} two processes are present in the HF and MF region. As already observed in the OCV, the processes slow down with increasing polarization time. Due to the large shift in the processes, a distinct assignment of the processes analogous to the previous cells is not possible. One possible explanation is a very large surface porosity of the anode surface caused by the polarization of the cell. Consequently, the surface roughness leads to far from ideal capacitive double layer, which exhibiting a phase angle that

is not indicating a process. Indeed, the impedance exhibits a small but steady increase in the HF region. Furthermore, the diffusion to the Mg surface can be inhibited by a too thick artificial SEI coating. This explain the slowing down of the LF process and consequently the associated visibility in the frequency range < 100 mHz.

4.5 Electrochemical impedance spectroscopy of Mg-S cells

The influence of the cathode side namely dissoluted sulfur species on the impedances was investigated in Mg-S full cells. Based on the insights from the impedance characteristics of symmetrical Mg-Mg cells, a deeper understanding of the particular processes at the anode/electrolyte interface in Mg-S cells could be obtained.

4.5.1 OCV and initial cycle

The main changes in the cell can be observed during the initial OCV and the subsequent first galvanostatic cycle by wetting the electrodes, dissolving sulfur species of the cathode and reaction of the Mg surface with the electrolyte. Figure 4.22 compares the Bode plots of OCV and the subsequent discharge of a cell without artificial SEI (black) and cells with Aquivion/PVDF (red), SPEEK/PVDF (green) and PAN SEI (blue).

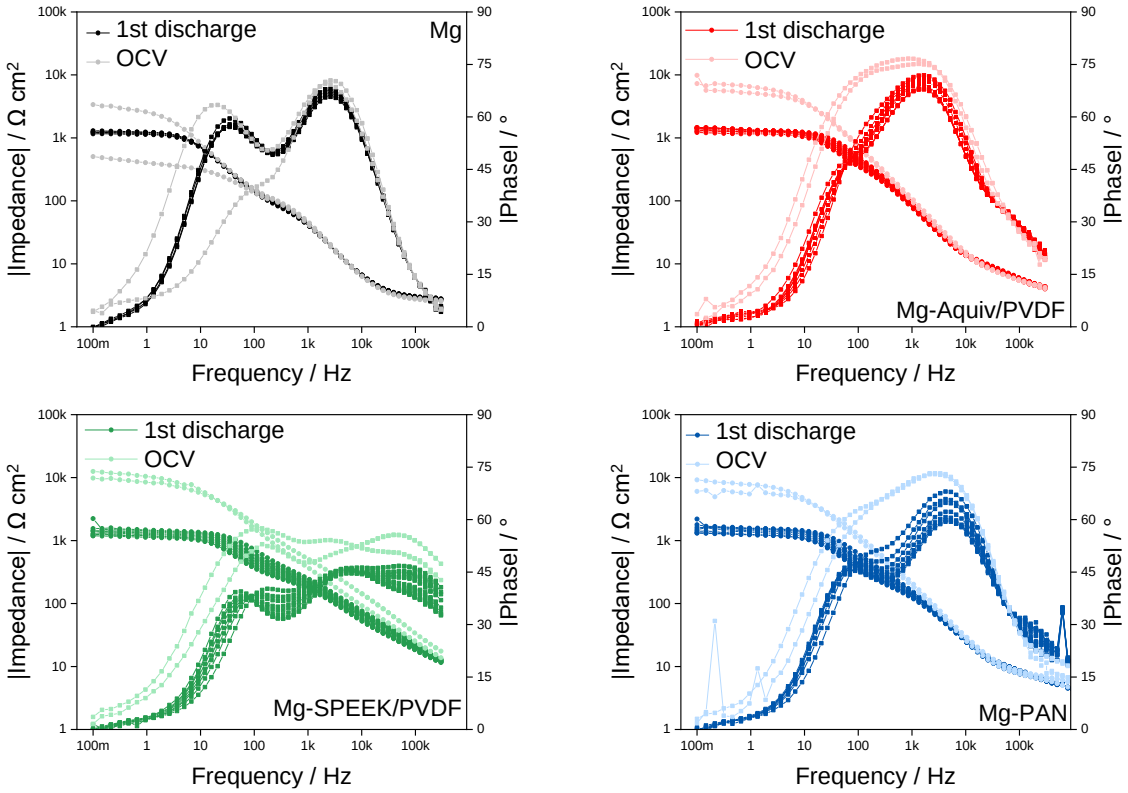

Figure 4.22: Bode plots of Mg-S cells without artificial SEI and with Aquivion/PVDF, SPEEK/PVDF and PAN SEI during OCV and subsequent first discharge cycle at $0.1\ \mathrm{mA} \cdot \mathrm{cm}^{-2}$.

In cells with artificial Aquivion/PVDF and PAN SEI two process are visible during the initial OCV. However, it is not possible to clearly separate these processes. In contrast, in cells without a coating or artificial SPEEK/PVDF SEI separable processes (HF and MF process) are already present during resting time. The similarity of the artificial SPEEK/PVDF SEI to the uncoated anode again confirms the assumption of a thin, inhomogeneous coating of the anode. As previously observed in symmetrical Mg-Mg cells *in-situ* SEI formation through electrolyte decomposition even takes place without applying a current. According to this the MF process is attributed to the formation of an *in-situ* SEI on the uncoated anode. In the subsequent first discharge, two processes are also more defined and clearly separable with Aquivion/PVDF- or PAN-coated anodes. One possibility is to assign this process to the artificial SEI. Consequently, a clear distinction between the *in-situ* SEI process and the artificial SEI process in the analyzed Mg-S cells is not possible. Another possibility is the assignment of the MF process to the *in-situ* SEI analogous to the uncoated anode due to partial failure of the artificial SEI. This is supported by the presence of an LF process in the Nyquist plot of the cell with Aquivion/PVDF anode (Figure A15). The previous characterization of symmetrical Mg-Mg cells showed similar time constants for the adsorption and the diffusion through the artificial SEI which causes an overlay of the impedance response in the LF region. Due to the low current density of $0.1\ \mathrm{mA \cdot cm^{-2}}$ it is therefore also possible that the mentioned LF process represent an incomplete removal of the adsorption layer that has formed during the OCV. The faster process in the HF region is assigned to the CT based on the previous evaluations in symmetrical Mg-Mg cells. It must be noticed that the process is slowed down by the contribution of sulfur species to the *in-situ* SEI formation.

Figure 4.23 compares the position of the processes during the first discharge in Mg-S full cells and the stripping in symmetrical Mg-Mg cells at $0.1\ \mathrm{mA \cdot cm^{-2}}$.

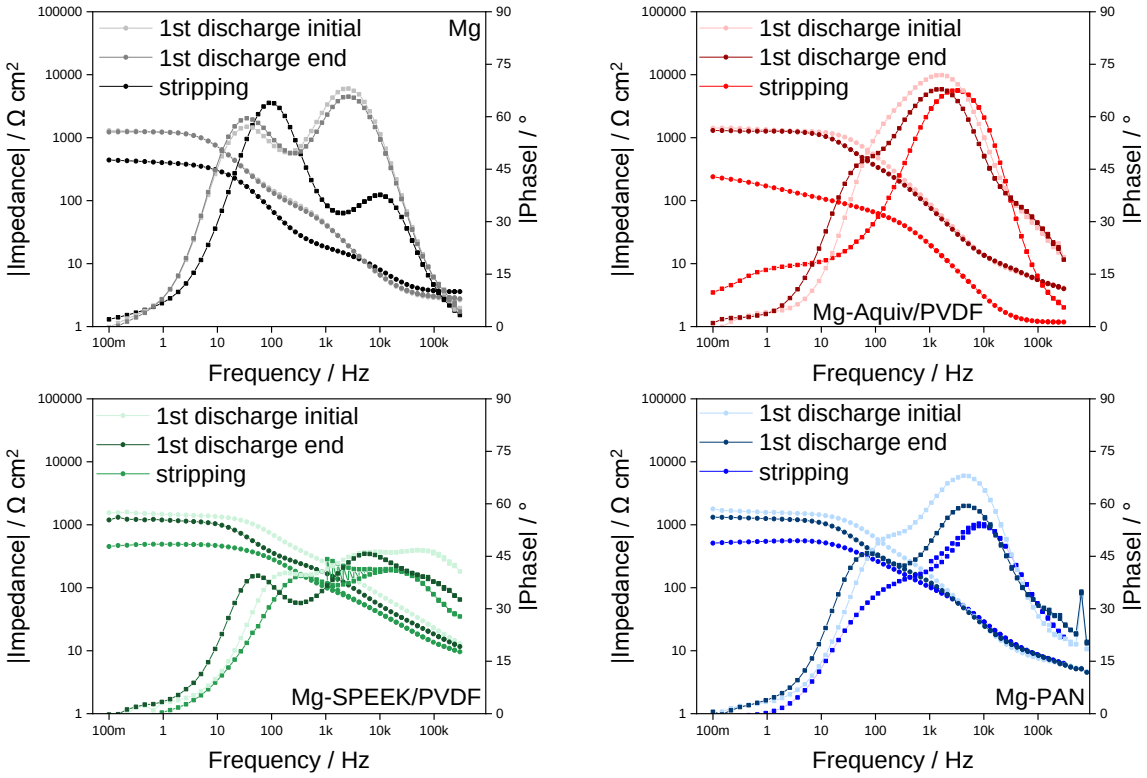

Figure 4.23: Comparison of the processes during the first discharge in Mg-S full cells and the stripping in symmetrical Mg-Mg cells at 0.1 mA · cm^{-2}.

Figure 4.23 proves a qualitative congruence of the position of the processes during the discharge in Mg-S full cells and the stripping in symmetrical Mg-Mg cells. This statement also applies to the processes during charge/plating (Figure A21 to Figure A24). In a symmetrical Mg-Mg cell the Aquivion/PVDF SEI (red) results in an additional process in the LF region, which is assigned to the artificial SEI (Chapter 4.4.1). In Mg-S full cells with the same Mg-Aquivion/PVDF anode, the MF process slows down during the first charging of the cell and shifts to a lower frequency range. The same is shown with a Mg-PAN anode during charging (Figure 4.24).

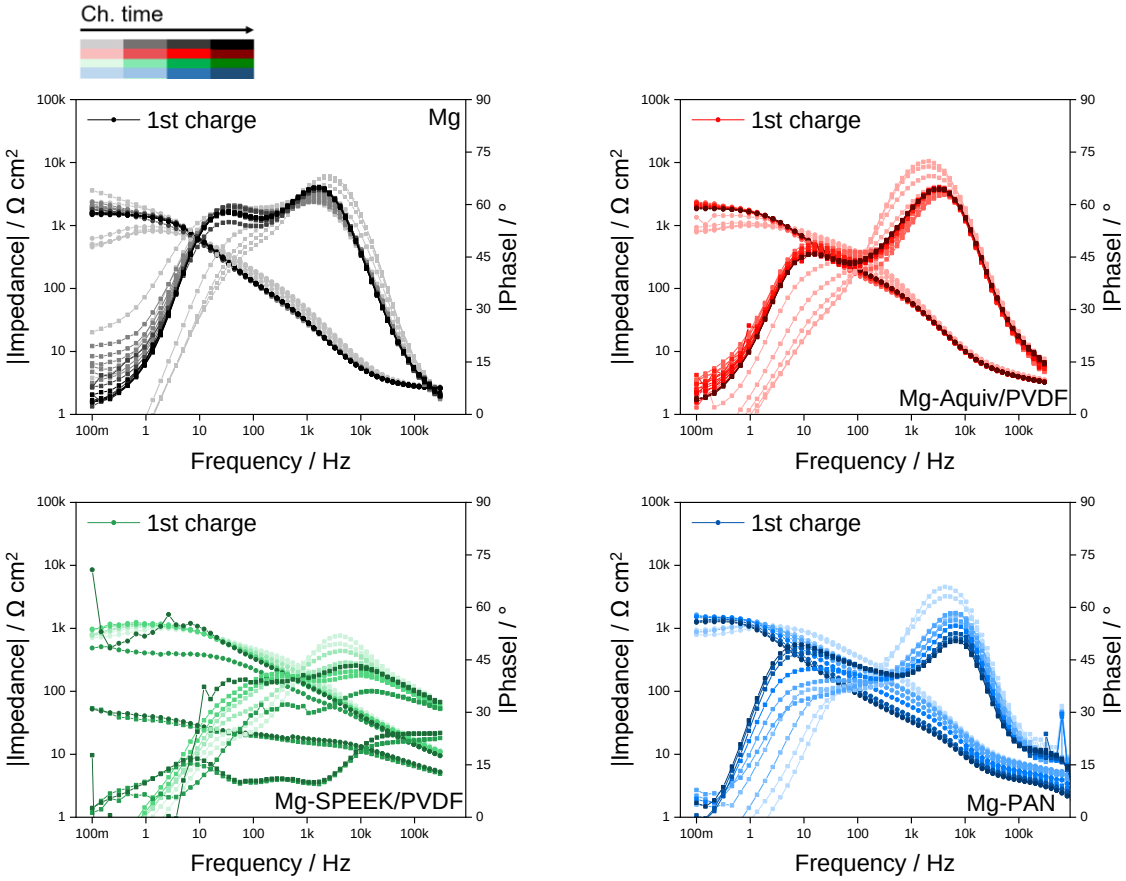

Figure 4.24: Bode plots of Mg-S cells without artificial SEI and with Aquivion/PVDF, SPEEK/PVDF and PAN SEI during first charge cycle at 0.1 mA · cm^{-2}.

In general, there is an increasing surface porosity in the charged state of the cells indicated by the reduced phase angle of the HF process (marked by the color gradient from light to dark in the Bode plots in Figure 4.24). Extreme SOC-dependent deviations in the total impedance occur, which are shown particularly in the cell with artificial SPEEK/PVDF SEI. The partial break-up of the coating during the first charge cycle, which causes extreme inhomogeneity of the anode surface, is a possible reason. This is supported by the initially higher impedance due to the artificial SEI and the subsequent decrease in impedance after the coating fails. Nyquist plots (Figure 4.25) of the cells underline the SOC-dependent differences in the impedances during the charge process. The irregularities when charging a cell with artificial SPEEK/PVDF SEI are represented as inductive loops. As illustrated in Figure 4.25 inductive loops also occur in cells without a coating, Aquivion/PVDF or PAN SEI. However, it is noticeable that in this case the loops only appear at the beginning of the charge process. Figure 4.25 shows as an example the Nyquist representations of Mg-S cells during the first charge cycle at

0.1 mA · cm^{-2}. It is worth to mention, that inductive loops are also observed in higher charge cycles (Figure A13 to Figure A20).

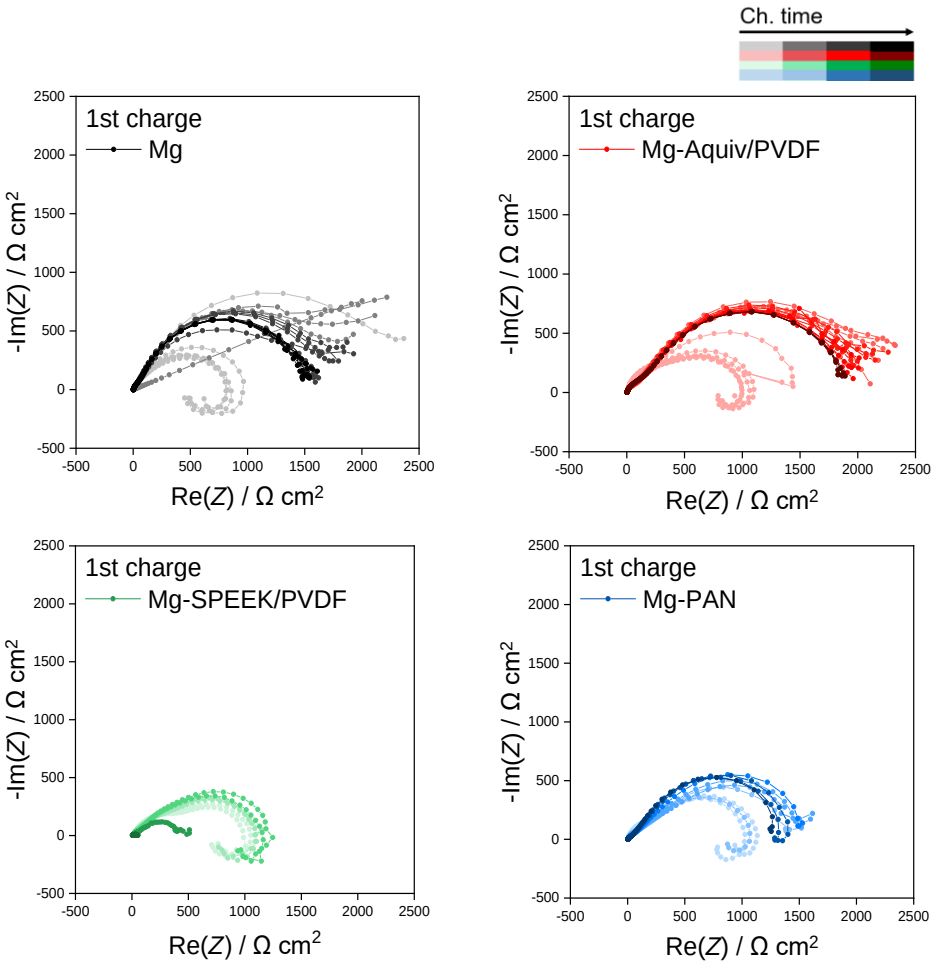

Figure 4.25: Comparison of the Nyquist representations of Mg-S cells with and without artificial SEI during the first charge cycle at 0.1 mA · cm^{-2}.

Discussions about the origin of inductive loops are controversial in the literature. The formation of the SEI is often cited as a possible origin. However, macroscopic causes such as geometric effects or the cell configuration can also be responsible for the formation.[90,91] Another explanation is the used cell design, in particular reference electrodes and springs. Dugas *et al.* showed that the use of Mg metal reference rings in three electrode configurations can easily lead to inductive loops.[92] In the present EIS measurements, however, inductive loops are mainly observed during charge process in Mg-S full cells. It is obvious that at the beginning of the charge process there is the greatest electrochemical asymmetry between the electrodes, which in this case leads to the formation of inductive loops.

4.5.2 Subsequent cycles

In addition to the initial cycle, the first ten cycles of the cells were considered. A comparison between the impedance characteristics of pristine Mg anodes and Mg anodes with artificial Aquivion/PVDF SEI during the second, fifth and tenth cycle is given in Figure 4.26.

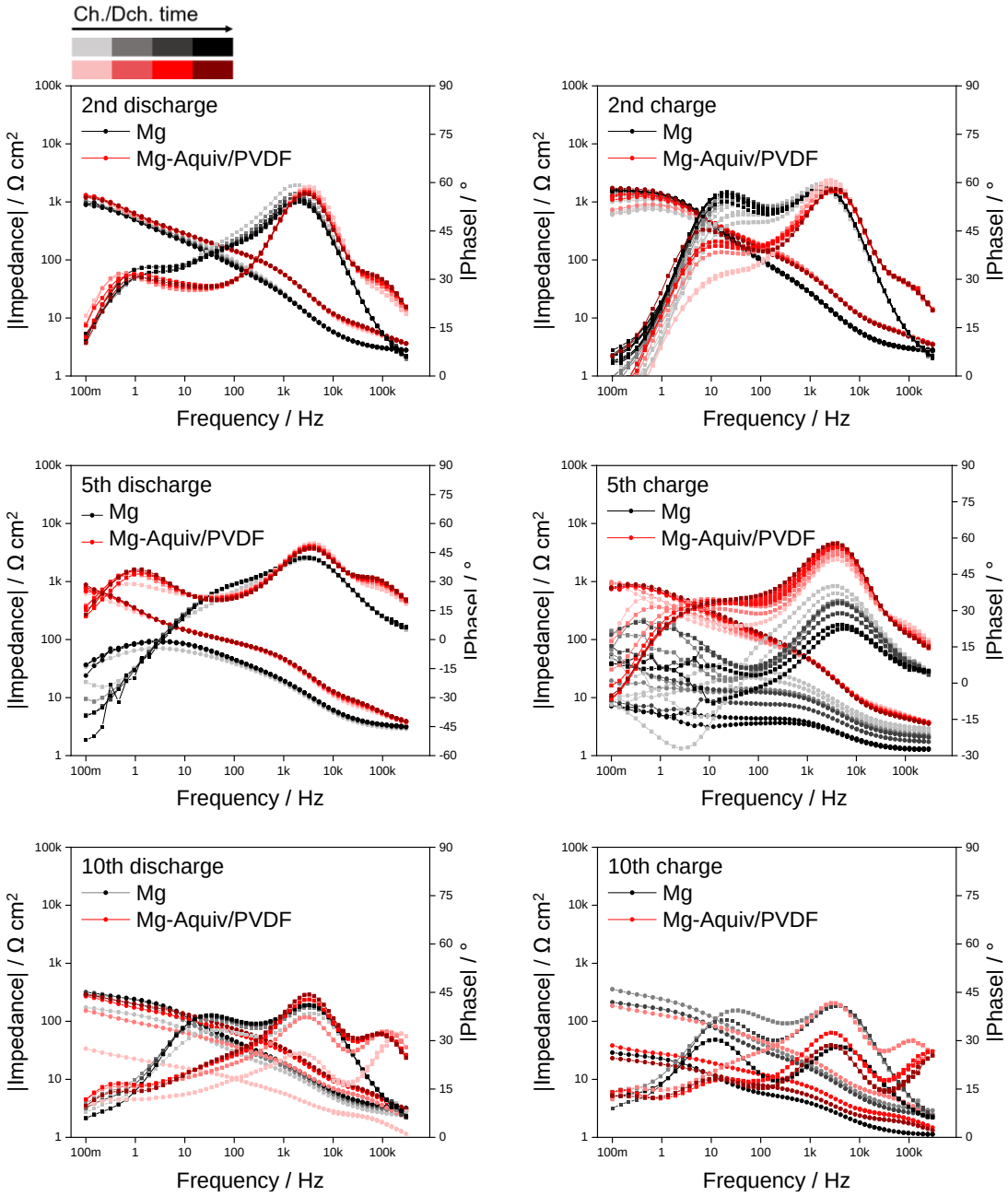

Figure 4.26: Bode plots of a Mg-S cell without artificial SEI (black) and with artificial Aquivion/PVDF SEI (red) during the second, fifth and tenth cycle at 0.1 $mA \cdot cm^{-2}$.

As already observed during the first discharge cycle, the MF process of the artificial Aquivion/PVDF-coated anode slows down during discharge and with increasing number of cycles compared to the uncoated anode. With increasing cycle numbers, the impedance component of the CT decreases while the component of the SEI increases, whereas the total impedance remains roughly the same. The cell with artificial Aquivion/PVDF SEI shows an additional process in the HF region (> 10^4 Hz), which is visible due to the slower CT. However, it is assumed that this is due to measurement artifacts. At higher cycles, the SOC-dependent irregularities increase, especially during charging of the cells.

The development of the particular processes in Mg-S cells with artificial SPEEK/PVDF SEI during the second, fifth and tenth cycle is illustrated in Figure 4.27.

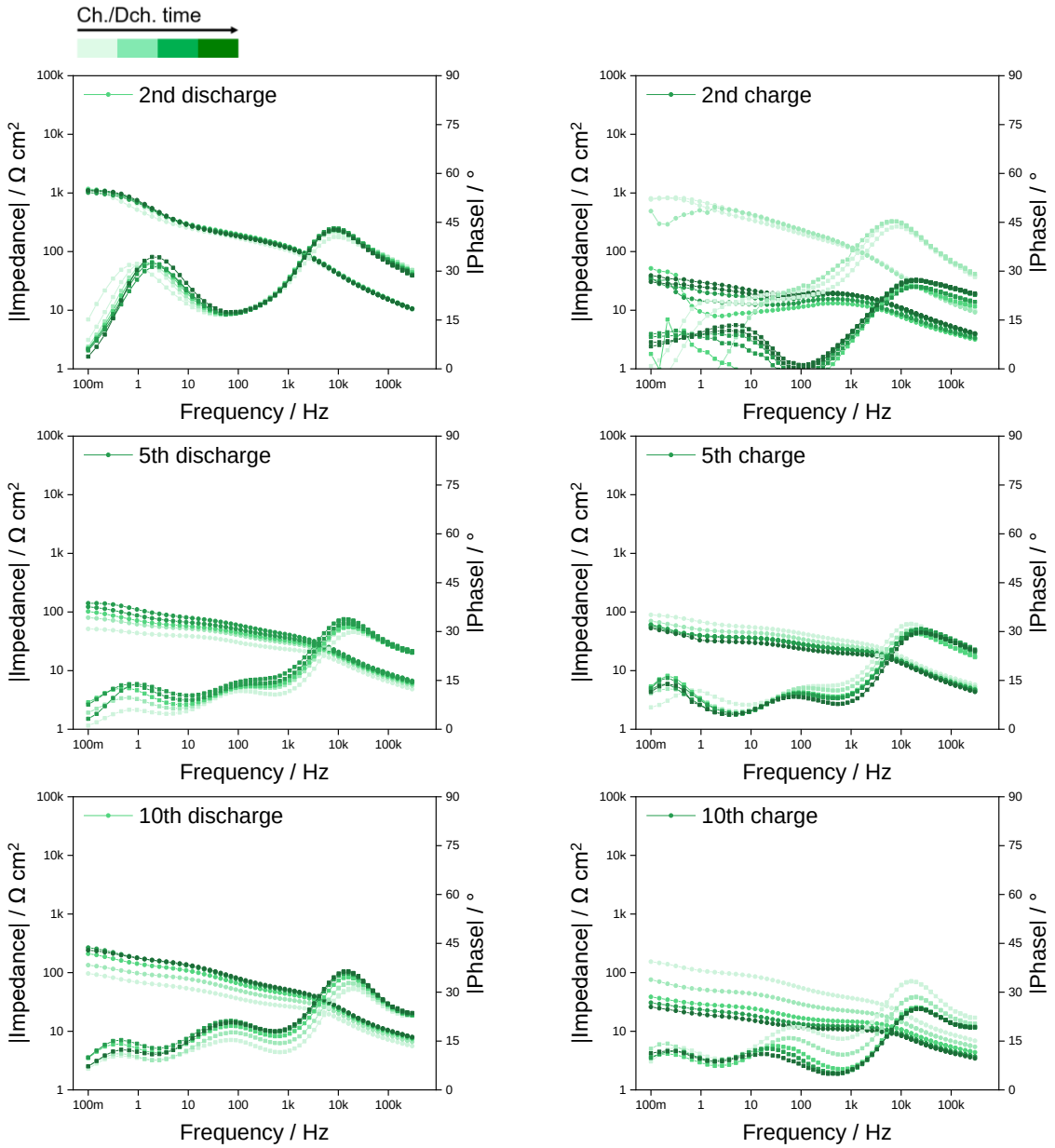

Figure 4.27: Bode plots of a Mg-S cell with artificial SPEEK/PVDF SEI during the second, fifth and tenth cycle at 0.1 $mA \cdot cm^{-2}$.

During the first cycle, there is a strong change in the surface porosity indicated by the smaller phase angle values of the Bode plot. Furthermore, a change in the total impedance of the cell was observed. It was analyzed that this was due the breakdown of the coating. This is also confirmed by the Bode plots of the second, fifth and tenth cycle (Figure 4.27). An approximately constant total impedance is shown. In addition, the formation of a further process in the MF region with increasing cycle numbers indicates a failure of the coating. Due to the

inadequate protection provided by the artificial SEI, *in-situ* formed SEI components are deposited on the unprotected areas of the Mg anode even with a low number of cycles. The selective break-up of the artificial SEI layer also causes the constantly high surface porosity. This is illustrated by the significantly smaller phase angle values of the processes of the cell with Mg-SPEEK/PVDF anode compared to the cell with Aquivion/PVDF anode. At the same time, the phase difference in the Bode plot shows the much higher stability and homogeneity of the artificial Aquivion/PVDF SEI.

The bode plots of the second, fifth and tenth cycle of the Mg-S cell with artificial PAN SEI are given in Figure 4.28.

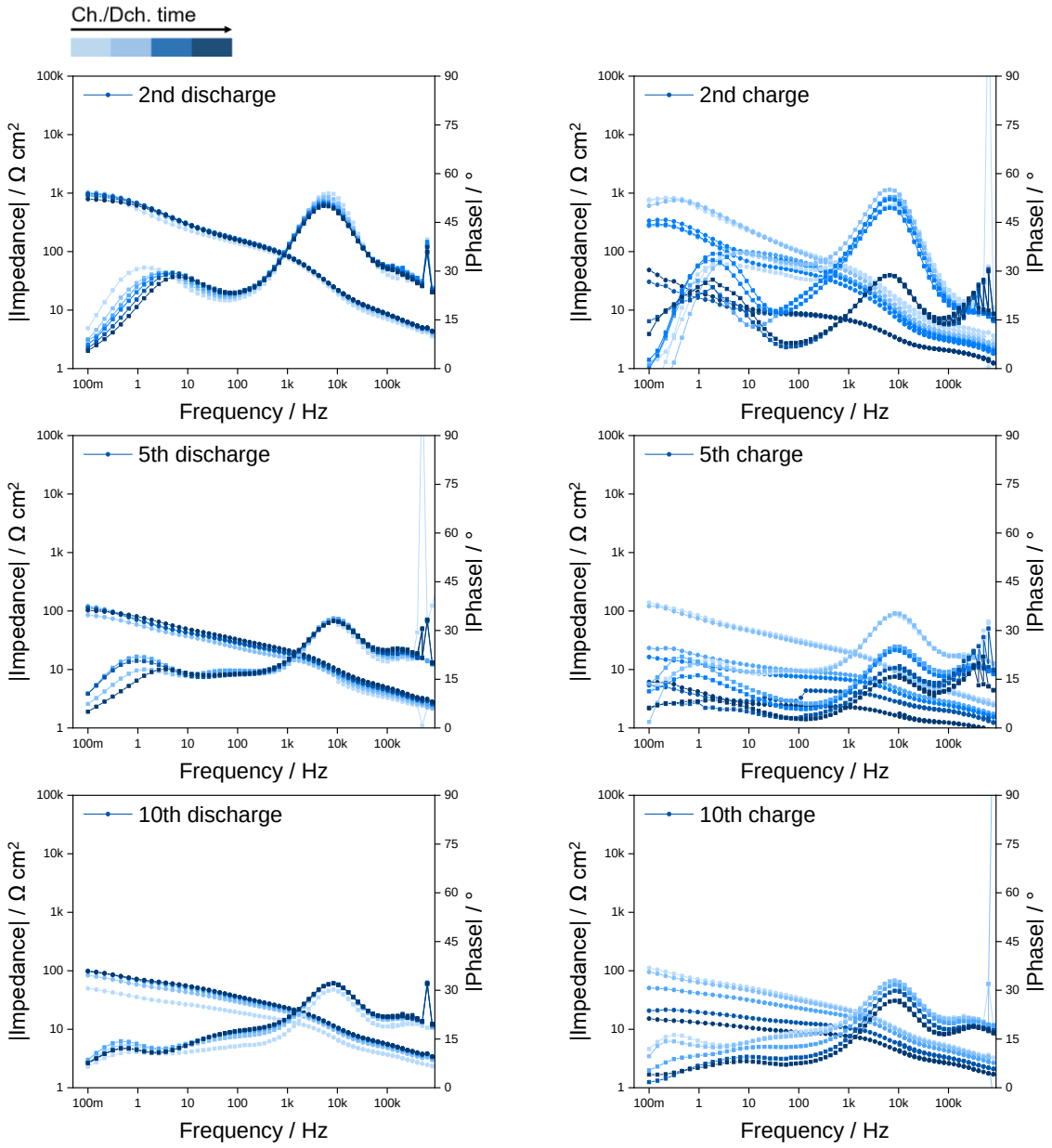

Figure 4.28: Bode plots of a Mg-S cell with artificial PAN SEI during second, fifth and tenth cycles at 0.1 $mA \cdot cm^{-2}$.

Analogous to the cell with artificial Aquivion/PVDF SEI, there is a shift in the SEI process to lower frequencies with an increasing number of cycles. This characteristic thus represents a significant difference to the cell without a coated anode and indicates the assignment of this process to the artificial SEI. The surface porosity of the Mg-PAN anode increases with increasing cycle duration illustrated by the smaller phase angle values indicating a change in the structure of the artificial SEI during cycling. Previous knowledge has shown that the artificial PAN SEI is thicker than an *in-situ* formed SEI. The increased surface porosity

therefore does not result from the layer breaking up, but rather from an inhomogeneous aging of the coating during cycling. SEM images of the artificial PAN SEI confirm this (Chapter 4.2).

4.4.5 Conclusion – interfacial processes

Insights about the interfacial processes at the Mg anode are obtained by means of pseudo-galvanostatic EIS measurements in symmetrical Mg-Mg cells. During polarization, two overall processes build up with the uncoated Mg anode, which are assigned to a fast CT process (HF region) and a slower process (MF region) through the formation of an *in-situ* SEI. Anodes completely coated with Aquivion/PVDF show the formation of another process in the LF region due to the artificial SEI. As the polarization time increases, the breaking of the artificial SEI causes the deposition of *in-situ* SEI components on the Mg anode. This leads to three overall processes in the case of the artificial SEI coated anode – namely CT, *in-situ* SEI and artificial SEI. During OCV, the formation of an adsorption layer is observed in a frequency range similar to the artificial SEI.

The coating of the Mg anode with an artificial PAN SEI leads to a slower diffusion to the Mg surface. Thus, the process of the artificial SEI shifts to a very low frequency range < 100 mHz. With an increasing number of cycles, the surface porosity on the Mg surface increases significantly, which indicates a change of the surface of the artificial SEI.

A thin SPEEK/PVDF coating led to a rapid breakdown of the artificial SEI. This results in the formation of an *in-situ* SEI after just a few cycles, as shown through the formation of the MF process.

The contribution of sulfur species to interfacial layer formation at the Mg anode was investigated in Mg-S full cells during OCV and the subsequent first ten cycles. All cells show two processes during initial OCV. However, the processes can only be clearly separated into an HF and MF process for the uncoated anode. With an Aquivion/PVDF- or PAN-coated anode the separation of the processes is shown in the subsequent initial discharge/charge cycle.

4.6 Galvanostatic cycling of Li-S cells

In addition to Mg, the applicability of artificial SEI protection on Lithium (Li) metal anodes was investigated. Main components of the coatings were the hydrocarbon-based ionomers s-PSO2-220 (IEC = 4.55 meq $\cdot$ g^{-1}) and SPEEK (IEC = 2.7 meq $\cdot$ g^{-1}) as well as the perfluorinated ionomers Aquivion (IEC = 1.3 meq $\cdot$ g^{-1}) and Nafion (IEC = 0.9 meq $\cdot$ g^{-1}) (the ionomers are described in more detail in Chapter 4.3.1). In order to achieve a stable coating, PVDF was used as a binder. Coating of Li anodes was done via dip coating, whereby a complete coating of the anode is ensured. It should be noticed that slight variations in the layer thickness cannot be excluded due to the coating process. An exchange of the proton (H^+) of the sulfonic acid group with Li^+ should takes place *in-situ* – analogous to the experiments in Mg-S cells. Furthermore, the *ex-situ* proton exchange of the s-PSO2-220 ionomer was successfully carried out confirmed using FTIR spectroscopy. Figure 4.29 compares the FTIR spectra of the unexchanged (H^+ form) and exchanged (Li^+ form) s-PSO2-220 ionomer.

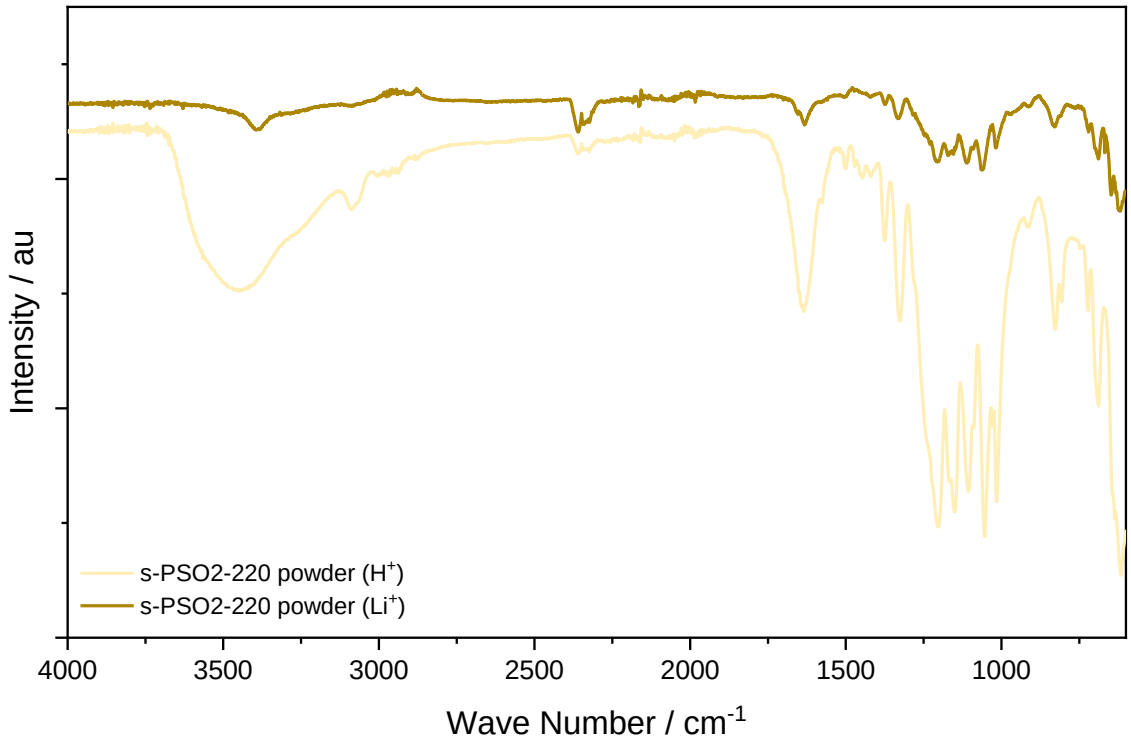

Figure 4.29: Comparison of the FTIR spectra of s-PSO2-220 (H^+) and s-PSO2-220 (Li^+) over the range of 600 – 4000 cm^{-1}.

The conversion from the H^+ form to the Li^+ form was verified by the less intensity of the broad -OH Band at 3400 cm^{-1}. As shown in Figure 4.29 the -OH stretching vibration decreases substantially due to the reduced OH groups compared to the s-PSO2-220 (H^+) reference spectrum.

In order to investigate the influence of the artificial SEI on the cycling performance of Li-S cells, coated anodes along with various cathodes were tested. For this purpose, a ball milled Sulfur/Ketjenblack (S/KB) cathode, a melt infiltrated S/KB cathode and a gas infiltrated Sulfur/Carbon-Aerogel (S/CA) cathode (Chapter 3.4.1) were utilized. In the case of ball milled S/KB cathodes, elemental sulfur is implemented in the conductive Ketjenblack matrix by simply mixing. Therefore, higher polysulfide shuttle redox during cycling is expected for the mixed electrode, compared to the gas or melt infiltrated electrodes, where the sulfur is confined in the pores. Melt infiltrated S/KB cathodes represent the current state of the art in Li-S cells, whereas gas infiltrated S/CA cathodes are currently the focus of research and are considered to be particularly stable indicating the quasi-solid-state reaction.

4.6.1 Li-S cells with artificial SEI and ball milled S/KB cathode

Different variants of the artificial SEI on Li anode in combination with the simple ball milled S/KB cathode (sulfur loading: 1.0 $mg \cdot cm^{-2}$) were employed. Firstly, the Li anode was coated with an s-PSO2-220/PVDF artificial SEI. The cathode coated using Aquivion/PVDF was further used with the intention to minimize the loss of active material and suppress the polysulfide shuttle. As a reference, a cell in which both the anode and the cathode were coated using Aquivion/PVDF was tested. Figure 4.30 compares the specific discharge capacity versus the number of cycles as well as the coulombic efficiency of the respective cells during galvanostatic cycling at C/3. Celgard 2500 separators and a 1 M LiTFSI DOL/DME electrolyte were used for cell assembly.

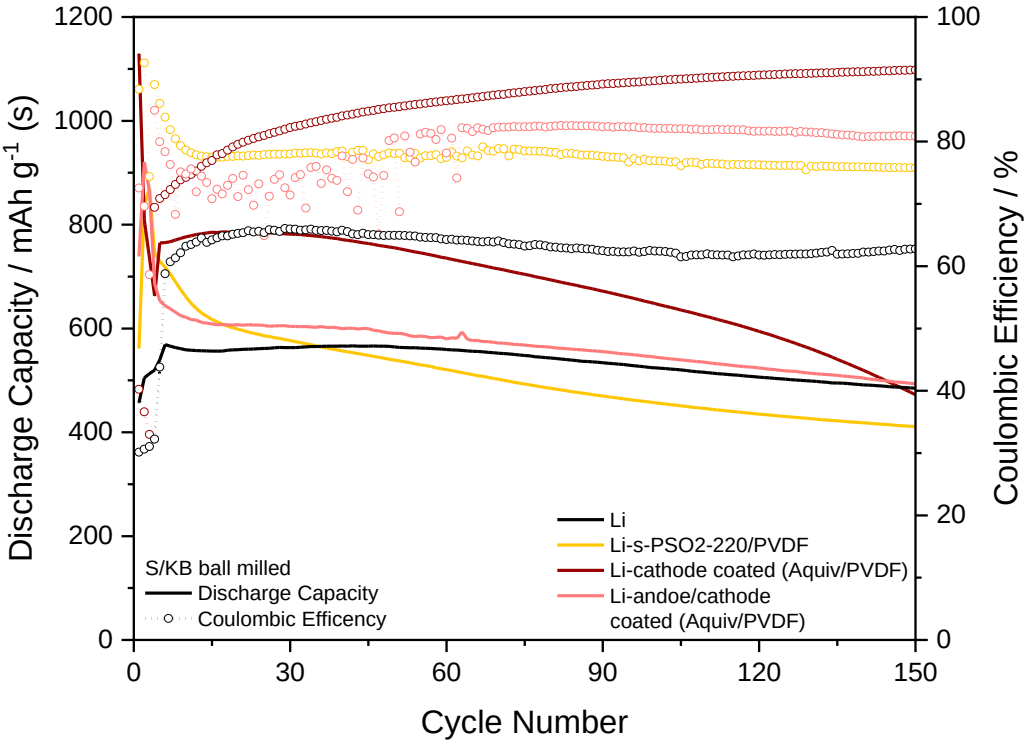

Figure 4.30: Cycling performance of Li-S cells with different artificial SEI and ball milled S/KB cathode at C/3 (electrolyte: 1.0 M LiTFSI DOL/DME, separator: Celgard 2500, sulfur loading: 1.0 $mg \cdot cm^{-2}$).

Cells with a coating show overall better coulombic efficiencies compared to the uncoated Li reference cell. Furthermore, the coating of the cathode leads to higher sulfur utilization as well as better cycling performance of the cell. As expected, the polysulfide shuttle is minimized by the coating and the loss of active sulfur material is reduced, resulting in a significantly higher capacity and an improved coulombic efficiency during galvanostatic cycling. However, this sample suffers from a sudden loss of capacity. This could be due to the stress build-up in the cathode upon conversion reaction of the sulfur to Li_2S causing 80% volume expansion which destroys the passivation film as well as the cathode. To further understand this in details, the cell comprised of both coated electrodes is taken into consideration. On the one hand, the cell with coated anode and cathode reveals a superior better cyclability while, the capacity and coulombic efficiency are lower than that of the cell with just coated cathode. This is mainly due to the reactivity of the Li anode with the Aquivion ionomer (Figure 4.31) which results in the loss of Li active material.

In contrast, the s-PSO2-220 ionomer is less reactive towards Li metal and has additionally a higher IEC than Aquivion. As shown in Figure 4.30 the protection of the anode with an artificial s-PSO2-220/PVDF SEI enhances the discharge capacity during the first 30 cycles compared to the uncoated Li reference. In the following cycles, however, the polysulfide shuttle is not effectively suppressed by the artificial s-PSO2-220/PVDF SEI and the capacity drops. Nevertheless, a better coulombic efficiency is observed compared to the Li reference cell. However, the cathode here still suffers from low sulfur utilization.

Post-mortem images of the uncoated Li anode, Li-Aquivion/PVDF as well as Li-s-PSO2-220/PVDF anodes after > 150 galvanostatic cycles are given in Figure 4.31.

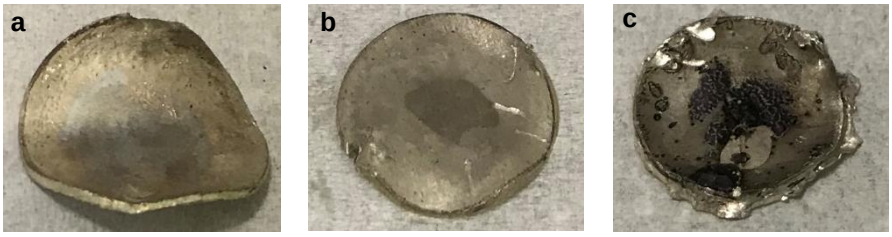

Figure 4.31: *Post-mortem* images of (a) the uncoated Li anode as well as (b) Li-s-PSO2-220/PVDF and (c) Li-Aquivion/PVDF.

An increased chemical reactivity of Li with the coating material is observed by the black discoloration of the Li-Aquivion/PVDF anode (c). In comparison s-PSO2-220 demonstrate less reactivity against Li. As already expected, the artificial s-PSO2-220/PVDF SEI collapse in the middle with increasing number of cycles and only partially protects the anode (b).

The respective specific charge capacity versus the number of cycles of the previously described Li-S cells is illustrated in Figure 4.32.

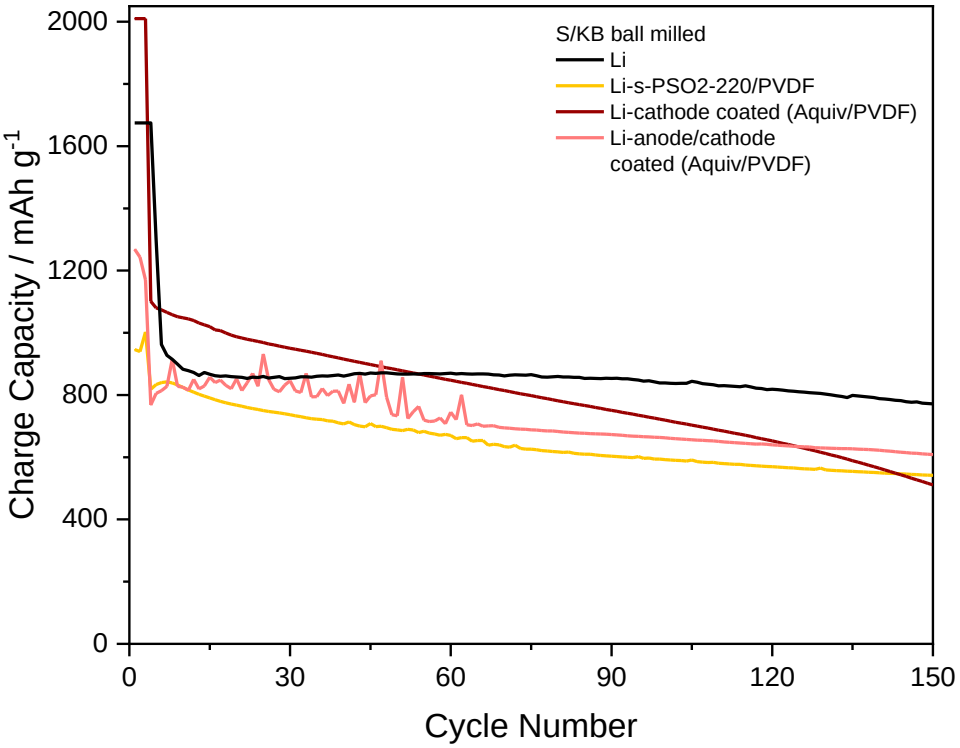

Figure 4.32: Charge capacity of Li-S cells with different artificial SEI and ball milled S/KB cathode at C/3 (electrolyte: 1.0 M LiTFSI DOL/DME, separator: Celgard 2500, sulfur loading: 1.0 $mg \cdot cm^{-2}$).

Cells without an anode coating show a higher initial irreversible charge capacity attributed to the *in-situ* SEI formation. However, a rapid decrease is observed in the first ten cycles. In contrast, the artificial SEI coating provides a better capacity retention during the charge process. Due to the previously observed high reactivity of Aquivion with Li metal, irregularities in the charge behavior of the cell occur. To achieve effective protection of Li anode by artificial SEI, ionomers with low reactivity to Li are therefore essential in combination with a stable cathode to prevent the artificial SEI from being disrupted by parasitic side reactions with sulfur species.

4.6.2 Li-S cells with artificial SEI and melt infiltrated S/KB cathode

In order to avoid the drawbacks of an unstable cathode, various artificial SEI in connection with a state-of-the-art S/KB cathode (sulfur loading: $0.45\ mg \cdot cm^{-2}$) were investigated. The implementation of sulfur via melt infiltration into the conductive Ketjenblack matrix results in a more stable cathode and minimized reactions of sulfur species and the artificial SEI. Figure 4.33 compares the specific discharge capacity versus the number of cycles as well as the coulombic efficiency of the respective cells during galvanostatic cycling at C/3. For cell assembly Celgard 2500 separators and a 1 M LiTFSI DOL/DME electrolyte were used.

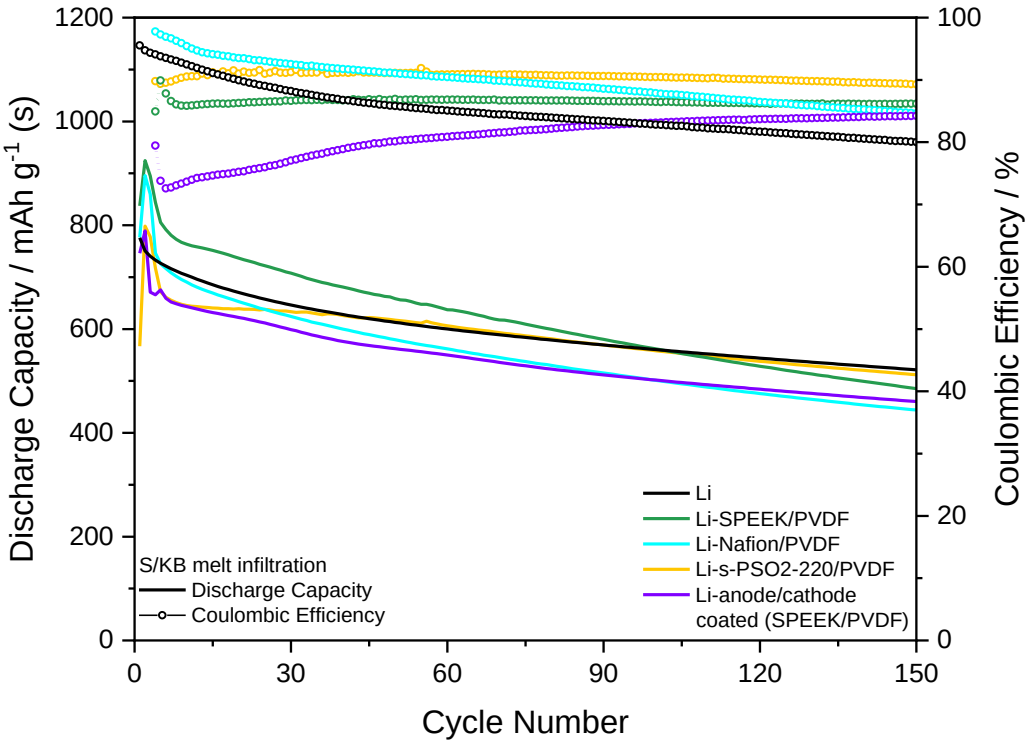

Figure 4.33: Cycling performance of Li-S cells with different artificial SEI and melt infiltrated S/KB cathode at C/3 (electrolyte: 1.0 M LiTFSI DOL/DME, separator: Celgard 2500, sulfur loading: $0.45\ mg \cdot cm^{-2}$).

Analogous to the previous characterization, cells with artificial SEI offer an improved coulombic efficiency compared to the uncoated Li anode. Artificial s-PSO2-220/PVDF and SPEEK/PVDF SEI lead to a constant coulombic efficiency of 90% and 85%, respectively. In comparison, the coulombic efficiency of the cell with an uncoated anode decreases with

increasing number of cycles from an initial 92% to 80% due to the irreversible capacity gain in the initial cycles induced by formation of the *in-situ* SEI.

It is noticeable that only the coulombic efficiency of the cell in which both the anode and the cathode were coated increases with increasing number of cycles. Figure 4.33 proves a stable discharge behavior of the cell, pointing out the irreversible capacity upon charge. This is also the reason for the overall lower discharge capacity compared to the Li reference.

Better cycling performances regarding to the discharge capacity are achieved with artificial s-PSO2-220/PVDF and SPEEK/PVDF SEI. The latter shows a capacity gain in the first 100 cycles compared to the uncoated Li anode. The subsequent drop in capacity supposedly results from the partial failure of the artificial SEI, whereby the Li anode is only partially protected and parasitic side reactions with polysulfide species can take place.

With a Nafion/PVDF SEI no improvement in cycling performance could be achieved. Analogous to the Aquivion ionomer, an increased reactivity of Nafion with Li metal could be observed, which leads to the loss of Li active material (Figure 4.34).

Figure 4.34: *Post-mortem* images of (a) the uncoated Li anode as well as (b) Li-Nafion/PVDF and (c) Li-SPEEK/PVDF.

Figure 4.34 shows *post-mortem* images of the uncoated Li anode (a), Li-Nafion/PVDF (b) and Li-s-SPEEK/PVDF anode (c) after > 150 galvanostatic cycles. Similar to Aquivion, black discolorations indicate an increased reactivity of the anode with the artificial Nafion/PVDF SEI. In contrast, the Li-SPEEK/PVDF anode shows less aging. The assumed break down of the coating cannot be assessed from a purely visual point of view.

Figure 4.35 compares the respective specific charge capacity versus the number of cycles of the previously described Li-S cells.

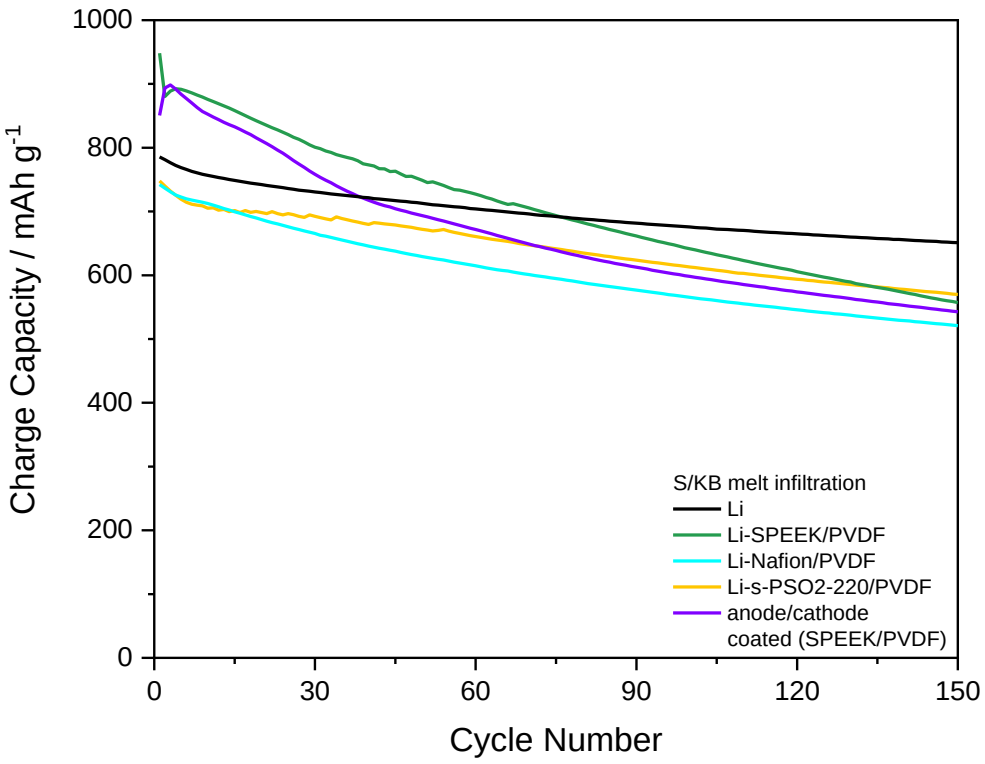

Figure 4.35: Charge capacity of Li-S cells with different artificial SEI and melt infiltrated S/KB cathode at C/3 (electrolyte: 1.0 M LiTFSI DOL/DME, separator: Celgard 2500, sulfur loading: 0.45 $mg \cdot cm^{-2}$).

At the initial cycles, the cell with coated anode and cathode shows significantly higher charge than discharge capacities indicating drawbacks at the Li deposition during charging. It is obvious that the artificial SEI of the anode or the additional coating of the cathode are too thick and thus the diffusion is inhibited. Furthermore, the low capacity retention of the cell with artificial SPEEK/PVDF SEI confirms a break-down of the coating with increasing number of cycles. Active material is lost and leads to a faster capacity fading.

4.6.3 Li-S cells with artificial SEI and gas infiltrated S/CA cathode

The previous characterization suggests the most effective protection of the Li anode with hydrocarbon-based ionomers achieved using ionomers s-PSO2-220 and SPEEK. In contrast, the perfluorinated ionomers Aquivion and Nafion showed an increased reactivity with Li and therefore have disadvantages in cycling performance. Another advantage of the s-PSO2-220/PVDF and SPEEK/PVDF SEI is the higher IEC compared to Aquivion/PVDF or Nafion/PVDF SEI. Therefore, a high cycle stability is expected in combination with a gas infiltrated S/CB aerogel cathode (sulfur loading: 0.5 $mg \cdot cm^{-2}$). This type of cathode is considered to be particularly stable and can effectively suppress the polysulfide shuttle.

Figure 4.36 compares the specific discharge capacity versus the number of cycles as well as the coulombic efficiency during galvanostatic cycling at C/3 of cells with artificial SPEEK/PVDF and s-PSO2-220/PVDF SEI. For cell assembly Celgard 2500 separators and a 1 M LiTFSI DOL/DME electrolyte were used.

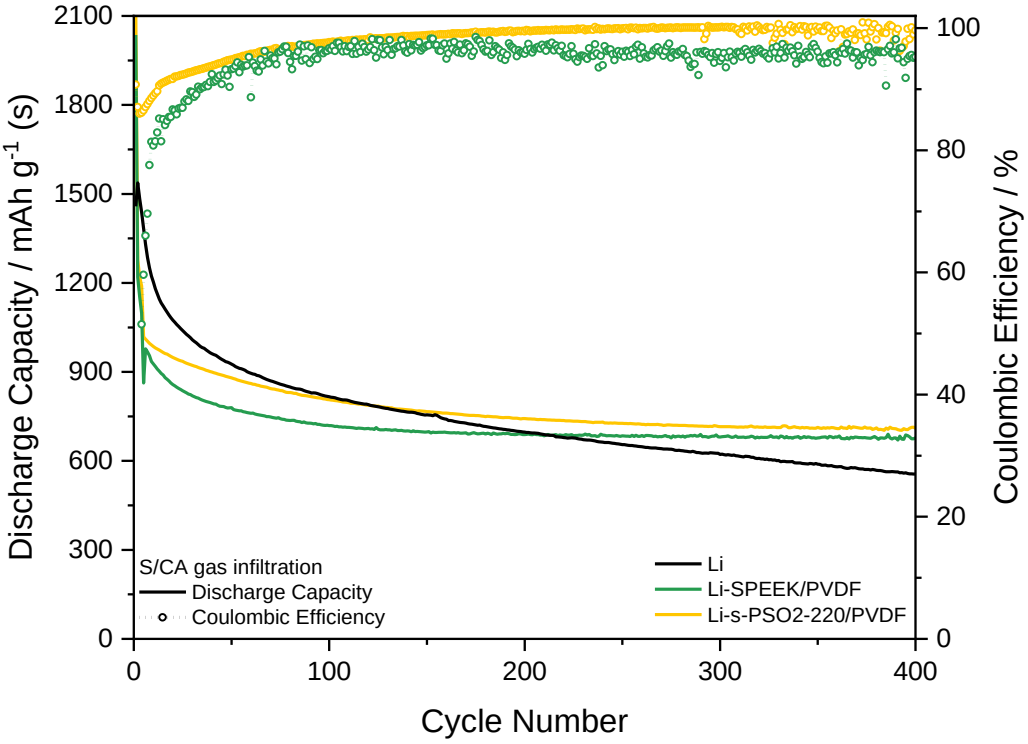

Figure 4.36: Cycling performance of Li-S cells with different artificial SEI and gas infiltrated S/CA cathode at C/3 (electrolyte: 1.0 M LiTFSI DOL/DME, separator: Celgard 2500, sulfur loading: 0.5 $mg \cdot cm^{-2}$).

It has been shown that the s-PSO2-220/PVDF coating results in a high cycle stability. Moreover, the anode could be effectively protected by means of artificial SPEEK/PVDF SEI in previous experiments. These observations are also confirmed with the stable S/CA cathode. Constant coulombic efficiencies of 95% to 100% are achieved proving the almost completely reversible stripping and plating of Li/Li^+ under the artificial SEI. Furthermore, cells with artificial SEI show a constant capacity retention of over 400 cycles and thus a better long-term stability than the Li reference. Due to the very stable cathode, the influence of the artificial SEI only becomes visible with a high number of cycles. The combination of the artificial SPEEK/PVDF and s-PSO2-220/PVDF SEI with an S/CA cathode leads to less parasitic side reactions during cycling the cells. As a result, the active material is received on the anode side as well as on the cathode side and the artificial SEI is not damaged by reactions with sulfur species. This ultimately results in the high cycle stability of the cells of over 400 cycles.

The cycling performance during charge process is illustrated in Figure 4.37.

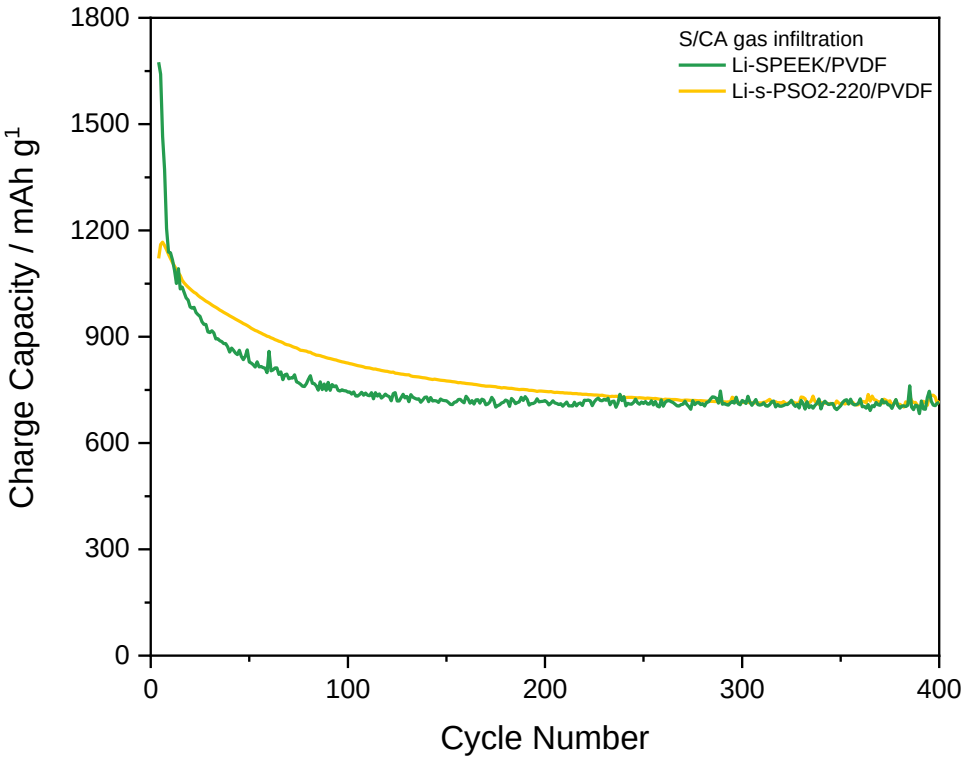

Figure 4.37: Charge Capacity of Li-S cells with different artificial SEI and gas infiltrated S/CA cathode at C/3 (electrolyte: 1.0 M LiTFSI DOL/DME, separator: Celgard 2500, sulfur loading: 0.5 $mg \cdot cm^{-2}$).

Cells with s-PSO2-220/PVDF coating indicated a high capacity retention even upon charge as well. The generally very high initial charge capacity of cells with SPEEK/PVDF SEI could already be observed in connection with S/KB cathodes. It is assumed that this is due to the *in-situ* exchange of H^+ to Li^+ during the initial cycles. In the following a rapid drop in capacity is observed until the capacity subsequently remains constant.

The effectiveness of the anode protection by the artificial SEI was additionally tested combined with a 1 M $LiPF_6$ ethylene carbonate/dimethyl carbonate (EC/DMC) (50:50) electrolyte. Li-S cells without a protected anode can generally not be cycled in this electrolyte in connection with Celgard 2500 separators due to the issue inducted by wetting. Here the complication arises when the excess electrolyte on the anode side react with the anion resulting in the overconsumption of the Li. Figure 4.38 shows the cycling performance during galvanostatic cycling at C/3 of a cell with artificial SEEK/PVDF SEI.

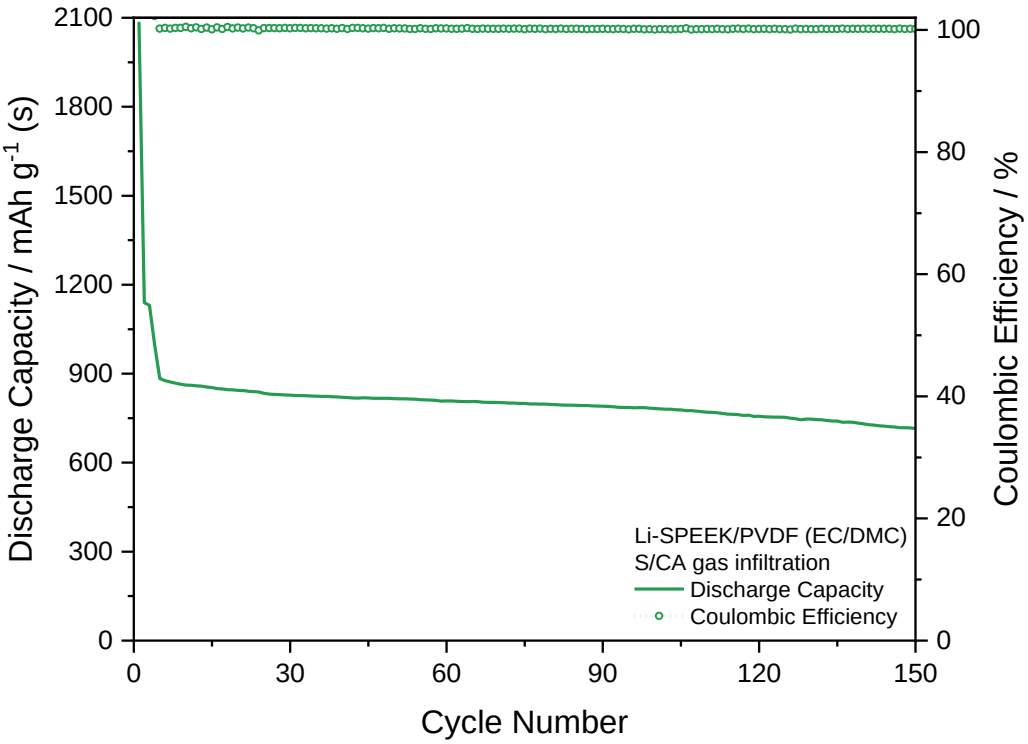

Figure 4.38: Cycling performance of a Li-S cell with artificial SPPEK/PVDF SEI, $LiPF_6$ EC/DMC electrolyte, Celgard 2500 separator and S/CA cathode at C/3.

Stable cycling of the cell over 150 cycles is achieved. The artificial SEI proves a high capacity retention as well as a constant coulombic efficiency of 100% confirming the effectiveness of the artificial SEI on the Li anode. The artificial SEI behaves as the passivation film on the Li suppressing the parasitic reaction. The wettability issue will be eliminated as soon as the discharge process starts facilitating the transport of solvent as well as ions through the separator.

5 Conclusion and outlook

Main goal of this thesis was to design and form *ex-situ* artificial SEI on the metal surface (Li, Mg) stabilizing the anode as well as hindering the dendrite formation and growth. Inherent drawbacks of an *in-situ* formed SEI should be eliminated in order to improve the long-term stability of Me-S batteries.

For this purpose, sulfonate ($-SO_3^-$) based ionomers Aquivion, Nafion, SPEEK and s-PSO2-220 were used as coating components. Moreover, a Mg^{2+} conducting polymeric film made from thermal-cyclized PAN and conductive Mg salt was investigated as Mg anode coating. The organic-based coatings were applied to the metal anode by means of casting-based coating techniques such as spin and dip coating.

Surface morphology of modified Mg anodes were investigated before and after galvanostatic cycling (> 150 cycles) in Mg-S cells using SEM-EDX. It has been shown that the most homogeneous coatings can be formed with Aquivion and PAN. Overall, increased aging of the anodes at the edge and in the middle was observed. Too thin coatings led in some cases to a partial collapse of the artificial SEI during cycling.

The *in-situ* exchange of H^+ ions of the sulfonic acid group with Mg^{2+} ions during galvanostatic cycling was confirmed by FTIR spectroscopy. Typical changes were noticed in the *post-mortem* spectra of the respective Mg anodes.

Galvanostatic cycling with artificial SEI protected anodes have shown that the additional use of a PVDF binder as coating component effectively stabilized the SEI. The coated anodes resulted in stable cycling performances for over 150 cycles at C/10 in Mg-S cells. Especially with homogeneous Aquivion/PVDF and PAN SEI, a significant increase in capacity compared to an uncoated Mg anode was achieved. The discharge capacities after 150 cycles were 200% and 85% higher in comparison to the discharge capacity of the Mg-S reference cell with uncoated anode, respectively. SPEEK, s-PSO2-220 and Nafion-based coatings led initially to higher capacities. The partial collapse of the artificial SEI, however, led to an adjustment to the values of the Mg-S reference cell with uncoated anode with increasing number of cycles.

Since the artificial SEI led to higher overpotentials in symmetrical Mg-Mg cells, the intrinsic processes at the anode/electrolyte interface were analyzed using EIS in Mg-Mg and Mg-S cells.

During polarization at different current densities, two overall processes occurred with the uncoated Mg anode: a fast CT process (HF region) and a slower process (MF region) through the formation of an *in-situ* SEI. Homogenous coated anodes showed the formation of another process in the LF region, which is assigned to the artificial SEI. A process in the MF region only developed with an increasing number of cycles, indicating a partial collapse of the artificial SEI. This allows an *in-situ* SEI to be formed on the locally unprotected Mg anode. In addition, an adsorption layer formed on the uncoated anode during OCV. Similar time constants for the adsorption and the diffusion through the artificial SEI led to an overlay of the impedance response in the LF region.

EIS in Mg-S full cells was carried out during OCV and the subsequent first ten discharge/charge cycles. Two processes were present in the initial OCV. However, the processes can only be clearly separated into an HF and MF process for the uncoated anode. With an Aquivion/PVDF- or PAN-coated anode the separation of the processes is shown in the subsequent initial discharge/charge cycle.

In order to investigate the influence of the artificial SEI on the cycling performance of Li-S cells, coated anodes along with various cathodes were tested. For this purpose, a simple ball milled S/KB cathode, a melt infiltrated S/KB cathode and a gas infiltrated S/CA cathode were used. Cells with artificial SEI showed overall better coulombic efficiencies compared to Li-S reference cells with uncoated anodes. However, the perfluorinated ionomers Aquivion and Nafion reacted with Li metal. Better cycling performance in terms of capacity retention and coulombic efficiency were achieved with hydrocarbon-based ionomers s-PSO2-220 and SPEEK. A higher polarity compared to Nafion and Aquivion also resulted in higher IEC numbers, resulting in an additional beneficial effect. The combination of a stable S/CA cathode with an artificial SEI based on a SPEEK or s-PSO2-220 ionomer was proved to be particularly promising. Thus, Li-S cells could be cycled for over 400 cycles at C/3 with a high capacity retention and coulombic efficiencies almost 100%. Furthermore, the implementation of an artificial SPEEK/PVDF SEI enabled the cyclability in a $LiPF_6$ EC/DMC electrolyte along with a Celgard separator. It must be noted that Li-S cells without artificial SEI cannot be cycled using this specific combination of this electrolyte and separator.

In conclusion, the implementation of an artificial SEI in Li-S and Mg-S cells led to an improved cycling performance. Therefore, especially in Mg-S batteries, it is desirable in the future to use a stable artificial SEI to enable the use of carbonate- or nitrile-based electrolyte systems. EIS

measurements were only recorded at room temperature so far. In order to better understand the intrinsic processes at the anode/electrolyte interface, future measurements at different temperatures are important. Measurements down to a low frequency range of < 100 mHz offer an additional possibility in order to be able to better assess the occurring LF process.

In the case of Li-S cells, it is desirable in the future to transfer functioning artificial SEI concepts from the lab-cell level to pouch cell technology, where inhomogeneity and surface passivation of Li appears to be a more challenging issue.

6 References

[1] S.-H. Chung, A. Manthiram, *Adv. Mater.* **2019**, *31*, e1901125

[2] R. Fang, S. Zhao, Z. Sun, D.-W. Wang, H.-M. Cheng, F. Li, *Adv. Mater* **2017**, *29*

[3] Z. Zhao-Karger, M. Fichtner, *Front. Chem.* **2018**, *6*, 656

[4] X. Zhao, G. Cheruvally, C. Kim, K.-K. Cho, H.-J. Ahn, K.-W. Kim, J.-H. Ahn, *J. Electrochem. Sci. Technol* **2016**, *7*, 97

[5] R. Mohtadi, F. Mizuno, *Beilstein J. Nanotechnol.* **2014**, *5*, 1291

[6] H. Zhao, N. Deng, J. Yan, W. Kang, J. Ju, Y. Ruan, X. Wang, X. Zhuang, Q. Li, B. Cheng, *Chem. Eng. J.* **2018**, *347*, 343

[7] J. Luo, R.-C. Lee, J.-T. Jin, Y.-T. Weng, C.-C. Fang, N.-L. Wu, *Chem. Commun.* **2017**, *53*, 963

[8] C. Hänsel, D. Kundu, *ACS Omega* **2019**, *4*, 2684

[9] S.-B. Son, T. Gao, S. P. Harvey, K. X. Steirer, A. Stokes, A. Norman, C. Wang, A. Cresce, K. Xu, C. Ban, *Nat. Chem.* **2018**, *10*, 532

[10] P. Birke, M. Schiemann, *Akkumulatoren. Vergangenheit, Gegenwart und Zukunft elektrochemischer Energiespeicher*, Utz, München, **2013**

[11] W. Schmickler, *Grundlagen der Elektrochemie*, Vieweg, Braunschweig, Wiesbaden, **1996**

[12] T. Reddy, *Linden's Handbook of Batteries, Fourth Edition*, McGraw-Hill, **2011**

[13] H. Rubenbauer, S. Henninger, *J. Energy Storage* **2017**, *12*, 87

[14] L. Kong, C. Yan, J.-Q. Huang, M.-Q. Zhao, M.-M. Titirici, R. Xiang, Q. Zhang, *Energy Environ. Mater.* **2018**, *1*, 100

[15] H. Zhou, S. Yu, H. Liu, P. Liu, *J. Power Sources* **2020**, *450*, 227632

[16] J. Muldoon, C. B. Bucur, T. Gregory, *Chem. Rev.* **2014**, *114*, 11683

[17] G. Rong, X. Zhang, W. Zhao, Y. Qiu, M. Liu, F. Ye, Y. Xu, J. Chen, Y. Hou, W. Li et al., *Adv. Mater.* **2017**, *29*

[18] T. Tao, S. Lu, Y. Fan, W. Lei, S. Huang, Y. Chen, *Adv. Mater.* **2017**, *29*

[19] K. Fan, Y. Tian, X. Zhang, J. Tan, *J. Electroanal. Chem.* **2016**, *760*, 80

[20] A. Robba, A. Vizintin, J. Bitenc, G. Mali, I. Arčon, M. Kavčič, M. Žitnik, K. Bučar, G. Aquilanti, C. Martineau-Corcos et al., *Chem. Mater.* **2017**, *29*, 9555

[21] M. Jäckle, A. Groß, *J. Chem. Phys.* **2014**, *141*, 174710

[22] P. Bonnick, J. Muldoon, *Adv. Funct. Mater.* **2020**, 1910510

[23] J. Eaves-Rathert, K. Moyer, M. Zohair, C. L. Pint, *Joule* **2020**, *4*, 1324

[24] P. Wang, M. R. Buchmeiser, *Adv. Funct. Mater.* **2019**, *29*, 1905248

[25] B. Sievert, J. Häcker, F. Bienen, N. Wagner, K. A. Friedrich, *ECS Trans.* **2017**, *77*, 413

[26] Y. Wang, E. Sahadeo, G. Rubloff, C.-F. Lin, S. B. Lee, *J. Mater Sci* **2019**, *54*, 3671

[27] Y. Hu, W. Chen, T. Lei, Y. Jiao, J. Huang, A. Hu, C. Gong, C. Yan, X. Wang, J. Xiong, *Adv. Energy Mater.* **2020**, *1*, 2000082

[28] Q. Pang, X. Liang, C. Y. Kwok, J. Kulisch, L. F. Nazar, *Adv. Energy Mater.* **2017**, *7*, 1601630

[29] R. Mukkabla, M. R. Buchmeiser, *J. Mater. Chem. A* **2020**, *8*, 5379

[30] Z. Zhao-Karger, X. Zhao, Di Wang, T. Diemant, R. J. Behm, M. Fichtner, *Adv. Energy Mater.* **2015**, *5*, 1401155

[31] E. Quartarone, P. Mustarelli, *ECS Trans.* **2020**, *167*, 50508

[32] J. Gao, M. A. Lowe, Y. Kiya, H. D. Abruña, *J. Phys. Chem. C* **2011**, *115*, 25132

[33] S. Warneke, *Neue Elektrolyte für Lithium-basierte Zellsysteme*, Universitätsbibliothek der Universität Stuttgart, Stuttgart, **2018**

[34] X. Wang, Y. Qian, L. Wang, H. Yang, H. Li, Y. Zhao, T. Liu, *Adv. Funct. Mater.* **2019**, *29*, 1902929

[35] Z. Zhao-Karger, M. E. Gil Bardaji, O. Fuhr, M. Fichtner, *J. Mater. Chem. A* **2017**, *5*, 10815

[36] Z. Zhao-Karger, R. Liu, W. Dai, Z. Li, T. Diemant, B. P. Vinayan, C. Bonatto Minella, X. Yu, A. Manthiram, R. J. Behm et al., *ACS Energy Lett.* **2018**, *3*, 2005

[37] R. Korthauer (Hrsg.) *Handbuch Lithium-Ionen-Batterien*, Springer Vieweg, Berlin, Heidelberg, **2013**

[38] G. Zhou, L. Li, D.-W. Wang, X.-Y. Shan, S. Pei, F. Li, H.-M. Cheng, *Adv. Mater.* **2015**, *27*, 641

[39] G. Li, S. Wang, Y. Zhang, M. Li, Z. Chen, J. Lu, *Adv. Mater.* **2018**, *30*, e1705590

[40] G. Bieker, D. Diddens, M. Kolek, O. Borodin, M. Winter, P. Bieker, K. Jalkanen, *J. Phys. Chem. C* **2018**, *122*, 21770

[41] M. Wild, L. O'Neill, T. Zhang, R. Purkayastha, G. Minton, M. Marinescu, G. J. Offer, *Energy Environ. Sci.* **2015**, *8*, 3477

[42] R. Attias, M. Salama, B. Hirsch, Y. Goffer, D. Aurbach, *Joule* **2019**, *3*, 27

[43] X. Yu, A. Manthiram, *Acc. Chem. Res.* **2017**, *50*, 2653

[44] E. Markevich, G. Salitra, A. Rosenman, Y. Talyosef, F. Chesneau, D. Aurbach, *J. Mater. Chem. A* **2015**, *3*, 19873

[45] L. E. Camacho-Forero, T. W. Smith, S. Bertolini, P. B. Balbuena, *J. Chem. Phys.* **2015**, *119*, 26828

[46] Y. Wang, C.-F. Lin, J. Rao, K. Gaskell, G. Rubloff, S. B. Lee, *ACS App. Mater. Interfaces* **2018**, *10*, 24554

[47] A. Kopač Lautar, J. Bitenc, T. Rejec, R. Dominko, J.-S. Filhol, M.-L. Doublet, *J. AM Chem. Soc.* **2020**, *142*, 5146

[48] M. Salama, R. Attias, B. Hirsch, R. Yemini, Y. Gofer, M. Noked, D. Aurbach, *ACS Appl. Mater. Interfaces* **2018**, *10*, 36910

[49] E. M. Erickson, E. Markevich, G. Salitra, D. Sharon, D. Hirshberg, E. de La Llave, I. Shterenberg, A. Rosenman, A. Frimer, D. Aurbach, *J. Electrochem. Soc.* **2015**, *162*, A2424-A2438

[50] X.-C. Hu, Y. Shi, S.-Y. Lang, X. Zhang, L. Gu, Y.-G. Guo, R. Wen, L.-J. Wan, *Nano Energy* **2018**, *49*, 453

[51] T. Gao, S. Hou, K. Huynh, F. Wang, N. Eidson, X. Fan, F. Han, C. Luo, M. Mao, X. Li et al., *ACS Appl. Mater. Interfaces* **2018**, *10*, 14767

[52] X. Li, T. Gao, F. Han, Z. Ma, X. Fan, S. Hou, N. Eidson, W. Li, C. Wang, *Adv. Energy Mater.* **2018**, *8*, 1701728

[53] H.-K. Jing, L.-L. Kong, S. Liu, G.-R. Li, X.-P. Gao, *J. Mater. Chem. A* **2015**, *3*, 12213.

[54] L. Wang, Q. Wang, W. Jia, S. Chen, P. Gao, J. Li, *J. Power Sources* **2017**, *342*, 175

[55] J. Qian, W. Xu, P. Bhattacharya, M. Engelhard, W. A. Henderson, Y. Zhang, J.-G. Zhang, *Nano Energy* **2015**, *15*, 135

[56] H. Liu, H. Zhou, B.-S. Lee, X. Xing, M. Gonzalez, P. Liu, *ACS Appl. Mater. Interfaces* **2017**, *9*, 30635

[57] H. Chen, A. Pei, D. Lin, J. Xie, A. Yang, J. Xu, K. Lin, J. Wang, H. Wang, F. Shi et al., *Adv. Energy Mater.* **2019**, *9*, 1900858

[58] H.-D. Lim, H.-K. Lim, X. Xing, B.-S. Lee, H. Liu, C. Coaty, H. Kim, P. Liu, *Adv. Mater. Interfaces* **2018**, *5*, 1701328

[59] I. Bauer, S. Thieme, J. Brückner, H. Althues, S. Kaskel, *J. Power Sources* **2014**, *251*, 417

[60] R. Mruk, "Ionomere zum Aufbau funktioneller Oberflächen", zu finden unter http://ArchiMeD.uni-mainz.de/pub/2003/0153/diss.pdf. (27 March 2020; 04:46 pm)

[61] K. A. Mauritz, R. B. Moore, *Chem. Rev.* **2004**, *104*, 4535

[62] J. Song, H. Lee, M.-J. Choo, J.-K. Park, H.-T. Kim, *Sci. Rep.* **2015**, *5*, 14458

[63] T. Chen, G. Ceder, G. Sai Gautam, P. Canepa, *Front. Chem.* **2019**, *7*, 24

[64] T. Chen, G. Sai Gautam, P. Canepa, *Chem. Mater.* **2019**, *31*, 8087

[65] A. UL-HAMID, *Beginners guide to scanning electron microscopy*, Springer, **2019**

[66] "EDX Grundlagen" zu finden unter https://qd-europe.com/at/en/news/product-application-news-spectrum/ (08 July 2020; 3:56 pm)

[67] "FT IR Grundlagen", zu finden unter https://www.thermofisher.com. (04 April 2020; 02:33 pm)

[68] "FTIR Spectroscopy", zu finden unter https://www.mt.com. (04 April 2020; 02:55 pm)

[69] J. Chastain, *Handbook of X-ray photoelectron spectroscopy*, Phys. Elect., Eden Prairie, Minn., **1995**

[70] M. P. Seah, W. A. Dench, *Surf. Interface Anal.* **1979**, *1*, 2

[71] V. F. Lvovich, *Impedance spectroscopy. Applications to electrochemical and dielectric phenomena*, Wiley, Hoboken, N.J., **2012**

[72] D. U. Sauer, Impedanzspektroskopie - Eine Methode viele Anwendungen, **2006**, 7-11

[73] O. Kanoun, *Impedance Spectroscopy*, De Gruyter, **2019**

[74] D. U. Sauer, Grundlagen der Impedanzspektroskopie für die Charakterisierung von Batterien, **2006**, 74-80

[75] "Assembly of insulation sleeve", zu finden unter https://el-cell.com/pat-series/the-pat-core-concept. (10 July 2020; 13:32)

[76] "chemical information" zu finden unter https://pubchem.ncbi.nlm.nih.gov/ (01 August 2020; 09:37 am)

[77] Cataldo Franco, *Eur. Chem. Bull*., **2015**.4

[78] M. Holfeder, Salerno Dagmar, E. Buxmann, *Relative Dielektrizitätskonstante von flüssigen und festen Medien*, Endress+Hauser Meßtechnik GmbH+Co., **1999**

[79] P. Kurzweil, O. Dietlmeier, *Elektrochemische Speicher*. Springer, **2015**

[80] "XPS data" zu finden unter https://srdata.nist.gov/xps (15 August 2020; 8:20 am)

[81] A. Münchinger, K.-D. Kreuer, *J. Membrane Sci.* **2019**, *592*, 117372

[82] "Nafion" zu finden unter https://www.fuelcellstore.com (15 August 2020; 15:48 pm)

[83] Z. Jin, K. Xie, X. Hong, Z. Hu, X. Liu, *J.Power Sources* **2012**, *218*, 163

[84] H. Bai, X. Wang, Y. Zhou, L. Zhang, *Prog. Nat. Sci.* **2012**, *22*, 250

[85] Z. Liang, W. Chen, J. Liu, S. Wang, Z. Zhou, W. Li, G. Sun, Q. Xin, *J. Membrane Sci.* **2004**, *233*, 39

[86] Y.-T. Weng, H.-W. Liu, A. Pei, F. Shi, H. Wang, C.-Y. Lin, S.-S. Huang, L.-Y. Su, J.-P. Hsu, C.-C. Fang et al., *Nat. Commun.* **2019**, *10*, 5824

[87] M. He, R. Guo, G. M. Hobold, H. Gao, B. M. Gallant, *Proc. Natl. Acad. Sci. U.S.A.* **2020**, *117*, 73

[88] J. Häcker, C. Danner, B. Sievert, I. Biswas, Z. Zhao-Karger, N. Wagner, K. A. Friedrich, *Electrochim. Acta* **2020**, *338*, 135787

[89] "EIS of organic coatings" zu finden unter https://www.gamry.com/application-notes/EIS/ (10 September 2020; 10:11 am)

[90] H. Brandstätter, I. Hanzu, M. Wilkening, *Electrochim. Acta* **2016**, *207*, 218

[91] D. Klotz, *Electrochem. Commun.* **2019**, *98*, 58.

[92] R. Dugas, J. D. Forero-Saboya, A. Ponrouch, *Chem. Mater.* **2019**, *31*, 8613

Appendix

EDX analysis

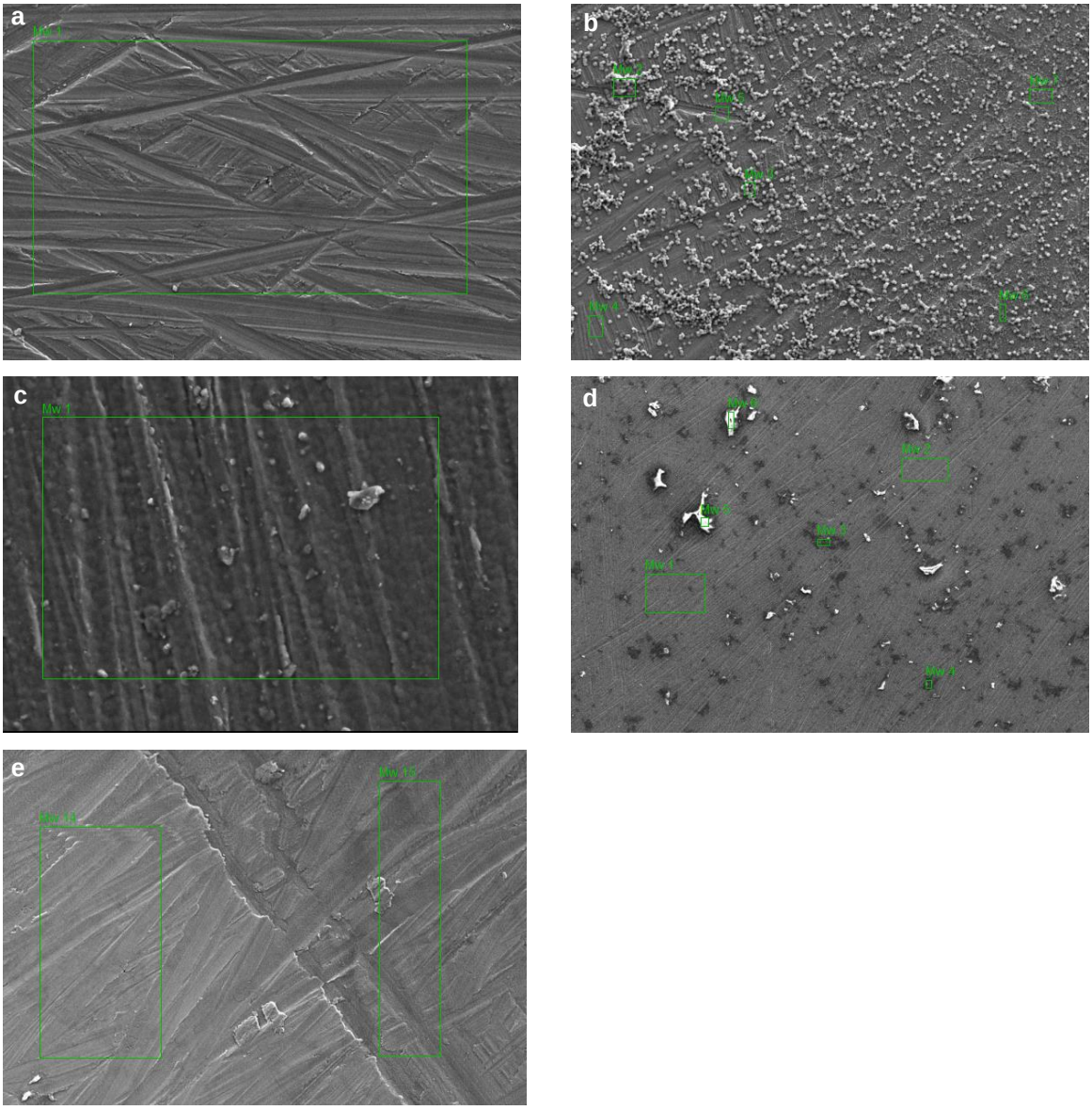

Figure A1: EDX analysis of (a) the pristine Mg anode, (b) Mg-s-PSO2-220/PVDF, (c) Mg-Aquivion/PVDF, (d) Mg-Nafion/PVDF and (e) Mg-SPEEK/PVDF before galvanostatic cycling in Mg-S cells.

Table A1: EDX analysis of the pristine Mg anode, Mg-s-PSO2-220/PVDF, Mg-Aquivion/PVDF, Mg-Nafion/PVDF and Mg-SPEEK/PVDF before galvanostatic cycling in Mg-S cells.

	Percent by weight / %					
Spectrum	**C**	**O**	**F**	**Mg**	**S**	**Cl**
Mg						
M_w 1	2.43	3.26	-	94.31	-	-
Mg-s-PSO2-220						
M_w 2	27.78	9.06	19.43	25.59	6.51	11.63
M_w 3	30.48	10.33	19.52	24.82	6.22	8.64
M_w 4	3.19	1.32	-	95.49	-	-
M_w 5	5.12	5.00	1.03	88.13	-	0.71
M_w 6	8.26	19.79	2.50	64.42	1.48	3.55
M_w 7	11.40	6.22	2.87	74.42	1.78	3.31
Mg-Aquivion/PVDF						
M_w 1	26.33	5.91	23.09	43.97	0.72	
Mg-Nafion/PVDF						
M_w 1	8.99	4.73	4.23	82.06	-	
M_w 2	8.83	3.98	4.45	82.74	-	
M_w 3	22.47	5.86	30.76	39.97	0.94	
M_w 4	22.51	6.79	29.33	40.57	0.81	
M_w 5	22.84	6.84	64.84	2.10	2.26	
M_w 6	23.54	7.06	65.81	1.51	2.08	
Mg-SPEEK/PVDF						
M_w 14	12.95	10.23	2.44	73.73	0.65	-
M_w 15	30.15	7.72	7.49	53.26	1.38	-

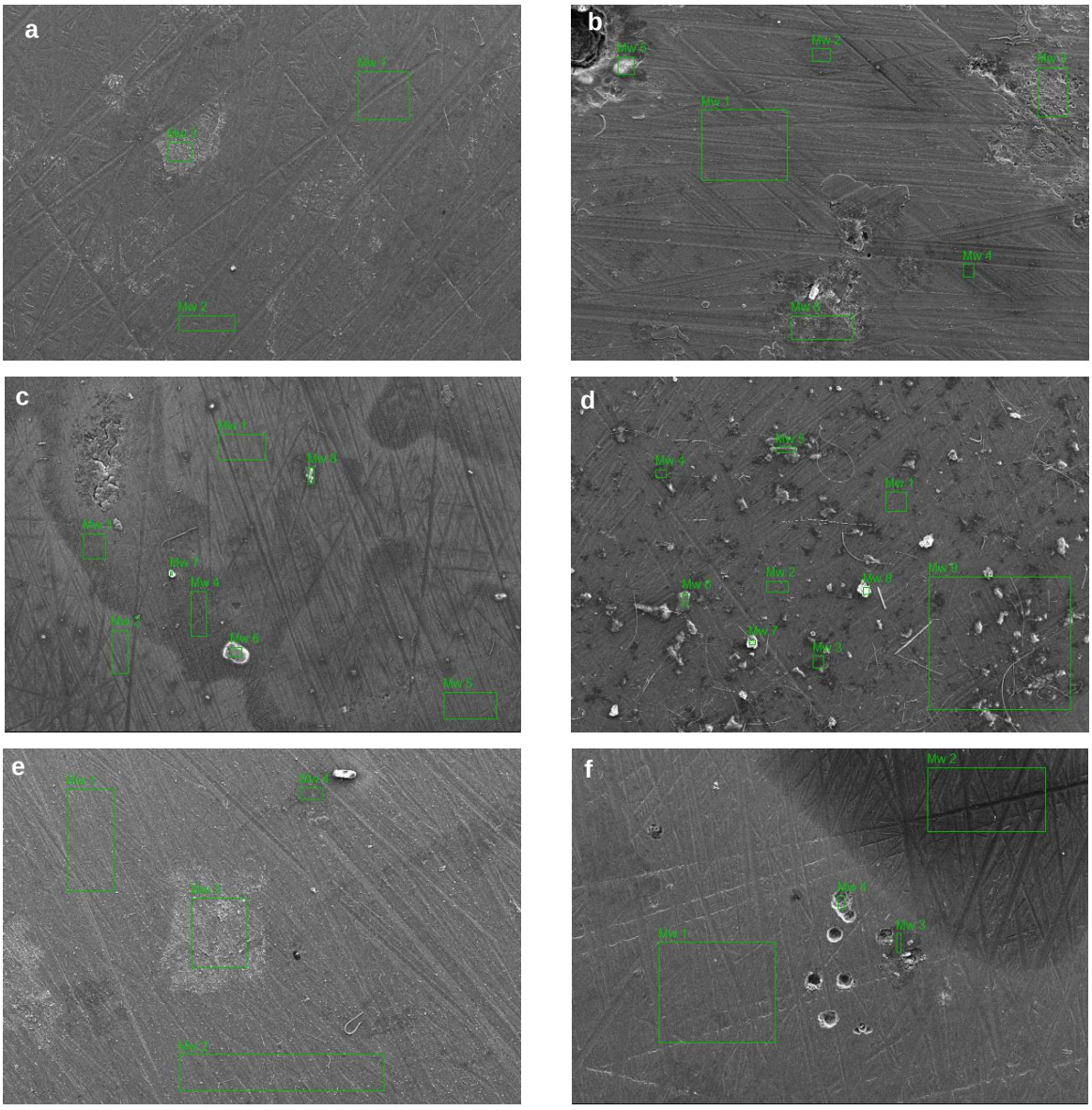

Figure A2: EDX analysis of (a) the uncoated Mg anode, (b) Mg-s-PSO2-220/PVDF, (c) Mg-Aquivion/PVDF, (d) Mg-Nafion/PVDF, (e) Mg-SPEEK/PVDF and (f) Mg-PAN after galvanostatic cycling (> 150 cycles) at C/10 in Mg-S cells.

Table A2: EDX analysis of the uncoated Mg anode, Mg-s-PSO2-220/PVDF, Mg-Aquivion/PVDF, Mg-Nafion/PVDF, Mg-SPEEK/PVDF and Mg-PAN after galvanostatic cycling (> 150 cycles) at C/10 in Mg-S cells.

	Percent by weight / %					
Spectrum	**C**	**O**	**F**	**Mg**	**S**	**N**
Mg						
M_w 1	2.67	2.15	-	95.18	-	-
	2.83	1.62	-	95.55	-	-
	4.30	7.49	0.82	80.88	6.51	-
Mg-s-PSO2-220						
M_w 1	5.07	2.95	1.30	90.67	-	-
M_w 2	8.17	5.32	3.18	83.33	-	-
M_w 3	10.00	10.29	4.21	74.74	0.76	-
M_w 4	11.38	19.9	8.09	59.11	1.50	-
M_w 5	11.19	36.52	10.86	37.96	3.47	-
M_w 6	6.12	25.65	3.19	63.03	2.01	-
Mg-Aquivion/PVDF						
M_w 1	16.17	8.46	10.78	64.58	-	-
M_w 2	14.74	8.12	9.53	67.61	-	-
M_w 3	16.18	13.34	14.34	54.56	0.67	-
M_w 4	16.76	15.95	16.42	49.19	0.71	-
M_w 5	16.28	14.20	13.80	54.16	0.61	-
M_w 6	9.40	5.92	4.35	80.34	-	-
M_w 7	13.61	9.43	10.94	64.92	0.57	-
M_w 8	19.81	22.24	29.19	23.62	5.15	-
Mg-Nafion/PVDF						
M_w 1	13.31	3.26	5.86	77.57	-	-
M_w 2	12.87	3.85	4.83	78.45	-	-

M_w 3	25.20	7.14	23.95	42.87	0.84	-
M_w 4	26.68	7.17	28.01	36.89	1.26	-
M_w 5	25.75	12.3	53.36	6.45	2.30	-
M_w 6	26.31	11.67	54.82	4.93	2.28	-
M_w 7	18.10	35.66	7.71	33.15	5.37	-
M_w 8	16.12	34.36	11.66	33.67	4.19	-
M_w 9	21.00	7.49	16.64	54.86	-	-
Mg-SPEEK/PVDF						
M_w 1	2.28	1.63	-	96.10	-	-
M_w 2	2.63	2.23	-	95.15	-	-
M_w 3	4.26	4.33	-	86.95	4.46	-
M_w 4	2.65	20.37	-	75.33	1.64	-
Mg-PAN						
M_w 1	3.43	3.09	-	93.47	-	-
M_w 2	34.69	4.40	2.41	48.96	1.78	7.76
M_w 3	5.37	35.84	3.28	52.86	2.65	-
M_w 4	4.93	5.32	0.66	89.09	-	-

Post-mortem SEM of the Aquivion/PVDF SEI

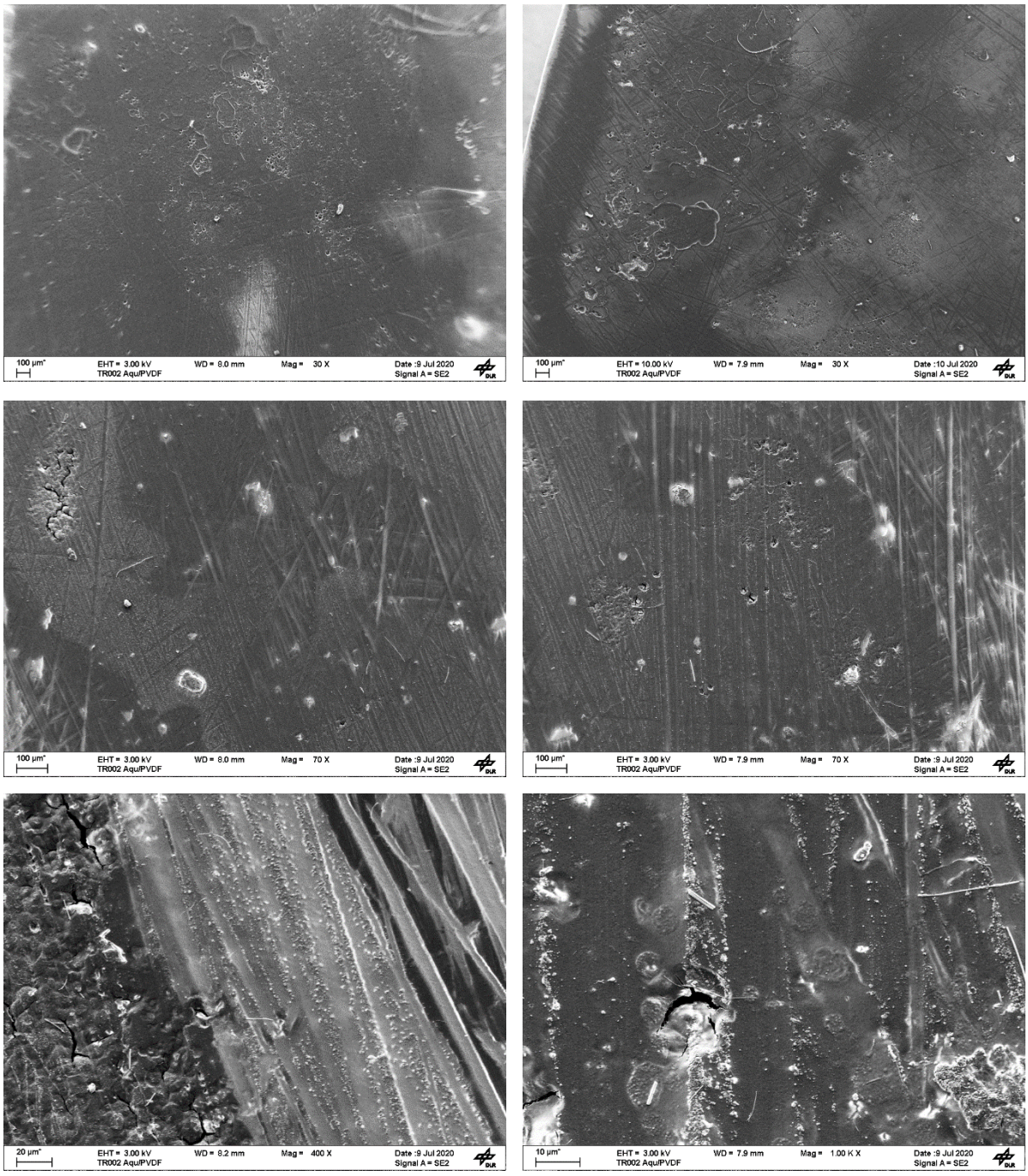

Figure A3: *Post-mortem* (> 150 galvanostatic cycles in Mg-S cell) SEM images of the Mg-Aquivion/PVDF anode at 30x, 70x 400x and 1000x magnification.

FTIR spectra

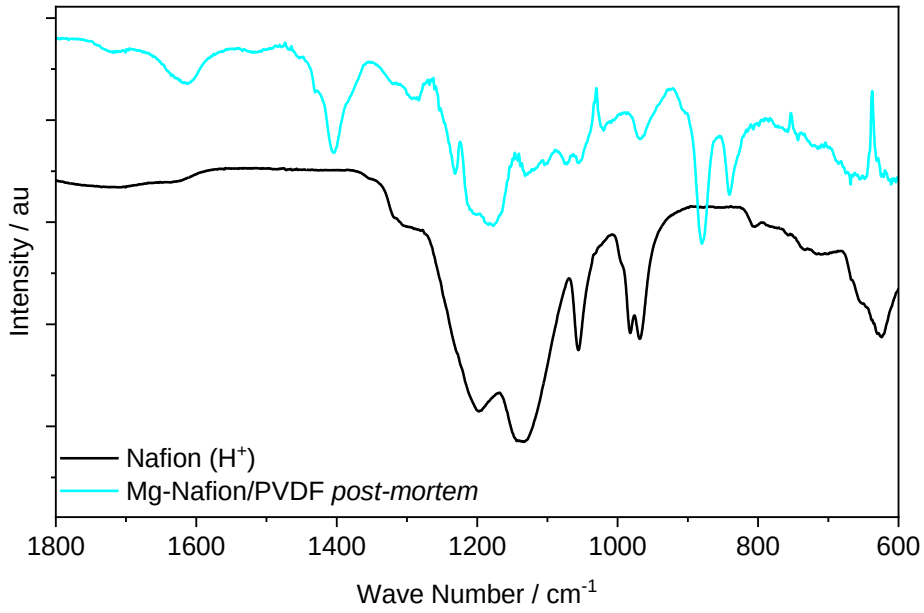

Figure A4: FTIR spectra of Nafion (H^+) before cycling and the corresponding Mg-Nafion/PVDF anode (*post-mortem*).

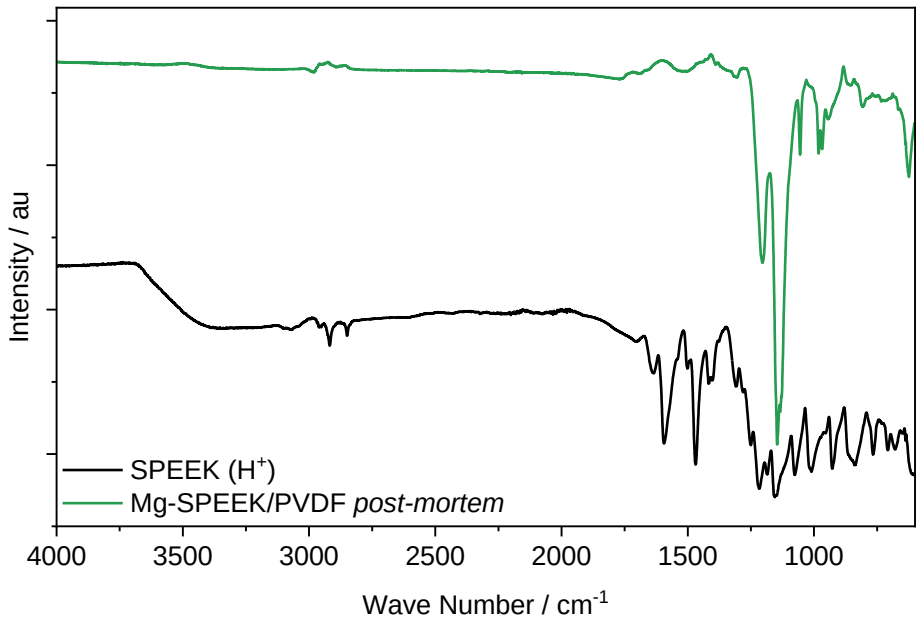

Figure A5: FTIR spectra of SPEEK (H^+) before cycling and the corresponding Mg-SPEEK/PVDF anode (*post-mortem*).

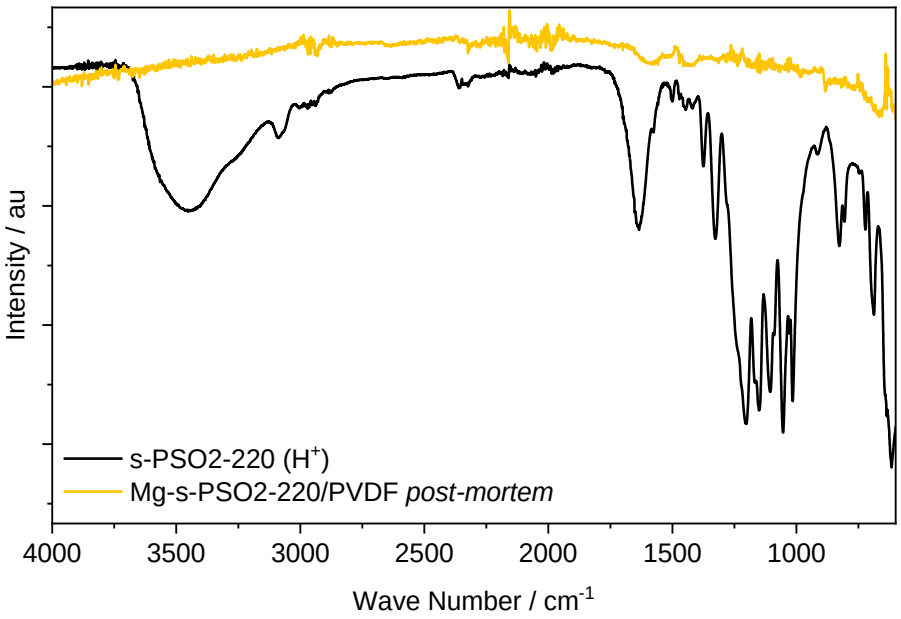

Figure A6: FTIR spectra of s-PSO2-220 (H^+) before cycling and the corresponding Mg-s-PSO2-220/PVDF anode (*post-mortem*).

Bode plots of Mg-Mg cells

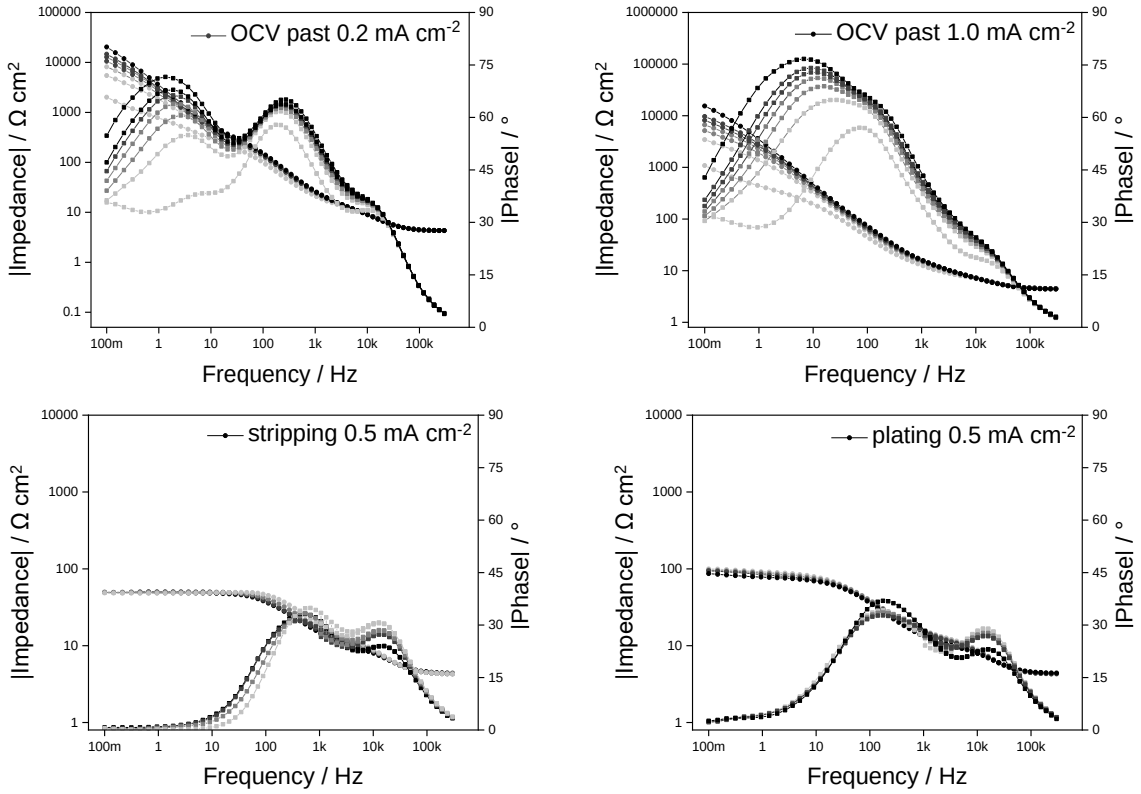

Figure A7: Bode plots of a Mg-Mg cell without coated anode during OCV after ten galvanostatic cycles at 0.2 and 1.0 $mA \cdot cm^{-2}$ as well as Bode plots of stripping and plating at 0.5 $mA \cdot cm^{-2}$.

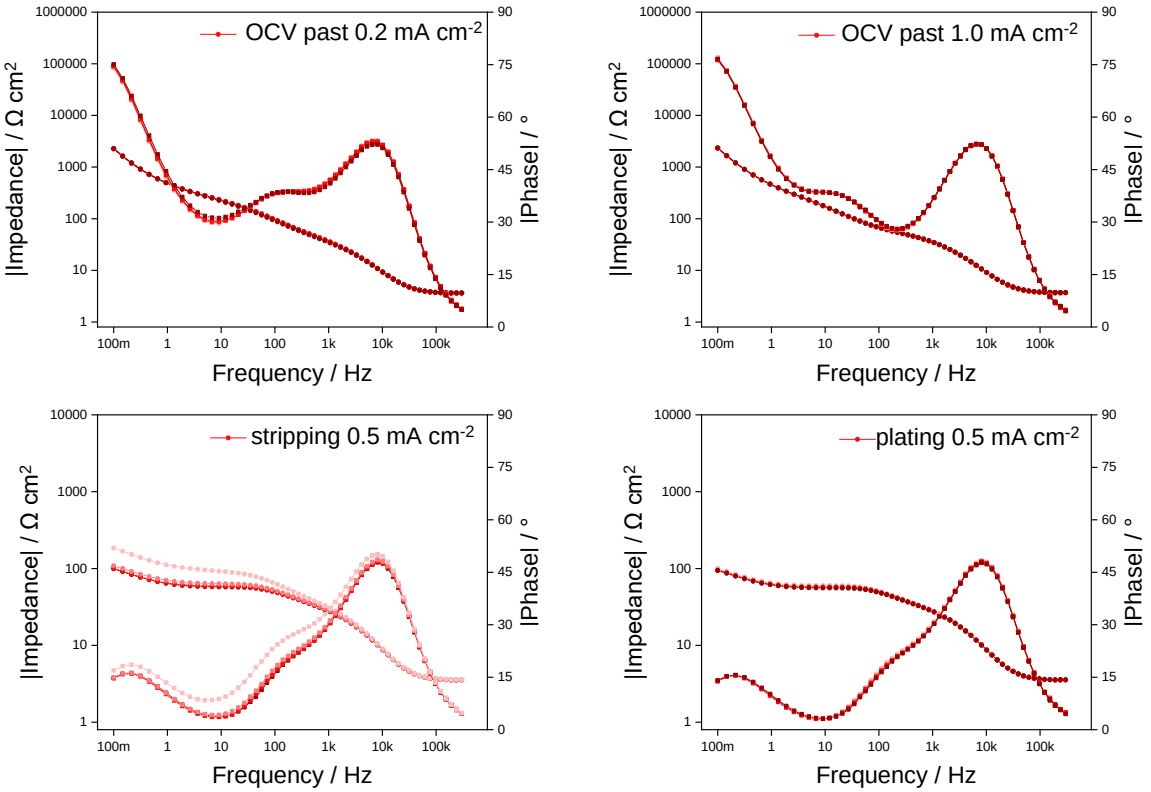

Figure A8: Bode plots of a Mg-Mg cell with artificial Aquivion/PVDF SEI during OCV after ten galvanostatic cycles at 0.2 and 1.0 $mA \cdot cm^{-2}$ as well as Bode plots of stripping and plating at 0.5 $mA \cdot cm^{-2}$.

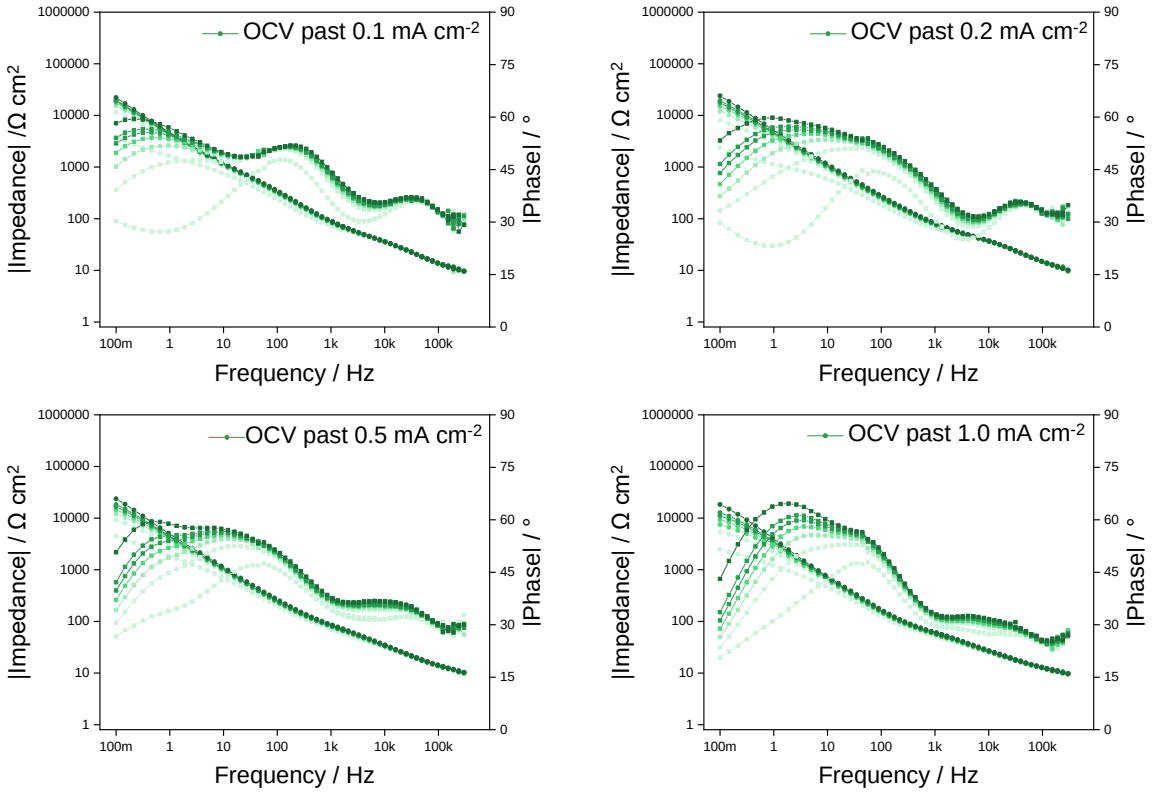

Figure A9: Bode plots of a Mg-Mg cell with artificial SPEEK/PVDF SEI during OCV after ten galvanostatic cycles at 0,1, 0.2, 0.5 and 1.0 $mA \cdot cm^{-2}$.

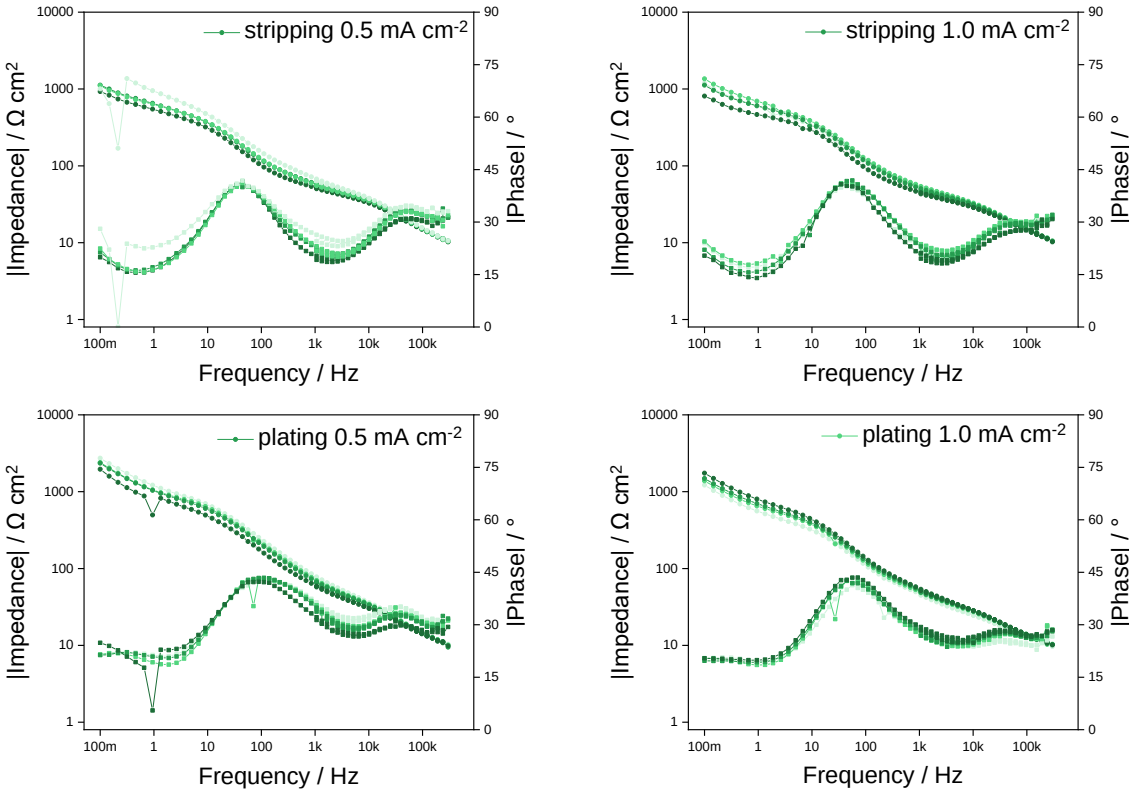

Figure A10: Bode plots of a Mg-Mg cell with artificial SPEEK/PVDF SEI during stripping and plating at 0.5 and 1.0 $mA \cdot cm^{-2}$.

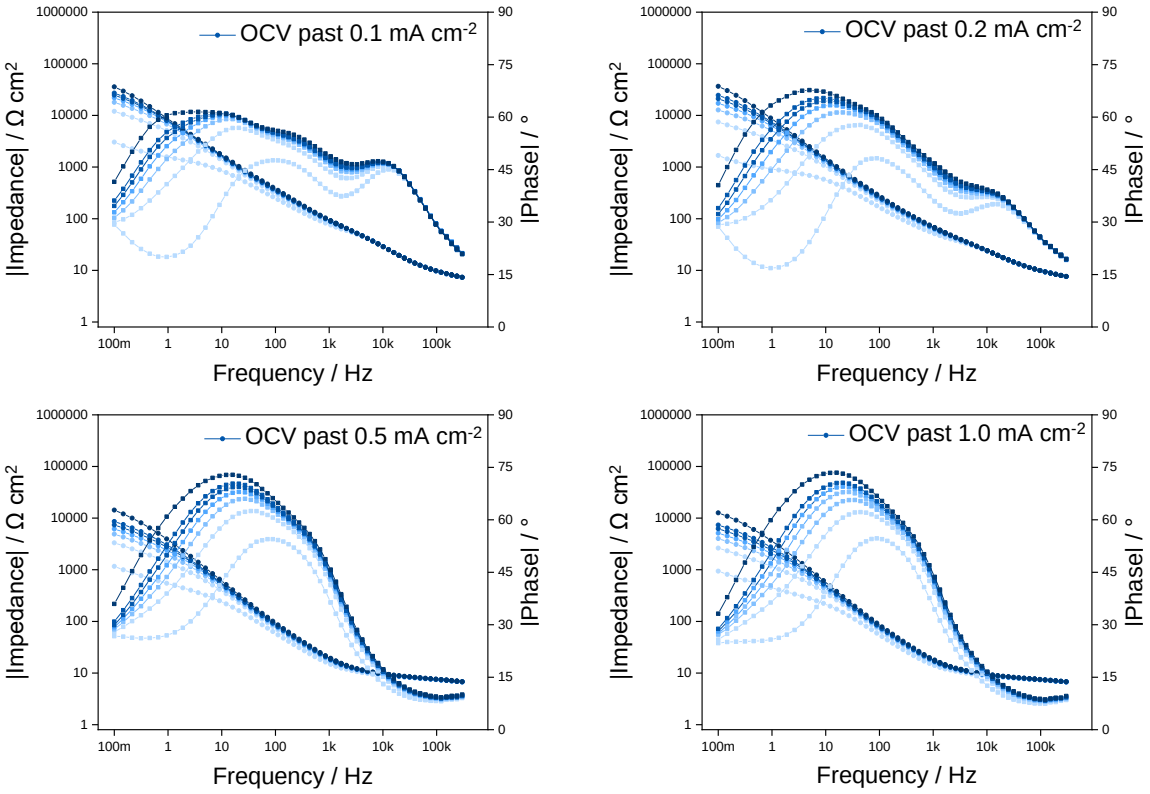

Figure A11: Bode plots of a Mg-Mg cell with artificial PAN SEI during OCV after ten galvanostatic cycles at 0.1, 0.2, 0.5 and 1.0 $mA \cdot cm^{-2}$.

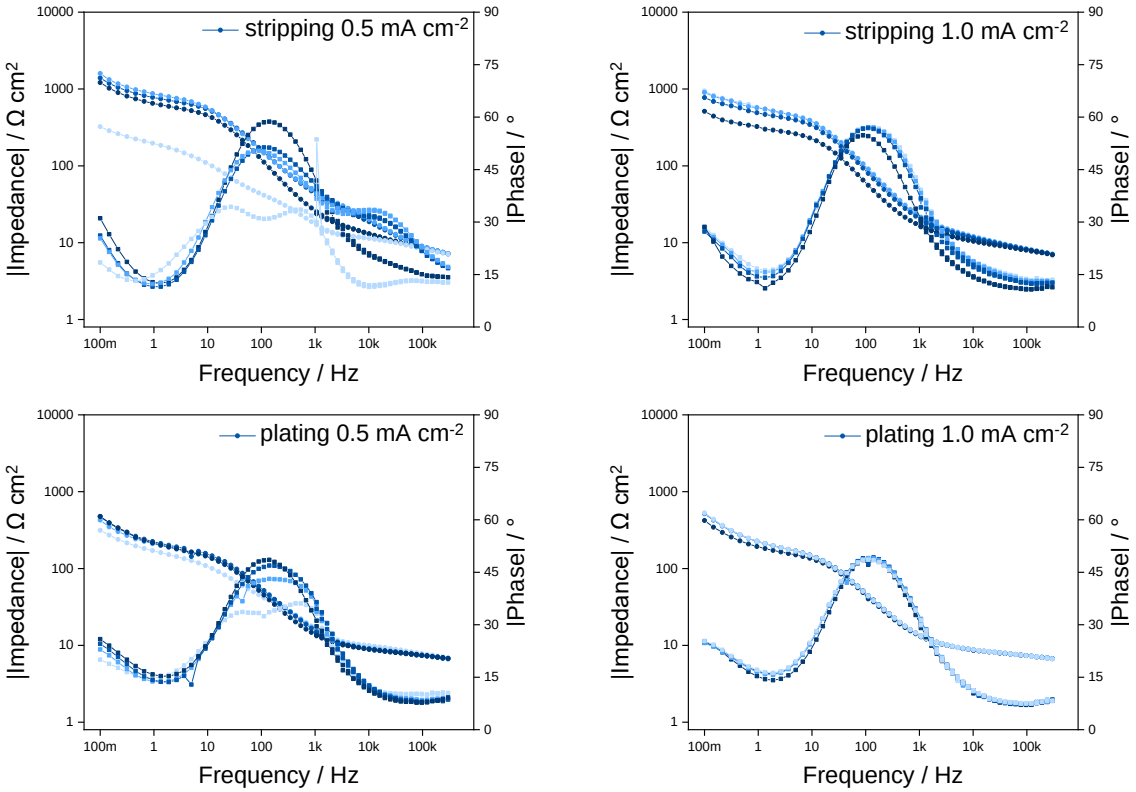

Figure A12: Bode plots of a Mg-Mg cell with artificial PAN SEI during stripping and plating at 0.5 and 1.0 mA · cm^{-2}.

Nyquist plots of Mg-S cells

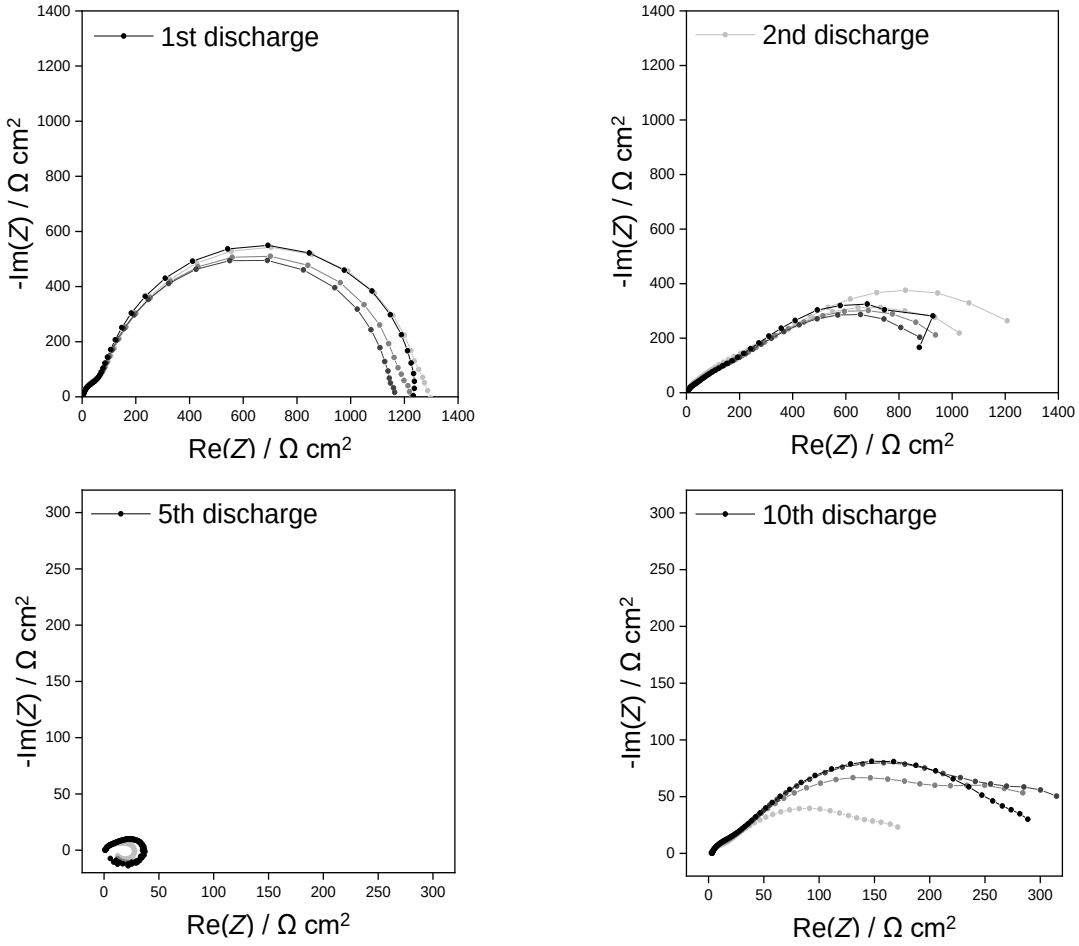

Figure A13: Nyquist plots of a Mg-S cell with uncoated Mg anode during first, second, fifth and tenth discharge cycles at 0.1 $mA \cdot cm^{-2}$.

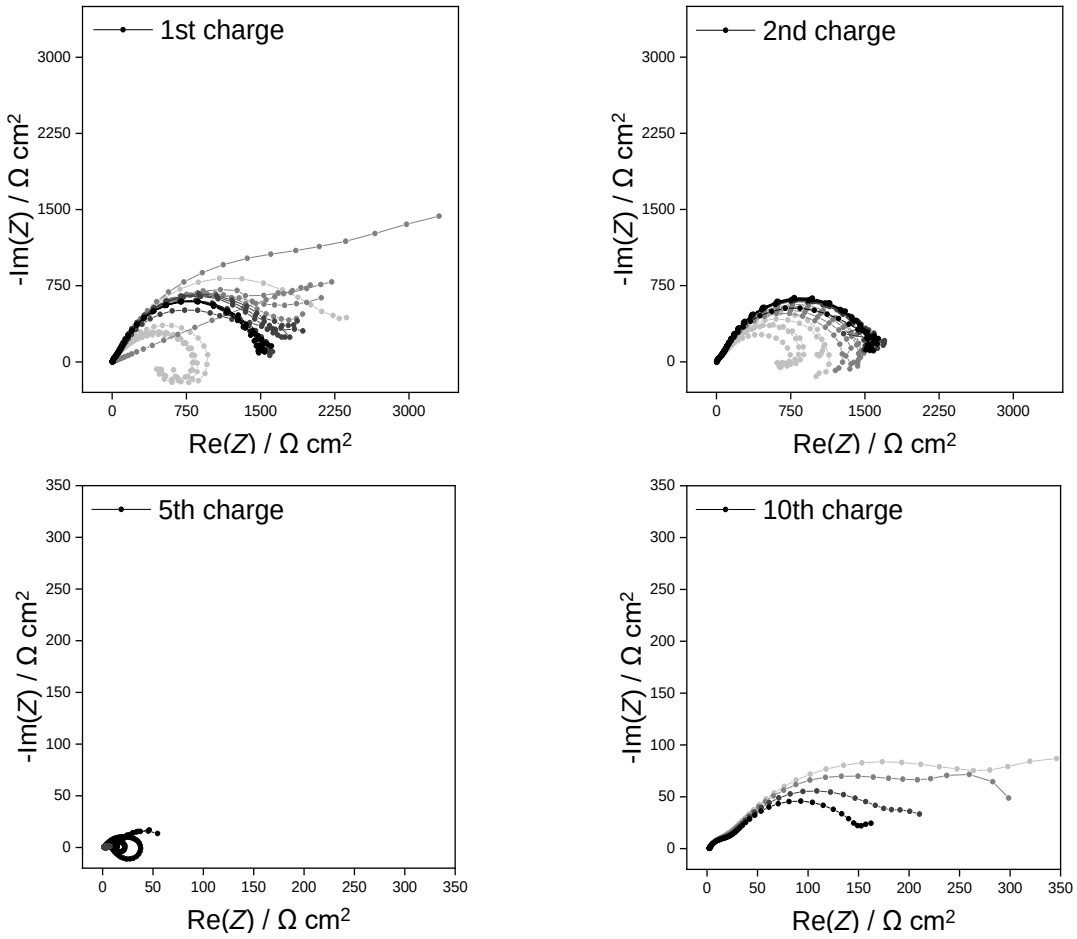

Figure A14: Nyquist plots of a Mg-S cell with uncoated Mg anode during first, second, fifth and tenth charge cycles at 0.1 $mA \cdot cm^{-2}$.

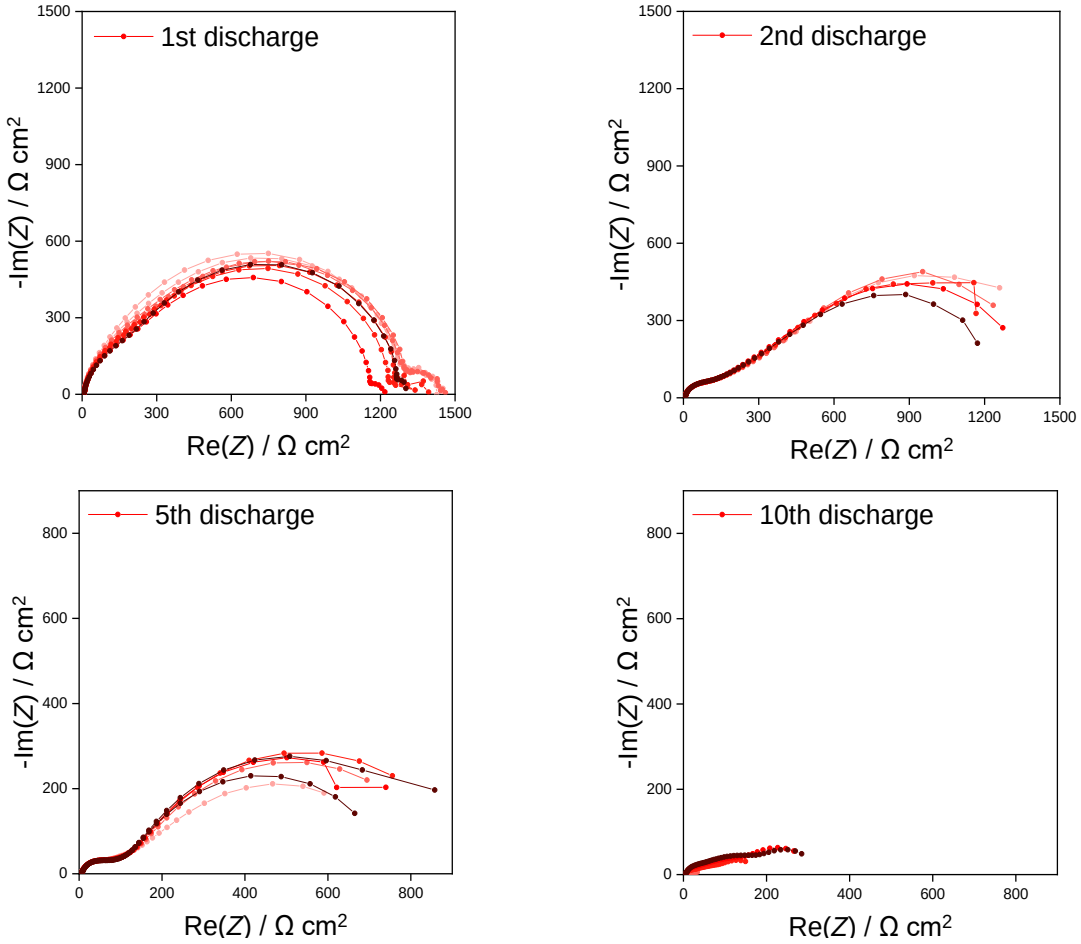

Figure A15: Nyquist plots of a Mg-S cell with artificial Aquivion/PVDF SEI during first, second, fifth and tenth discharge cycles at 0.1 $mA \cdot cm^{-2}$.

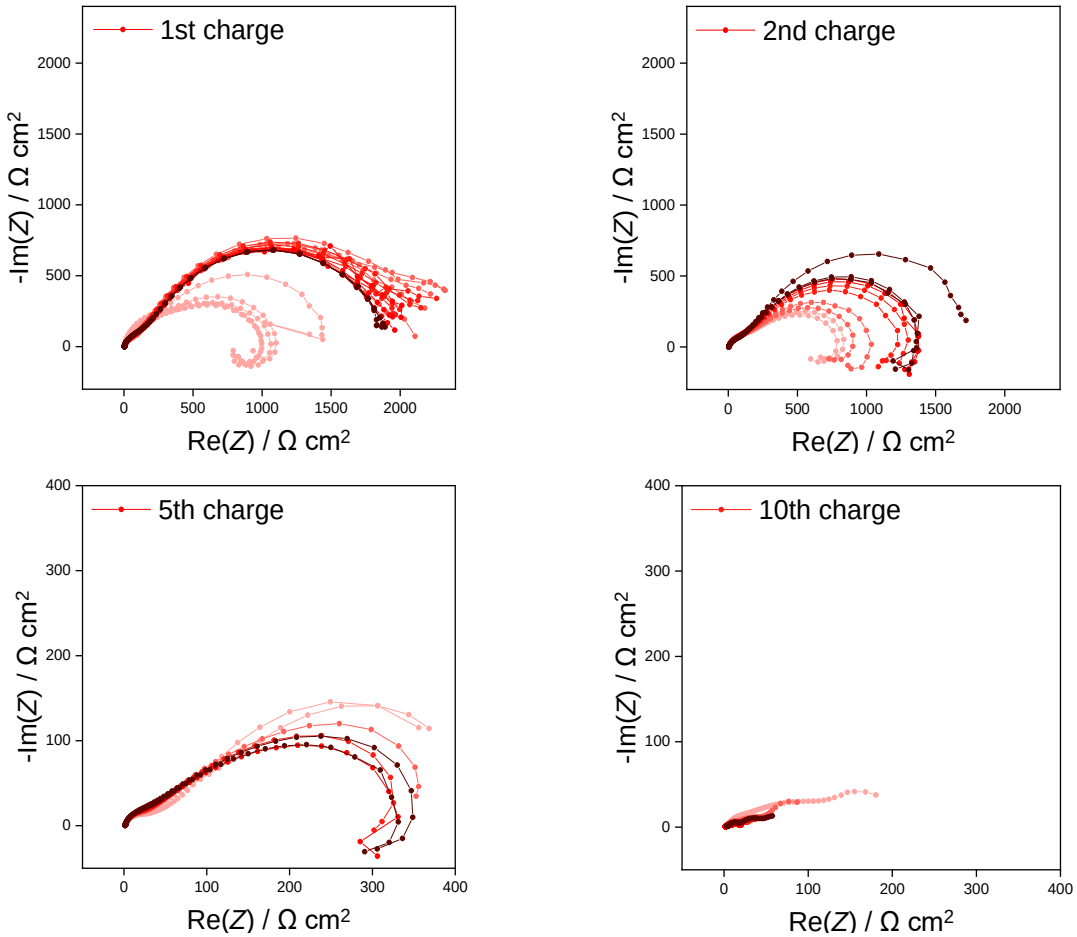

Figure A16: Nyquist plots of a Mg-S cell with artificial Aquivion/PVDF SEI during first, second, fifth and tenth charge cycles at 0.1 $mA \cdot cm^{-2}$.

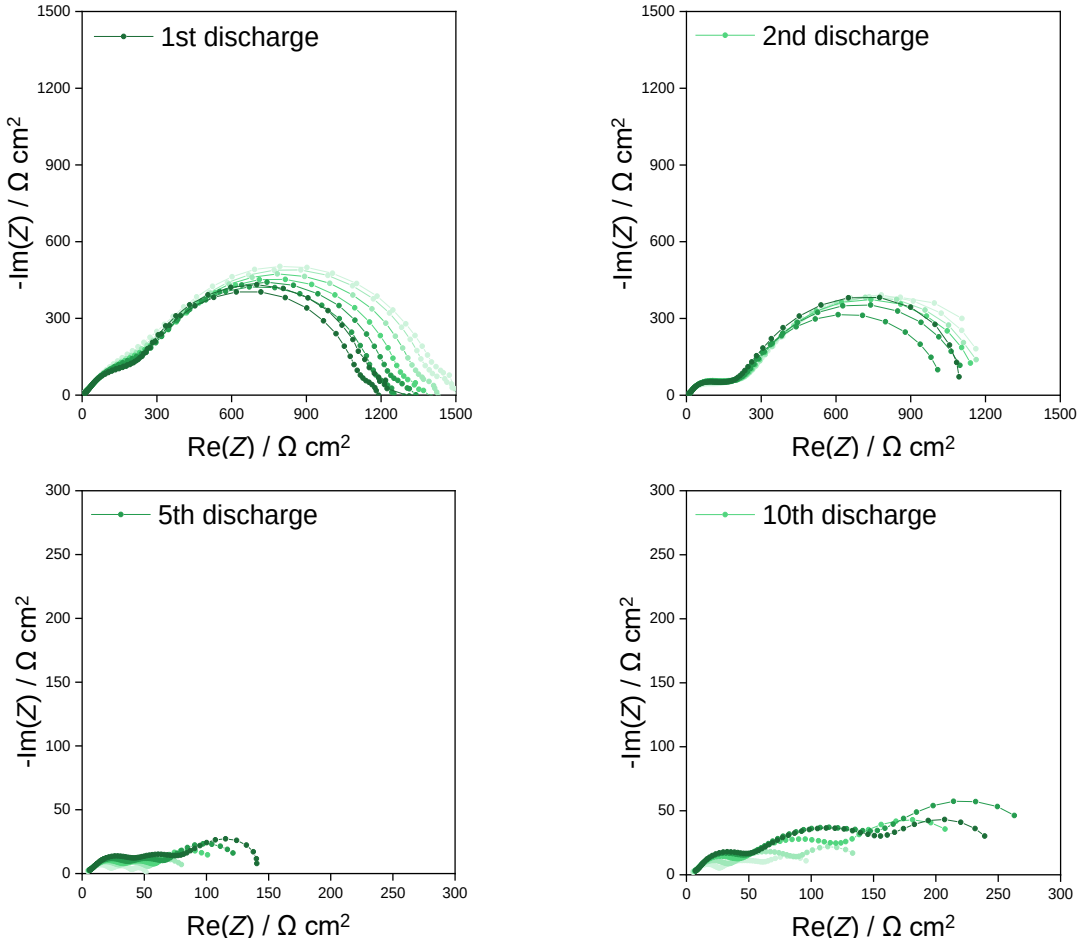

Figure A17: Nyquist plots of a Mg-S cell with artificial SPEEK/PVDF SEI during first, second, fifth and tenth discharge cycles at 0.1 $mA \cdot cm^{-2}$.

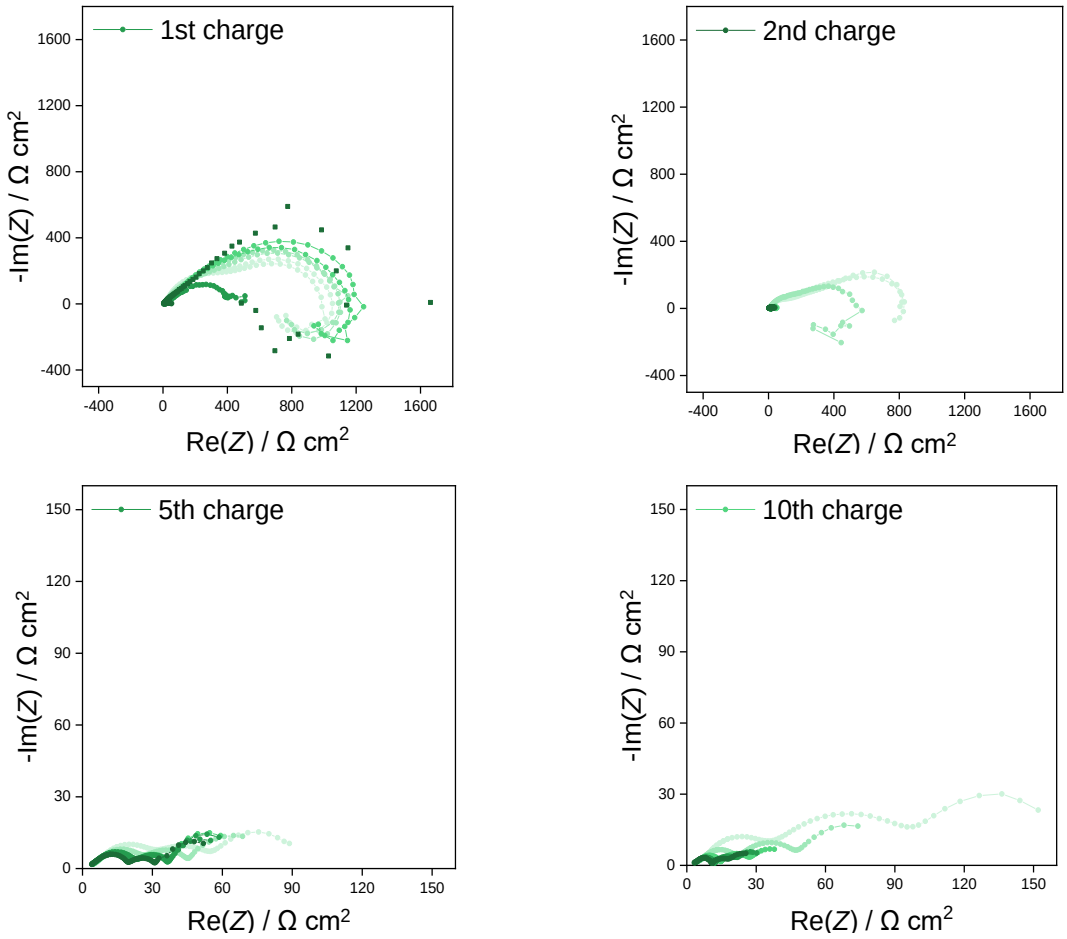

Figure A18: Nyquist plots of a Mg-S cell with artificial SPEEK/PVDF SEI during first, second, fifth and tenth charge cycles at $0.1\ \mathrm{mA \cdot cm^{-2}}$.

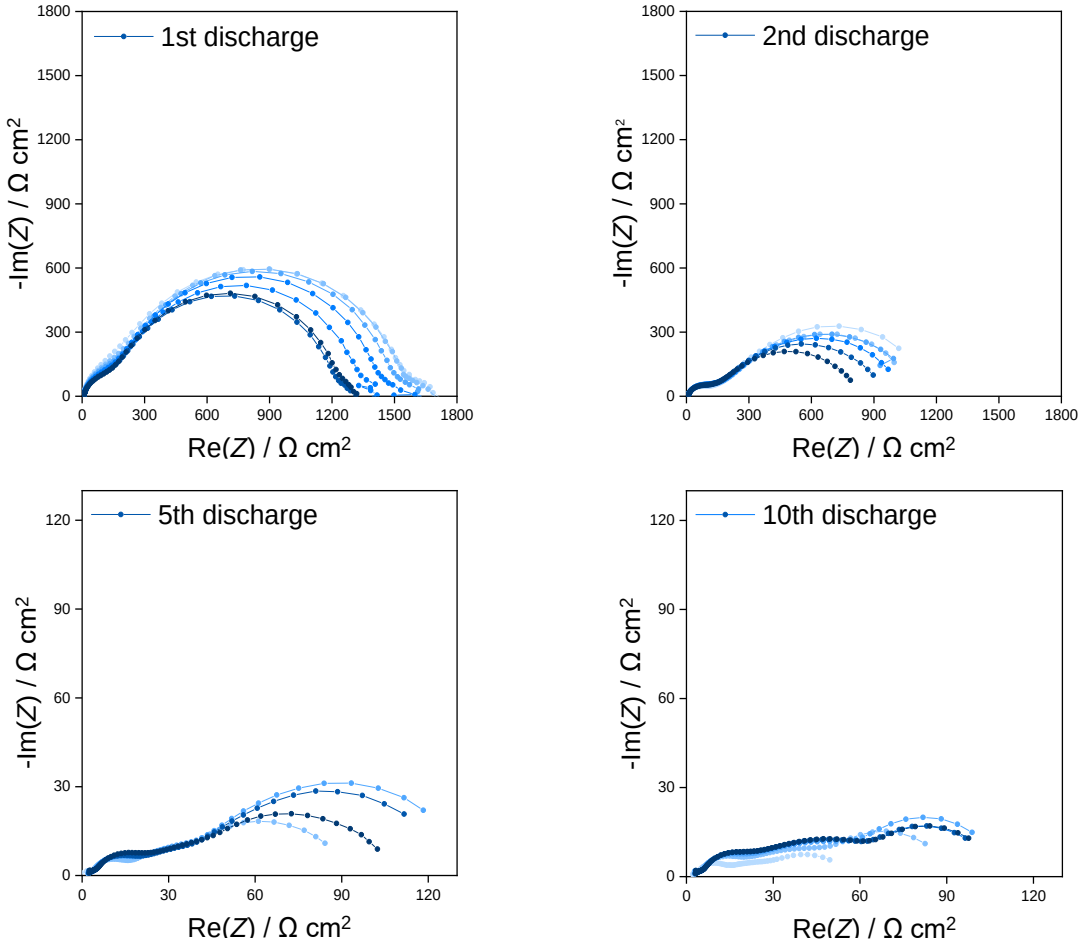

Figure A19: Nyquist plots of a Mg-S cell with artificial PAN SEI during first, second, fifth and tenth discharge cycles at 0.1 $mA \cdot cm^{-2}$.

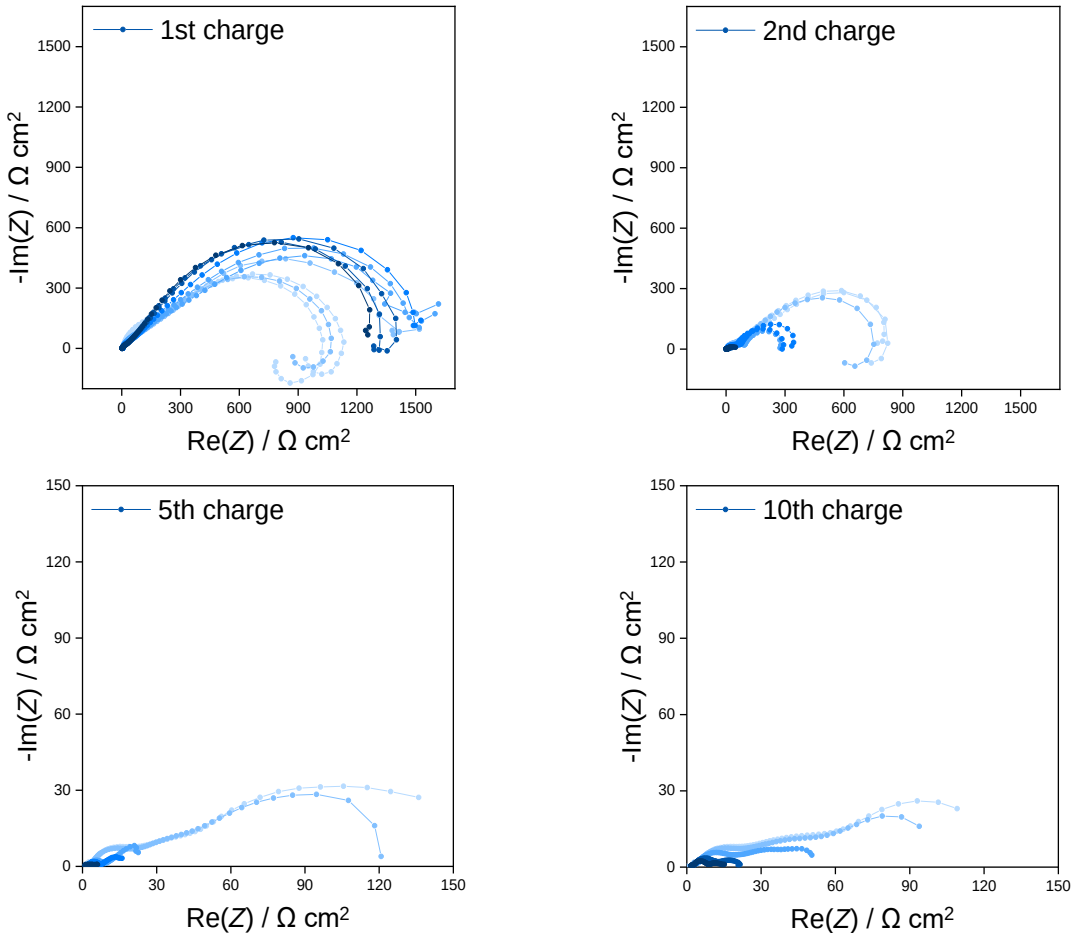

Figure A20: Nyquist plots of a Mg-S cell with artificial PAN SEI during first, second, fifth and tenth charge cycles at 0.1 $mA \cdot cm^{-2}$.

Comparison of the Bode plots of Mg-Mg cells and Mg-S cells

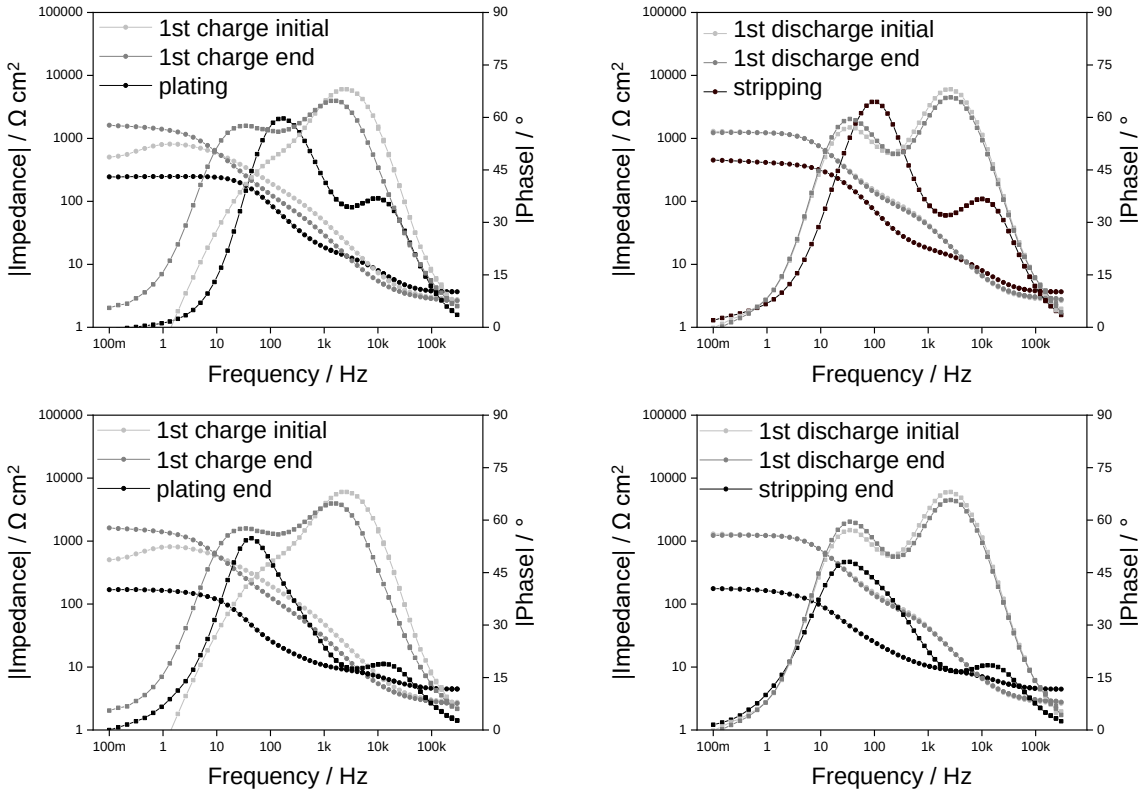

Figure A21: Comparison of the Bode plots of a symmetrical Mg-Mg cell and a Mg-S cell (each without artificial SEI) during stripping and plating at 0.1 $mA \cdot cm^{-2}$ (Mg-Mg) and during the first galvanostatic charge and discharge cycle at 0.1 $mA \cdot cm^{-2}$ (Mg-S).

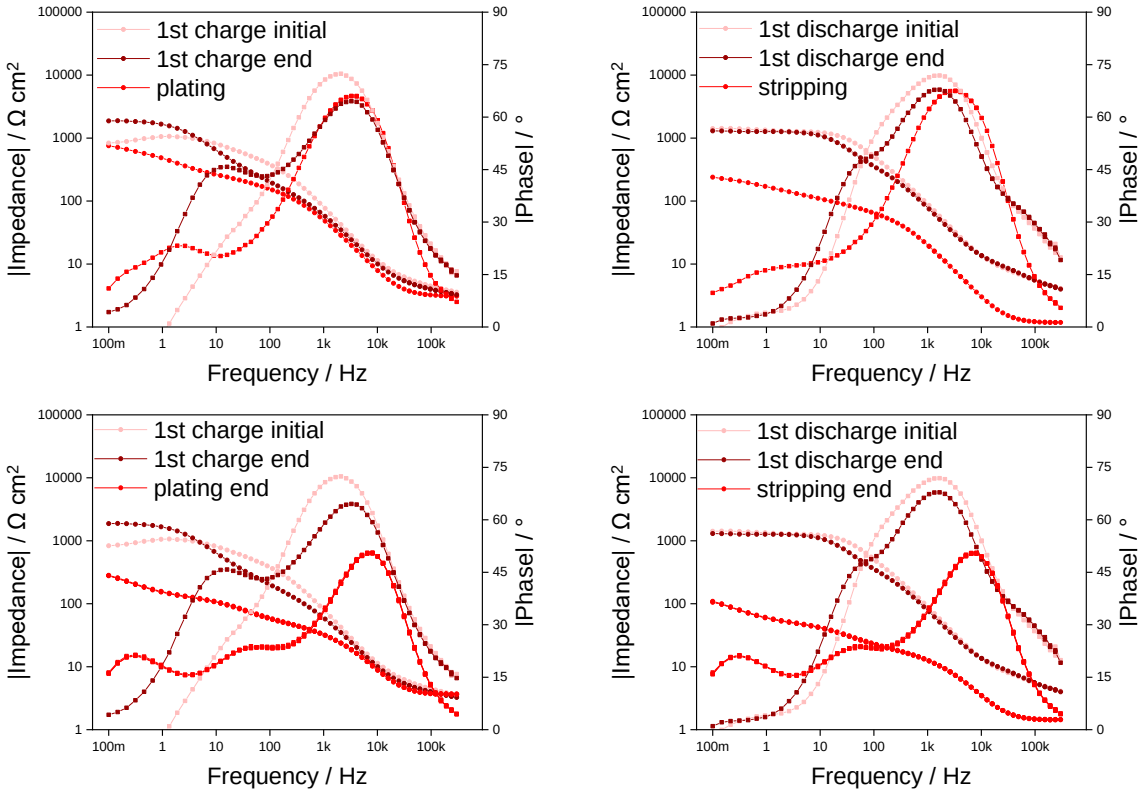

Figure A22: Comparison of the Bode plots of a symmetrical Mg-Mg cell and a Mg-S cell each with artificial Aquivion/PVDF SEI during stripping and plating at 0.1 mA · cm^{-2} (Mg-Mg) and during the first galvanostatic charge and discharge cycle at 0.1 mA · cm^{-2} (Mg-S).

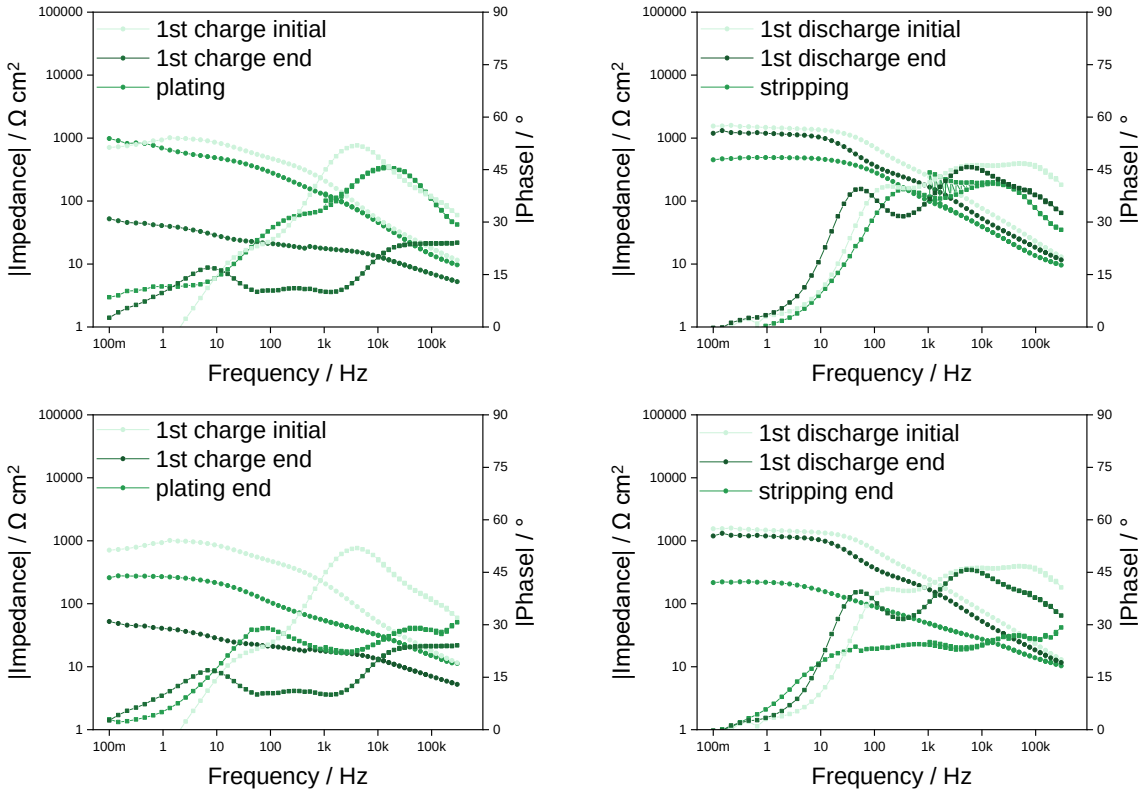

Figure A23: Comparison of the Bode plots of a symmetrical Mg-Mg cell and a Mg-S cell each with artificial SPEEK/PVDF SEI during stripping and plating at 0.1 mA · cm^{-2} (Mg-Mg) and during the first galvanostatic charge and discharge cycle at 0.1 mA · cm^{-2} (Mg-S).

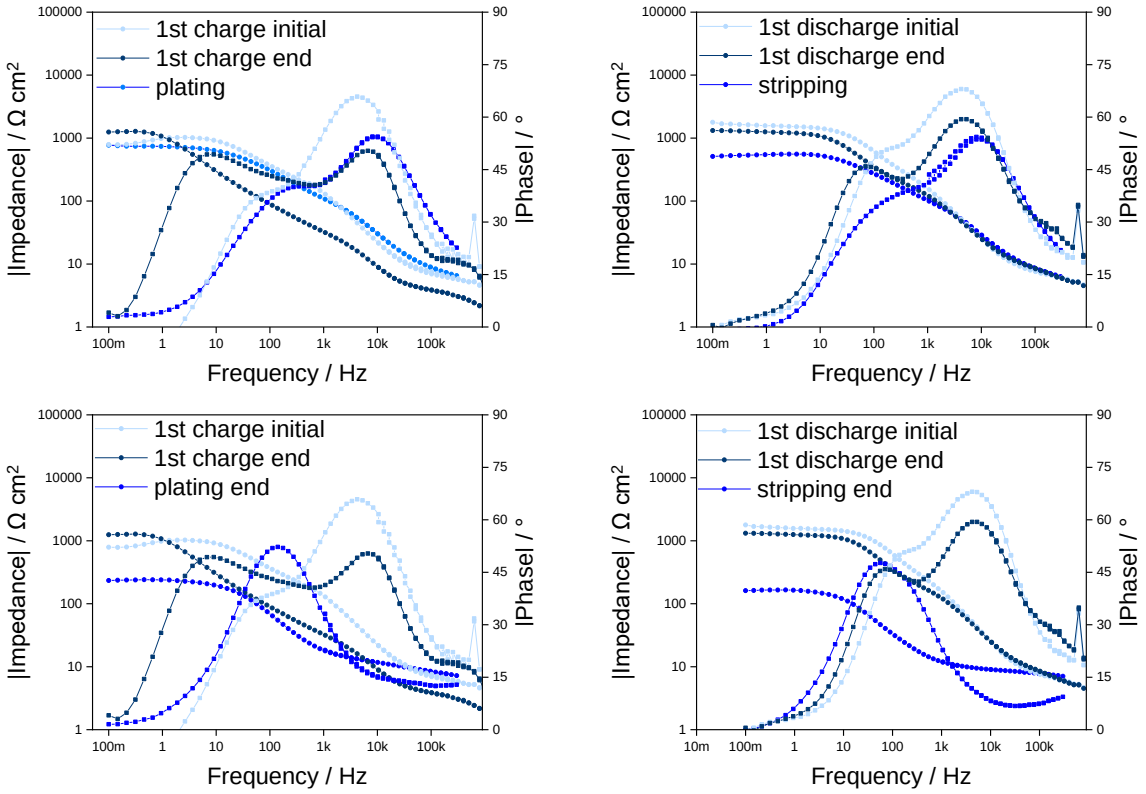

Figure A24: Comparison of the Bode plots of a symmetrical Mg-Mg cell and a Mg-S cell each with artificial PAN SEI during stripping and plating at 0.1 mA · cm^{-2} (Mg-Mg) and during the first galvanostatic charge and discharge cycle at 0.1 mA · cm^{-2} (Mg-S).